Study on Mechanical, Morphological & Machining Behavior of Reinforced Magnesium Metal Matrix Composite

Hanna Tadesse Kebede

A thesis Submitted to

The department of Mechanical Engineering

School of Mechanical, Chemical and Material Engineering

Presented in Partial Fulfillment of the Requirement for the Degree of Master's in Manufacturing Engineering

Office of Graduate Studies

Adama Science and Technology University

June, 2024

Adama, Ethiopia

Study on Mechanical, Morphological & Machining Behavior of Reinforced Magnesium Metal Matrix Composite

Hanna Tadesse Kebede

Advisor: Devendra Kumar Sinha (PhD)

A thesis Submitted to

The department of Mechanical Engineering

School of Mechanical, Chemical and Material Engineering

Presented in Partial Fulfillment of the Requirement for the Degree of Master's in Manufacturing Engineering

Office of Graduate Studies

Adama Science and Technology University

June, 2024

Adama, Ethiopia

DECLARATION

I hereby declare that this Master Thesis entitled **‘‘Study on Mechanical, Morphological & Machining Behavior of Reinforced Magnesium Metal Matrix Composite**” is my original work. That is, it has not been submitted for the award of any academic degree, diploma or certificate in any other university. All sources of materials that are used for this thesis have been duly acknowledged through citation.

___________________________	________________________	________________
Name of student	Signature	Date

RECOMMENDATION

I, the advisor of this thesis, hereby certify that I have read the revised version of the thesis entitled **‘‘Study on Mechanical, Morphological & Machining Behavior of Reinforced Magnesium Metal Matrix Composite”** prepared under my guidance by Hanna Tadesse Kebede submitted in partial fulfillment of the requirements for the degree of Mater’s of Science in Manufacturing Engineering. Therefore, I recommend the submission of the thesis to the department following the applicable procedures.

___________________________	________________________	________________
Advisor	Signature	Date

APPROVAL PAGE

I, the advisor of the thesis entitled **''Study on Mechanical, Morphological & Machining Behavior of Reinforced Magnesium Metal Matrix Composite**" and developed by Hanna Tadesse Kebede, hereby certify that the recommendation and suggestions made by the board of examiners are appropriately incorporated into the final version of the thesis.

Advisor	Signature	Date
______________________	______________________	______________

We, the undersigned, members of the Board of Examiners of the thesis by Hanna Tadesse Kebede have read and evaluated the thesis entitled ''**Study on Mechanical, Morphological & Machining Behavior of Reinforced Magnesium Metal Matrix Composite**" and examined the candidate during open defense. This is, therefore, to certify that the thesis is accepted for partial fulfillment of the requirement of the degree of Master of Science in Manufacturing Engineering.

______________________	______________________	______________
Chairperson	Signature	Date
______________________	______________________	______________
Internal Examiner	Signature	Date
______________________	______________________	______________
External Examiner	Signature	Date

Final approval and acceptance of the thesis is contingent upon submission of its final copy to the Office of Postgraduate Studies (OPGS) through the Department Graduate Council (DGC) and School Graduate Committee (SGC).

______________________	______________________	______________
Department Head	Signature	Date
______________________	______________________	______________
School Dean	Signature	Date
______________________	______________________	______________
Office of Postgraduate Studies, Dean	Signature	Date

ACKNOWLEDGEMENT

I give thanks to Almighty God for providing me the health and strength to do this work. Next, I would like to sincerely thank Dr. Devendra Kumar Sinha, my advisor, for all of his help, patience, and support during this thesis project. I also want to express my gratitude to my family for their unwavering support and prayers. For their help, I would like to thank Mr. Sintayehu Legesse (Head of the department), Mr. Samuel Kefyalew (PhD student), and Mr. Sintayehu (thermal stream). I would want to use this opportunity to express my gratitude to my teachers, friends, and other kind individuals for their time and insightful advice throughout my career.

TABLE OF CONTENTS

CONTENTS PAGE

LIST OF TABLES

TABLE PAGE

LIST OF FIGURES

FIGURES PAGE

ACRONYMS

ANOVA	Analysis of variance
ASTM	American Society for Testing Materials
CeO_2	Cerium Oxide
CNC	Computer Numerical Control
Gr	Graphene
Mg MMC	Magnesium Metal Matrix Composite
MMC	Metal Matrix Composite
SEM	Scanning Electron Microscope
SiC	Silicon Carbide
XRD	X-ray Diffraction

ABSTRACT

The goal of this thesis study was to create Mg- metal matrix composite materials with high-hardness, compression strength and corrosion-resistance for use in industrial and automotive applications. From optical microscope micrographs the grain distribution was analyzed and Scanning Electron Microscope showed particles distributed finely in base matrix. (AZ31B-5%CeO_2-10%SiC-4%Gr) shows minimum pores (0.2209), high relative densities (77.9%), uniform microstructure, higher Vickers hardness (111.2HV), compressive strength (339.6MPa) and minimum wear rate was investigated. The investigation of machining behavior was carried out through dry turning operation on Computerized Numerical Control (CNC) machine. The findings revealed that both tool wear rate and tool tip temperature were increased with increasing cutting speed and feed rate of AZ31B-5%CeO_2-10%SiC-4%Gr composite. The new reinforced Mg MMC material is thus expected to have potential uses in the automobile industry, as well as a variety of other structural applications.

Keywords***:*** AZ31B Mg MMCs, Casting, Turning, Surface roughness

CHAPTER ONE

INTRODUCTION

1.1 Background of the Study

The use of composite materials has constantly increased during the last decades. Several examples show that composite materials have entered in different industries as a viable alternative to traditional materials. Aerospace and defense industries have been pioneers in using composite material (Treviso et al., 2015). A composite material as the name itself elaborates it's a composition of materials. It is formation of two or more constituent materials having significantly different physical or chemical properties when combined together produces a material which possesses unique characteristics different from the constituent elements. Composite material is an amalgamation of a base material and a filler material. Base material is also called as matrix or a binder material as it surrounds and binds reinforcement of other material. Filler material or reinforcement is in the form of fragments, particles, and fibers, whiskers of natural or synthetic material (Rajak et al., 2019).

The matrix material of MMCs are compulsorily metallic (mostly aluminum (Al), magnesium (Mg), copper (Cu) & titanium (Ti)) and reinforcement could be either dispersed ceramics like oxides & carbides or it could be metallic (i.e. tungsten, molybdenum, lead). Reinforcement contributes a few percentages to around 50% of the total volume of the composite material (Rajak et al., 2019). Metal matrix composites are finding increasing application in many of today's industries. In particular, Magnesium and its alloys have gained widespread attention in scientific research as well as commercial application as energy conservation and performance demands are increasing because of their low density, approximately two-third of that of aluminum, and high specific strength as compared to other structural metals. These properties are important in automotive and aerospace applications in order to reduce fuel consumption and to reduce greenhouse emission. However, the application of magnesium alloys is limited evidently due to their poor creep resistance at high temperatures, low strength, low modulus and wear resistance. Therefore, Reinforcements are needed to improve the properties of the base metal. MMCs fabricated from magnesium would provide attractive alternatives to Al MMCs (Dey & Pandey, 2015).

The low density and improved damping resistance of magnesium-based alloys, among other special qualities, broaden their potential uses. Poor tribological behavior and limited corrosion resistance are two of these materials' drawbacks. Comparing AZ31 alloy to pure magnesium (Mg), one of the Mg-based alloys, the corrosion resistance is lower. Because of this, the alloy cannot be utilized to fabricate components for tribological purposes, such as cylinder liners and piston rings, or for use in maritime environments. Researchers' attention is drawn towards improving the properties of Mg-based materials as a result of this phenomenon. Numerous techniques, including surface treatment, protective coatings, and composite fabrication, can be used to increase a material's resistance to wear and corrosion. Among them, adding hard ceramic particles to a material to increase its mechanical and tribological qualities is best achieved through the process of composite manufacturing, which is the most well recognized and accepted approach. An improved metal matrix composite (MMC) with uniform distribution and size of reinforcements are thought to be the result of these two important elements. Nowadays, the field of material science is very interested in nanoparticle-reinforced composites due to their increased material characteristics. Another reason is that, in comparison to micro-sized reinforcements, a minor addition of nanoparticles shows more desirable features (Kavimani et al., 2017).

One of the crucial manufacturing procedures that is necessary to give a given raw material the proper shape is machining. During manufacturing, nanostructured materials also need to go through machining procedures. In this regard, it is essential to comprehend how grain size affects machining properties. In particular, there is not enough information in the literature about the machining of grain-refined magnesium alloys (Venkataiah et al., 2019).

The use of Magnesium alloy AZ31B nowadays has increased exponentially in the aeronautical industries for the manufacturing of certain high grade and complicated components. The reason for its perpetual usage is the fact that it has a very low mass to volume ratio and has very high hardness value, due to which it is used in aeronautical industries in order to improve the efficiency by decreasing the weight. AZ31B is reinforced with SiC and CeO_2 to improve its degradation rate and corrosive resistance. Also, it has proven to be a valuable alternative to Aluminum based alloys in industries due to its less density and high strength. That is why, in order to determine the best machining condition to manufacture these products, an analysis is carried out by dry turning operation by keeping some input parameters under control and obtaining the resulting output parameters which are going to be analyzed. Output responses which are going to be analyzed are

Surface roughness, cutting tool temperature, tool wear and MRR. These responses are analyzed in order to check the productivity and surface quality of the whole turning process at set and controlled input parameters which are spindle speed, feed rate and depth of cut.

1.2 Problem Statement

Now a day, Aerospace and automobile industries are highly in need of materials that are stronger, lighter and wear resistant. Therefore, composite material is replacing conventional materials and particular metal matrix composites due to their properties like high specific strength, high stiffness, better wear resistance and improved thermal resistance compared to base metals. Among metal matrix composites, magnesium alloy based composites have shown a significant improvement in mechanical and tribological properties in order to provide the demand of aerospace and automobile industries. But, the abiding problem is that, they are very difficult to machine due to the presence of hard abrasive ceramic reinforcing particles that build them stronger and stiffer than the base matrix and they lead to rapid tool wear and thereby short tool life and also cause poor surface finish of machined part. The performance measure of machinability includes surface finish. Therefore, the present work has been aimed to meet the challenges related to machining behavior of Mg MMC's.

1.3 Objectives

1.3.1 General Objective

The general objective is to develop, characterize, test and investigate mechanical, metallurgical and machining behavior of Mg based metal matrix composites.

1.3.2 Specific Objectives

The specific objectives of study are:

- To develop magnesium based metal matrix composite through casting route at different weight percentages of reinforcement particles.
- To investigate particle size distribution, microstructure, morphology, density, hardness, wear resistance, compressive strength and corrosion resistance of the developed material.
- To investigate MRR, tool wear rate and cutting tool tip temperature through numerical simulations at various cutting speeds, feed rate and depth of cut.

- To investigate the optimum values of cutting speed, feed rate and depth of cut using Design expert and GA.
- To conduct dry turning operation on a CNC lathe machine at optimum values of input machining parameters and to investigate surface roughness, cutting tool temperature, tool wear and MRR of the machined sample.

1.4 Significance of the Study

The proposed study work is to fabricate AZ31B/SiC/CeO_2/graphene hybrid composites and optimizing the process parameter of its machining characteristics to improve surface roughness, MRR, tool wear, and cutting tool temperature. Therefore, it has crucial benefits, both academically and practically, to individuals and to other stakeholders in aerospace and automobile manufacturing industries that are in need of this composite material. It improved the hardness, compressive strength, wear resistance and corrosion resistance of the base material which is AZ31B by adding the reinforcements. The best parametric combination of input process parameters were explored for the best possible machining characteristics. This work will be used as a reference for other students or researchers.

1.5 Scope of the Study

The research mainly concentrates on the development and investigation of mechanical and tribological properties of Magnesium reinforced metal matrix composite and optimization of its process parameters for machining characteristics to improve surface roughness, MRR, cutting tool tip temperature and tool wear rate. This research work includes: to develop AZ31B/SiC/CeO_2/Gr hybrid composites at varying weight composition of silcon carbide and cerium oxide, identification of reinforcement particle distribution and phase of materials, investigation of hardness, compressive strength and wear rate, experimental investigation of CNC dry turning, optimization of cutting process parameters for selected light weight, hard, strong and wear resistant material of AZ31B/SiC/CeO_2/Gr hybrid composites to improve surface roughness, MRR, cutting tool tip temperature and tool wear rate.

1.6 Thesis Organization

This thesis work contains five chapters. Chapter one includes; background of the study, problem statement, objectives of the study, research scope and significance of the study. The overviews of the literature on this area of study were provided under chapter two. In which fabrication method of MMC'S, the matrix and reinforcement utilized in metal matrix composites, the influence of reinforcement on microstructure, mechanical characteristics and machining properties of Mg MMC were all reviewed. Chapter three includes material selection, experimental procedure and testing and analysis method. Under chapter four several test findings and discussions on produced samples, simulation, optimization; actual machining and discussions on selected sample have been discussed and evaluated. Lastly chapter five presents conclusions, recommendation, reference and various appendixes.

CHAPTER TWO

LITERATURE REVIEW

2.1 Introduction

In this chapter related research works were reviewed on fabrication, testing and machining of magnesium based hybrid composites. The difficulties and solutions related to Mg MMC turning and its cutting parameters are also reviewed.

2.1.1 Composite materials

The term "composite material" clarifies that it is made up of several different materials. A material with unique attributes distinct from its basic elements is created when two or more constituent materials with significantly different physical or chemical properties are mixed. A composite material is created by combining a filler substance with a foundation material. Because it envelops and binds the reinforcing of other materials, base material is often referred to as a matrix or binder material. Reinforcement or filler material can take the shape of fibers, particles, or natural or synthetic material whiskers. In general, matrix is thought of as a relatively soft phase possessing particular mechanical and physical characteristics like as formability, ductility, and heat conductivity. The materials used for the matrix reinforcement have high strength, high stiffness, and minimal thermal expansion. Because the reinforcement phase of a composite bears the applied load on the material, it is typically stronger and stiffer than the matrix. (Rajak et al. (2019)

2.1.1.1 Classification of composite materials

A composite's size, form, content, temper state, kind of matrix, reinforcement, and other characteristics can all be used to classify it widely. (Kandpal et al., 2018) The principal composite classifications are Organic Matrix Composites (OMCs), Metal Matrix Composites (MMCs) and Ceramic Matrix Composites (CMCs). Polymer matrix composites (PMCs) and carbon matrix composites, often known as carbon-carbon composites, are the two kinds of composites that are typically included in the phrase "organic matrix composite." (Nagavally, 2017)

MMCs are developed by mixing the different materials to achieve uniform and controlled dispersion of the constituents. Compared to conventional materials, the mechanical qualities of composite materials are superior. PMCs are made up of several organic polymer types with continuous or short fibers and various reinforcing agents. (Sajan & Selvaraj, 2021)

Polymers yield high-quality components because they are easily processed. One key property of polymers is their lightweight nature. PMCs, or polymer matrix composites, have many different qualities. Among these are their exceptional mechanical qualities, low cost chemical inertness, remarkable chemical and corrosion resistance, high strength, excellent impact, compression, and fatigue properties, and cost-effective production and machining procedures. PMCs are typically used in rocketry, aircraft, and sporting goods. Metal Matrix Composites are materials that have advanced significantly. When it comes to improved mechanical and thermal qualities, such as outstanding thermal conductivity and strong wear resistance, MMCs outperform conventional materials. At the moment, aluminum, copper, iron, magnesium, nickel, and titanium are common matrix metals. Matrix of ceramics Composites are characterized as solid materials that typically exhibit extremely strong bonding, which is typically ionic but can occasionally be covalent. They are composed of a mixture of ceramic fibers, whiskers, and particles with a matrix of another ceramic. Glasses, metals, polymers, and ceramics can all be used to strengthen the ceramic matrix. The ceramic-based matrix materials exhibit outstanding compressive strength, high melting points, stability at elevated temperatures, and remarkable resistance to corrosion (Sharma et al., 2020).

MMCs are developed by mixing the different materials to achieve uniform and controlled dispersion of the constituents. Compared to traditional materials, composite materials have better mechanical qualities. Composite materials can have certain unique features.(Sajan & Selvaraj, 2021)

The sixth most common metal element in the world is magnesium. Magnesium has a lot of promise for use in structural and functional parts of the automotive, biomedical, and electronics sectors because of its rich content, low density, extremely high specific stiffness, superior vibration damping, recyclability, and benefits in machining.

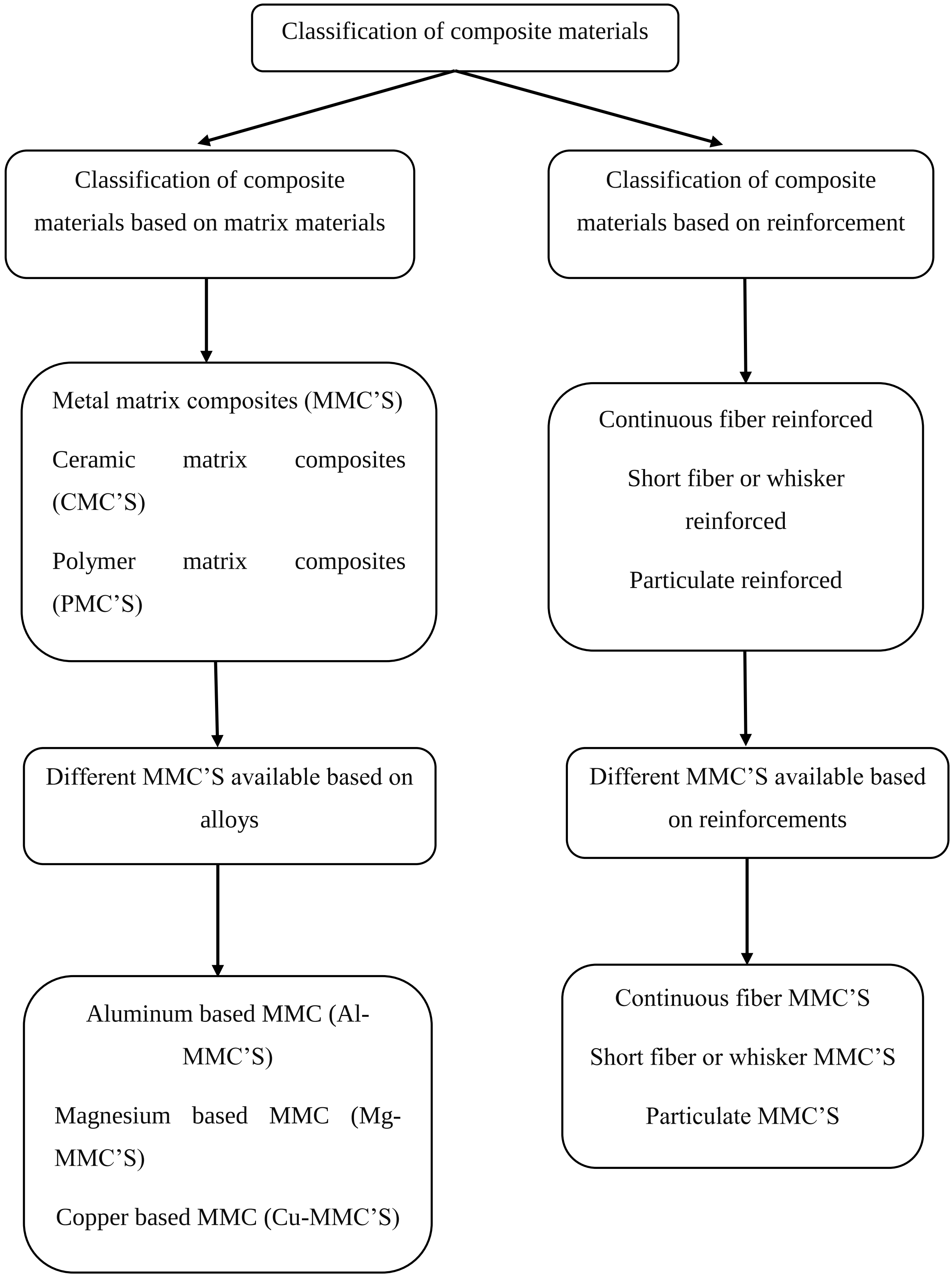

Figure 2.1 Flow chart showing the broad classification of composite materials.(Lakshmikanthan et al., 2022)

Table 2.1Metallic matrix and their drawbacks (Dhanesh, Kumar, Fayiz, et al., 2021)

Matrix Materials	Density (g/cm^3)	Major drawbacks to be filled by reinforcements
Al	2.70	⇒ Its possible use in high temperatures is limited by its temperature range. ⇒ Low strength and hardness
Mg	1.74	⇒ Quick rate of creep, low resistance to wear and corrosion, and chemical reactivity
Cu	8.92	⇒ Low hardness, low creep resistance, low tensile and compressive strength
Fe	7.87	⇒ Low hardness, low tensile yield strength, and inadequate resistance to wear and corrosion

2.2 Reinforcement types

Islam et al. (2021) **f**ocused on the effects of reinforcing on composites made of stir-cast magnesium. The demand for materials with high specific strength and low weight led to the development of composite materials with a magnesium foundation. Due to their remarkable qualities and reasonable price, magnesium metal matrix composites, or MMCs, have found a wide range of applications in various industrial fields. This work provides a brief assessment of the impacts of reinforcing several materials in magnesium-based alloys formed by standard and modified stir casting, such as carbon nanotubes, graphite, titanium carbide, and alumina. It also demonstrates how the perfect selection of stir casting process parameters improves the wettability and quality of the produced composite.

2.3 Ceramic Particulate Reinforced Mg MMCs and Hybrid Mg MMCs

Table 2.2 Magnesium-based composites made by stir casting: An overview of the effects of reinforcing

Material used	Reinforcement	Aim	Research finding
Mg-5Al-2Ca	SiCp (Volume fraction of 2%, 5%, 10%)	Effect of reinforcement on the composite's	The strengthening of SiCp disrupts the Al2Ca network distribution at grain

		mechanical characteristics and microstructure	boundaries. Enhancement in work hardening rate and tensile yield strength. Maximum ultimate tensile strength at 5% SiCp volume percentage. During the tensile process, interfacial debonding between the matrix and reinforcement could result in fracture.
AZ31	WC nanoparticles(wt.% of 0.5, 1, 1.5 and 2)	Impact of weight % of WC nanoparticles and surface roughness on AZ31 corrosion behavior	AZ31-2WC exhibits modest agglomeration effects, however nanoparticles improved the grain structure overall. The micro hardness increases with the weight percentage of WC. As it turns out, the composite with WC of weight percentage 0.5 WC is the most corrosion resistant, followed by composites with WC of 2%, 1.5%, and 1%, in that order. When the corrosion behavior of Mg-2wt.%WC with varying surface quality is tested, it is discovered that the sample with the least amount of surface roughness exhibits greater corrosion resistance.
AZ31	Fly Ash (10 vol%)	Effects of stir casting versus FSP	Through stir casting processing, it was discovered

		on the wear resistance and microstructure of the Fly Ash composite reinforced with AZ31	that there was coarse grain structure and particle dispersion inhomogeneity. The molten magnesium matrix and the fly ash particle were found to have good wettability. The reaction between the molten material and the reinforcement is initiated by the high casting temperature.
AZ91	Titanium dioxide (TiO_2) (composition of 1%, 2%) and Graphene (0.5%)	Analyze the mechanical behavior and wear of the TiO2/Graphene hybrid composite reinforced with AZ91.	The reinforcement is distributed uniformly and exhibits a fine grain structure in hybrid composite. density, ultimate tensile strength, and enhanced hardness Slipping Wear loss decreases and wear resistance significantly improves as the fraction of reinforcement rises.
AZ31	$CaSiO_3$ (weight percentage of 0,2, 4,6,8)	CaSiO3's effect on the characteristics of AZ31	The inclusion of reinforcement increased the micro hardness. The maximum hardness was determined with a 2% reinforcing addition.
AZ31	Multiwall Carbon nanotubes (CNTs)- (weight% of 0, 0.1, 0.5, and 1)	Impact of varying Multiwall CNT fractions on the AZ31-based	As the weight concentration of CNTs increases, so do hardness and density. Significant reduction in

		composite's microstructure, tribological characteristics, and wear processes.	porosity and wear rate as CNT concentration rises. For both dry and wet sliding, the coefficient of friction initially decreases and then almost always increases in a consistent manner.
AZ91D	Ti2AlC (vol. % of 5,10,15,20)	Examining the microstructure and mechanical characteristics of reinforced Ti2AlC AZ91D mg composite	Hardness, compressive strength, yield strength, and density all rose with a rise in the volume percentage of reinforcement, although Mg grain size and percentage elongation decreased. It was discovered that the 10% volume of reinforcement produced the maximum ultimate tensile strength. In composites with reinforcement percentages of 15% and 20%, agglomeration of reinforcement was observed. The reinforcement limits the expansion of the magnesium particle. The kink band behavior of reinforcement, which guarantees strong damping properties, was demonstrated by a compression test.
AZ91D	B4C (compositions by wt. % of 0, 1.5, 1.5), Graphite	identifying the characteristics of the hybrid composite	With an increase in reinforcing, density rises and porosity falls. Furthermore,

	(composition by wt. % of 0, 0, 1.5)	made from an alloy based on magnesium and reinforced with graphite and boron carbide	tensile and hardness strengths rise, but the composite that just has B4C as reinforcement exhibits the highest tensile and hardness strengths. Compared to the base alloy and hybrid mg composite, AZ91D–B4C has a greater coefficient of friction and superior wear resistance. Graphite reinforcing reduces adhesion wear because it has strong lubricating properties..
AZ91E	SiC, Fly Ash (both having wt. % of 0, 2.5, 5)	To investigate the mechanical characteristics and microstructure of the hybrid AZ91E composite	Tensile strength, hardness, and density all rise slightly as reinforcement levels rise. The homogeneous distribution of reinforcement in the matrix material results in an increase in hardness. Grain refining results in a decrease in fracture toughness when compared to the basic alloy.
ZX51	Al2O3 (vol. % of 2.25, 4.50, and 6.75)	Effect of Al2O3 reinforcement on the microstructure and mechanical properties of ZX51 alloy	Reinforcement enhances porosity but also causes grain refining. The addition of reinforcement causes brittle behavior in the composite, indicating a decrease in toughness. Strengthening of yield and hardness increases.
AZ91C	TiC (particle size:	Examine how the	For stir-cast composites,

	5–20 µm) 12 wt%	wear behavior and microstructure of the AZ91C–12 weight percent TiCp composite relate to one another in dry sliding contact.	delamination wear determines the wear rate; for heat-treated composites, tribo oxidation in addition to delamination wear determines the wear rate. The as-cast composite has a wear rate that is twice as low as the heat-treated composite. In comparison to the heat-treated composite, the as-cast composite has a coefficient of friction that is 4.5 times higher.
AZ31B	$Mg_2B_2O_5$ whiskers (vol. % of 1.0, 3.5 and 6.0)	Examining how various volume ratios, whisker textures, and Mg2B2O5 microstructure affect the mechanical characteristics of composites based on AZ31B.	Mg2B2O5 addition allows for grain refining of a matrix. The dispersion appears agglomerated as the volume of whisker reinforcement rises, though. MgO forms an interfacial interaction between the reinforcement and matrix. By adding 1 vol% of reinforcement, it was possible to increase the yield strength, UTS, and elongation; however, adding an additional 3.5 or 6 vol% of reinforcement had detrimental effects on the composite's mechanical properties.

Suneesh and Sivapragash (2018) centered on hybrid composites made of magnesium, where the base matrix is additionally reinforced with many phases. With regard to processing techniques and the choice of reinforcing phases, hybrid composites provide a great deal of flexibility. These composites could therefore find use in the automobile and aerospace industries.

2.4 Solid-Lubricant Particulates Reinforced Mg MMCs and Hybrid Mg MMCs

Khatkar et al. (2018) investigated about self-lubricating HMMC's strengthened with graphite as secondary reinforcement. The mechanical and tribological behavior of self-lubricating HMMCs based on magnesium and aluminum was the main focus of the investigation.

2.5 The mechanical and tribological characteristics of metal matrix composites based on magnesium

A material's behavior under mechanical loads is determined by its mechanical characteristics. Different strength tests, such as tensile strength, compression test, three-point flexural strength, hardness test, impact strength, etc., are used to determine the mechanical properties. The gradual loss or removal of material from the surface is defined by tribological parameters like wear rate.

Veeranjaneyulu et al. (2023) investigated mechanical characteristics and microstructural distribution of manufactured hybrid nano composites. The outcomes demonstrate that the mechanical characteristics and uniform distribution of SiC and Gr particles are enhanced compared to those of the base alloy. In comparison to monolithic AZ31 alloy, micro hardness, ultimate tensile strength (UTS), yield strength (YS), and compressive strength (CS) were raised by about 54%, 68%, 82%, and 107%, respectively. Te presence of reinforced particles, the uniform distribution of particles, and the strong interfacial connection between the matrix and reinforcement all contribute to the improvement of mechanical properties. However, the addition of 7 wt. % SiC/Gr showed good mechanical properties compared to the base alloy. Te microstructure of Nano composites was analyzed using a scanning electron microscope (SEM), and particles were described using energy-dispersive spectroscopy (EDS).

Shen et al. (2018) TEM microstructures of composites were examined in order to determine the impact of SiCp/m+s+n on the dynamic recrystallization (DRX) behavior of the magnesium matrix. The findings showed that increasing the ratio of DRXed nucleation and lowering the average particle size of the matrix were two benefits of adding

SiCp/m+s+n. The tensile test results show a notable increase in the AZ31B/SiCp/m+s+n composites' strength.

Manroo et al. (2022a) observed that incorporation of Al_2O_3, CeO_2, and MWCNTs nano reinforcement particles into the Mg-ZE41 alloy by FSP produced MMCs without any defects, the distribution of the nanoparticles into the MMCs was fairly homogenous, except for ZE41-MWCNTs MMC, and a clean interface was observed between the reinforcement particles and the Mg-ZE41 matrix, The grain size was seen to be reduced from 113 lm (cast-ZE41) to 4lm by FSP, and further to 1.41lm by the addition of CeO_2 particles and In comparison to the base alloy, all of the produced composites shown strong wear resistance. Of these, the ZE41-CeO_2 composite displayed the greatest wear performance because to the CeO_2 particles' solid lubricating action.

Al-maamari et al. (2020) SEM, EDX, and XRD were used to study the morphological examination of the component powders and the hybrid powder mixture. The microstructure of the sintered MMCs revealed that the reinforcement was dispersed evenly throughout the matrix. Comparing the produced hybrid MMCs to the base material and the Mg-Gr composite, the former showed better mechanical properties. With dry sliding conditions, the pin-on-disc tribometer was used to examine the tribological characteristics of the produced hybrid MMCs. Compared to the matrix Mg, the hybrid MMC made of 5% Gr and 10%SiC (Mgá5%Grá10%SiC) exhibits a 92% lower wear rate and a 53% lower friction coefficient. As a result, this hybrid MMC may be a good option for developing tribological operation-related components.

Zhang et al. (2018) investigated the friction coefficient of Mg Nano composite reinforced with 15 vol% SiC nanoparticles is much higher than pure Mg and AZ31B alloy. Its wear resistance is about 23 times higher than that of pure Mg. Analysis on the surface and debris suggests that the delamination mechanism of Mg has been overcome by the addition of high volume fraction nanoparticles, and the dominant wear mechanism of the Mg-SiC Nano composites is oxidation.

Banerjee et al. (2021) examined how graphite nanoparticles affected the corrosion properties and Nano indentation behavior of Mg–WC Nano composites. Stir casting combined with ultrasonic treatment is how composites are created. Scanning electron microscopy and optical microscopy are commonly used to characterize Nano composites. Energy dispersive X-ray analysis is used to analyze the compositions of as cast materials.

Tests using Nano indentation are used to reveal the hybrid Nano composites' elastic modulus and Nano hardness. The inclusion of 1 weight percent Nano Gr as reinforcement to Mg–WC composites has improved their Nano hardness and elastic modulus; however, additional additions had negative consequences. Potential dynamic polarization tests and electrochemical impedance spectroscopy are used in corrosion testing. According to a corrosion study, adding 1 weight percent of graphite powder has increased corrosion resistance; however, adding more graphite nanoparticles causes the corrosion resistance to drop. In order to determine the mechanism of corrosion, corroded surfaces are evaluated. This reveals that, out of all hybrid Nano composites, the surface of Mg–2WC–1Gr nano composite has the fewest number of cracks collinear with its lowest corrosion rate.

Manroo et al. (2022b) studied the surface modification and fabrication of surface composites of magnesium alloys by friction stir processing**.** The mechanical and tribological properties such as tensile strength, hardness, corrosion resistance and wear resistance of magnesium alloys can be improved by making a surface composite layer of reinforcement particles on magnesium alloys by FSP.

Saranu et al. (2020) did a review on magnesium metal matrix composites. The study includes, reinforcing substantial, processing techniques, Characterization, tribological and mechanical behavior of Mg-MMCs. Furthermore, the CNT, Carbonaceous, Fullerene, SiC, Al_2O_3, TiC, B4C, Graphene reinforced Mg-MMC articulates. The mechanical behavior of hardness, compressive strength, tensile strength, and tribological characteristics of wear rate and corrosion performance was therefore examined for a variety of cutting-edge techniques. Considering the observation, The Al and SiC reinforced Mg alloy based MMT provides finest relationship to the fiber matrix contrast to CNTs. Thus the reinforced MMCs attained more influence stress, more tensile strength, less thermal growth and more hardness. Besides, the CNTs reinforced MMCs attained high strength and low mass density due to the friction coefficient reduction. While compare to the Al_2O_3 and SiC, the CNT fabrication provides light weigh MMCs. The corrosion resistances properties are reduced using SiC, yet the properties are enhanced by other reinforced particles.

Banerjee et al. (2023) examined how adding graphite (Gr) and WC nanoparticles affected the tribological properties of magnesium-based hybrid Nano composites at various WC and Gr weight percentages. Using the stir casting method in conjunction with ultrasonic vibration, hybrid Nano-composites were created. Energy dispersive spectroscopy (EDS), optical microscopy (OM), and scanning electron microscopy (SEM) were used to investigate the synthesized Nano-composites in detail. Particle inclusion and improved microstructural integrity as compared to the base alloy Mg AZ31 are both confirmed by characterization. As-cast hybrid Nano composites' micro hardness values were also noted. The micro hardness of Mg-1WC and Mg-2WC Nano-composites is increased by the addition of 1 weight percent of Gr nanoparticles. The tribological experiments were performed utilizing a pin-on-disk tribo tester with different weights (10 N–40 N) and sliding speeds (0.1 m s−1–0.4 m s−1). Results for Mg-WC Nano composites containing 1 weight percent of Nano-Gr are superior to those containing 2 weight percent of Nano-Gr. The materials with the lowest coefficient of friction (COF) are Mg-2WC-1Gr, Mg-1WC-1Gr, Mg-1WC-2Gr, and Mg-2WC-2Gr. We also looked at the roughness values of worn surfaces. The Mg-2WC-1Gr sample's worn surface has the least amount of roughness. SEM analysis of worn surfaces was also performed to identify wear mechanisms. The most common abrasion in hybrid Nano composites containing 1 weight percent of Gr is accompanied by the most common delamination in those containing 2 weight percent of Gr.

Jayalakshmi et al. investigated the hardest measurement (165 BHN), which is almost twice as high as the unreinforced base alloy's (85 BHN), was obtained from the largest volume fraction (25%) that was examined. Four test temperatures—25°C (room temperature), 100°C, 150°C, and 200°C—were used for the tensile testing. Percentage elongation initially rises as well.

Lim et al. claimed that Mg-Al/SiCp exhibits better density, macro-hardness, and elastic modulus than Mg-Al. Wear rates are higher under the higher load of 30 N, according to the volumetric wear rates for the Mg–9Al alloy and its SiCp–reinforced composite. The addition of SiCp reinforcement improves the Mg-Al alloy's wear resistance by a small but steady 15–30% for lower loads of 10 N, with the exception of the fastest speed of 5 m/s, where wear rates are almost comparable.

Jiang et al. found that B_4C/Mg composites containing 20 vol. % B_4C particles have a harder surface than as-cast magnesium ingots. As predicted, the volumetric wear rate of the B_4C/Mg composite is clearly lower than that of the as-cast magnesium ingot.

Poddar et al**.** investigated the mechanical properties of SiC (15 vol.%) reinforced cast magnesium matrix composites (AZ91D) and found that the composite with 150 μm size particles had a significantly lower increase in hardness and elastic modulus when compared to Mg15 vol.% of SiC monolithic composite. Composite materials' ultimate tensile strength and ductility were lower than those of unreinforced alloys.

2.6 Fabrication methods of Mg metal matrix composite

A multitude of solid and liquid phase manufacturing pathways are accessible for the production of metal matrix composites based on magnesium, featuring diverse forms of reinforcement, sizes, volume fractions, and other characteristics. In contrast to liquid phase processes, which combine liquid metal matrix and solid reinforcement, solid phase processes include joining matrix and reinforcement without melting them, similar to powder metallurgy techniques.

Dash et al. (2018) Magnesium and its alloys are primarily processed using either solid phase (powder metallurgy) or liquid (sand casting). The liquid phase processing is more advantageous than the solid phase processing because the solid phase has higher processing costs, limits thickness, lower ductility, and fracture toughness, and requires laborious handling of fine powders. Examples of liquid phase processes include semisolid metal (SSM) casting, stir casing, melt infiltration method, in-situ synthesis, and die casting under high pressure and gravity.

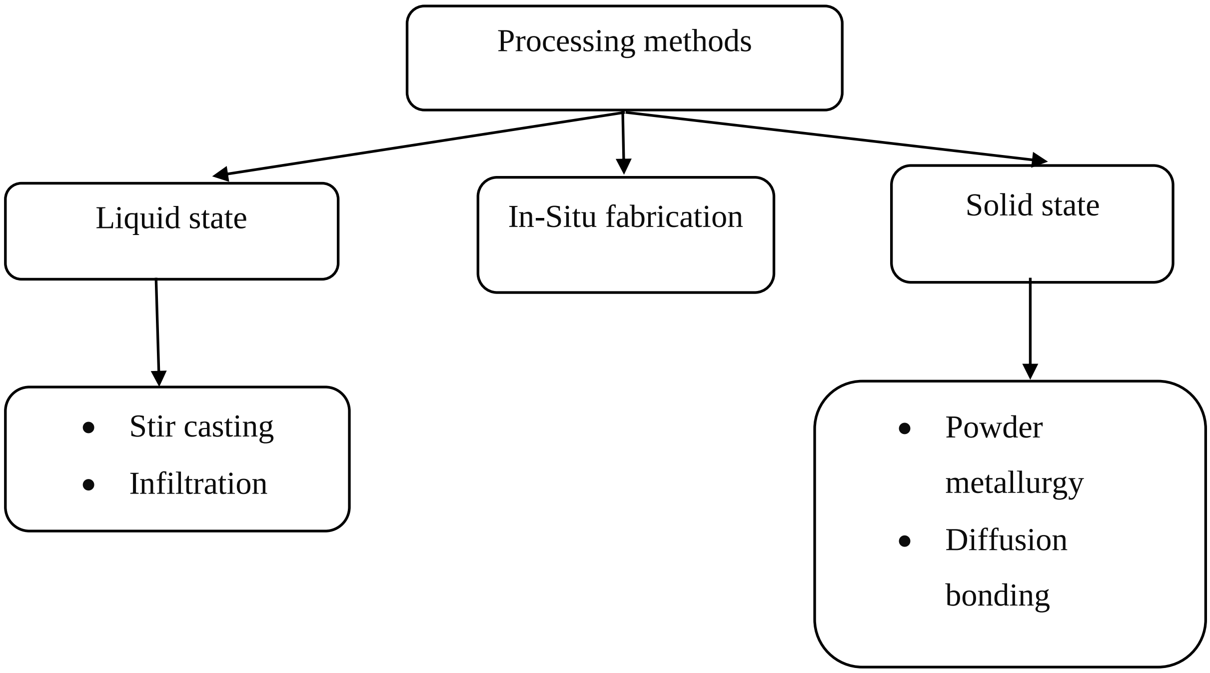

Figure 2.2 Classification of metal matrix composite preparation methods. (A. Kumar et al., 2021)

Anand (2020) reviewed the evolution and impact of tribomechanical characteristics on hybrid metal matrix composites based on magnesium. The methods of development, like stir casting and powder metallurgy, were most commonly used in a majority of works.

A better liquid processing approach is stir casting. Because of its ease of use, adaptability, and low processing costs, Stir casting is among the least expensive ways to make metal matrix composites. Both magnesium alloy and magnesium alloy composites can be cast using the stir casting technique.(Kumar et al., 2018)

Xiao et al. (2021) investigated on developing stir casting-produced composites AZ31B-GNPs. By using the "Sandwich" stacking technique, composites made of AZ31B magnesium alloy containing GNPs at weight percentages of 0.1, 0.3, 0.5, and 0.7. According to experimental findings, GNPs are a great reinforcing phase for alloys and magnesium.

Veeranjaneyulu et al. (2023) studied the mechanical characteristics and microstructure of hybrid Nano composite AZ31-SiC-Graphite that were created using stir casting machines with bottom pouring technology. Silicon carbide (SiC) and graphite (Gr) weight percentages of 0, 3, 5, and 7 were employed in the creation of AZ31 magnesium alloy hybrid Nano composites using a bottom pouring-style stir casting process.

Manroo et al. (2022b) researched the use of friction stir processing to modify the surface and create surface composites of magnesium alloys. Improvements were noted in two areas, the Mg/rare earth system and the Mg-AZ system, with regard to the realization of surface-modified magnesium alloys.

Singh and Belokar (2021) focused on every important aspect of the tribological behavior of hybrid metal matrix composites; stir casting was determined to be the best fabrication method after a thorough evaluation of the body of literature; for wear analysis on Al and Mg-based hybrid metal matrix composites, a pin on disc tribometer is strongly advised.

Shen et al. (2018) investigated The characteristics and mechanical properties of magnesium matrix composites enhanced with SiC particles of nano, submicron, and micron sizes are presented. Stirring casting method was used to create the AZ31B/SiCp/m+s+n composites, which are magnesium matrix composites reinforced by (submicron[s] + nano[n] + micron[m]) SiC particles (SiCp).

2.7 Machinability of magnesium based metal matrix composites

Machining is a process in which a material (often metal) is cut to a desired final shape and size by a controlled material-removal process. Computer Numerical Control (CNC) machining is a manufacturing process in which pre-programmed computer software dictates the movement of factory tools and machinery. The process can be used to control a range of complex machinery, from grinders and lathes to mills and CNC router.

Gao et al. (2020) utilized a combination of regression analysis and experimentation to examine the areal surface roughness of AZ31B Mg alloys. As the feed rate decreases, the machined end face's areal surface roughness, Sa and Sz, also drop. 0.05 mm/rev feed rate, 0.3 mm cut depth, and 85 m/min cutting speed are all used here. The lowest values of Sa and Sz are 5.480 μm and 0.577 μm, respectively. The factors that contribute the most, second most, and least to Sa are the feed rate, depth of cut, and cutting speed, in that order. Since the depth of cut, feed rate, and cutting speed can account for 97.5% of the variation in Sa, the linear regression model can predict Sa of AZ31B machined with dry face turning.

Sun et al. (2019) done the experimental investigation on micro-drilling properties of Mg-based MMCs reinforced with HAP nanoparticles. In this research, Hydroxyapatite (Ca10(PO4)6(OH)2, HAP) nanoparticle-reinforced magnesium-based metal matrix composites (MMCs) have been investigated as bone substitute materials due to their superior biocompatibility and biological activity. Additionally, it was noted that Mg/HAP MMCs were chosen and their micro-drilling characteristics were disclosed with varying HAP levels (0.5, 1.0 wt%). The MMC chip was examined first. Second, under various cutting conditions, the surface roughness of Mg/HAP MMCs was examined. The findings demonstrated that, in contrast to pure magnesium, surface roughness diminishes as feed rate increases and as spindle speed increases. Additionally, all burr shapes fall into the uniform burr category, and burr height rose as spindle speed and feed increased. Finally, a study was conducted on the size effect of micro-drilling. For Mg/HAP MMCs, 1.0 μm was found to be the minimal cutting thickness per tooth.

Davis et al. (2017) investigated Chip Morphology and Chip Formation Mechanism during Machining of Magnesium-based Metal Matrix Composites. Magnesium-based MMC machinability is currently mainly unattainable. Broad ranges of cutting speeds are used during the machining of magnesium-based MMCs to clarify the chip shape and creation mechanism. It is discovered that cutting speed has the greatest impact on the morphology of chips as well as the mechanism of chip production; as cutting speed rises, so does the likelihood of discontinuous, particle-type chip development. At low cutting rates (less than 0.5 m/s), saw tooth chips are primarily observed, but discontinuous, particle-type chips are more common at high cutting speeds (more than 1.0 m/s). It is discovered that the genesis of the saw-tooth chip shape is caused by fracture initiation at the free. Nevertheless, it is discovered that fracture initiation at the tool tip is what causes the discontinuous, particle-type chip morphology to form as cutting speed (and strain rate) rise. Furthermore, an investigation into the effects of tool rake angle, particle size, and particle volume fracture reveals that these factors have minimal bearing on the morphology and production mechanism of chips.

Hira et al. (2021) investigated influence of machining settings on average surface roughness Ra during turning hybrid Mg MMC-An experimental technique. Due to its high molecular strength, low density of these combined materials, and lightweight nature, hybrid metal matrix composites (MMC) reinforced with silicon carbide (SiCp), alumina (Al_2O_3p), and graphite (Grp) are becoming more and more popular for industrial applications. For application goods, the manufacturing industries that use hybrid Mg-MMC also go through machining and turning processes. For the hybrid Mg-MMC to have the appropriate dimensional accuracy, machining is therefore crucial. Thus, the goal of the current experimental study was to determine the average surface roughness height Ra during the hybrid Mg-MMC's rotation utilizing the tungsten carbide insert CCMT 09 T3 08 WF 1525. The cutting speeds of 40, 80, and 120 m/min, the feed rates of 0.08, 0.2, and 0.4 mm/rev, and the depth of cut of 0.2, 0.5, and 0.75 mm were among the machining parameters. Using a surfcom 130A (profilometer), the average surface roughness height Ra was calculated. The results of an experimental examination showed that at lower feed rates and high cutting speeds, the average surface roughness height Ra was lower. Moreover, for all cutting speed settings, the built-up edges were created at a reduced feed rate.

Raj et al. (2020) investigated mechanical characteristics and machining of Mg AZ91D/SiC/Al_2O_3 MMC. Since the reinforcement percentages increase in magnesium composites of Mg AZ91D/SiC/Al_2O_3, the surface roughness decreases. The sole variable influencing the output reactions is the depth of cut. (surface roughness and material removal rate) in a CNC lathe, as opposed to other input process parameters.

P. S. Kumar et al. (2021) examined HfC reinforced ZE41 magnesium matrix composites for machining and corrosion investigations. The density of dislocations created at the interface between the matrix material and reinforcements during machining is crucial in lowering cutting forces. The dislocation densities between the magnesium matrix and the HfC reinforcement caused a thermal mismatch that resulted in a reduction of the cutting forces. Cutting force mechanism was produced during machining by the solid lubrication provided by HfC reinforcements. Using SiC & RHA in metal matrix composites resulted in a similar decrease in cutting forces.

2.8 Research gap

It has been observed from the literature review that some researches have been carried out on synthesis, characterization and testing of Magnesium metal matrix composites applicable to various applications. Almost all research paper have developed a composite material having a gaps between reinforcement and final solidified matrix due to poor wettability which reduces ultimate strength, composite material having high particle segregation at bottom and float over the surface of liquid metal which results high porosity, heterogeneous mechanical and tribological properties and leads difficult to machine. Fabrication process parameters affect the machining characteristics and very few works has been carried out including the machining characteristics of casted Magnesium metal matrix composites. Moreover, the machining characteristics of casted AZ31B Magnesium metal matrix composites on optimum machining conditions have not been studied. Thus, the proposed work aims to improve the mechanical and tribological properties of reinforced magnesium metal matrix composites; fill the research gap by optimizing the process parameters (cutting speed, feed rate, and depth of cut); and improve its machining characteristics (surface roughness, tool wear, and cutting tool temperature).

CHAPTER THREE

MATERIALS AND METHODOLOGY

3.1 Materials

Materials that are to be used on this research work are metal matrix (magnesium alloy) and reinforcement phases (SiC, CeO_2) that yields the needed properties and small amount of graphene will be used for self-lubrication properties. This selection has to be considered regarding to cost, properties and availability.

3.1.1 Magnesium Alloy AZ31B Matrix Selection

The alloy magnesium AZ31B is widely utilized in many different industries because of its special qualities, strength, and low weight. It is a blend of zinc, aluminum, and magnesium. This alloy's excellent resistance to corrosion and ease of machining has made it a favorite in the automotive, aerospace, and biomedical industries.

Table 3.1 Chemical Composition of Magnesium Alloy AZ31(Kavimani et al., 2017)

Elements	Al	Zn	Mn	Fe	Cu	Si	Ni	Mg
Wt %	3.5	1.4	0.3	0.003	0.008	1.2	0.001	Balanced

3.1.2 Reinforcements

3.1.2.1 Silicon Carbide

Silicon carbide (SiC) is the third hardest material after diamond and boron nitride, which gives SiC its excellent properties such as high-temperature stability. Silicon carbide used as reinforcement in the form of particulates, fibers to develop the properties of the composite. When surrounded in metal matrix composites SiC certainly improves the overall strength of the composite along with corrosion and wear resistance.

Figure 3.1 Silicon Carbide

Table 3.2 Mechanical Properties of SiC (Olani et al., 2023)

Properties	SiC
Elastic modulus(GPa)	410
Density (g/cc)	3.1
Poisson’s ratio	0.14
Hardness (HB500)	2800
Compressive strength (C) (MPa)	3900(C)

3.1.2.2 Cerium oxide (CeO_2)

CeO_2 is an attractive rare earth oxide with positive electrochemical stability, thermal stability, high hardness, and excellent wear resistance (Liu et al., 2023). In this magnesium metal composite it improves micro hardness, wear resistance and compressive strength which make it suitable for many applications.

Figure 3.2 Cerium oxide

3.1.2.3 Graphene (Gr)

Graphene is a material that is extracted from graphite and is made up of pure carbon, one of the most important elements in nature and which we find in daily objects like the lead of a pencil. Graphene stands out for being tough, flexible, light, and with a high resistance.

Because of its special qualities in thermal conductivity, lubrication, and mechanical performance, graphene is mostly employed. Graphene has an elastic modulus of 1100 GPa and a tensile strength of 125 GPa. Research indicates that the strength and ductility of pure magnesium can be enhanced by adding more expensive types of reinforcement. Typically, reinforcements employed in composites take the form of powder. In addition, graphene presents a promising option for the reinforcement of metal matrix composites, with superior mechanical capabilities and perfect conductivity. Magnesium's mechanical qualities and biocompatibility are improved by graphene, which is utilized as a reinforcing material at various weight percentages (Raja et al., 2021).

Figure 3.3 Graphene

3.1.3 Selection of Cutting Tool

Any tool that uses shear deformation to remove metal from a work piece is considered a cutting tool. To perform an effective cutting operation, the cutter should be made from a material three times harder than the work material to be cut. The tool must be ready to withstand the heat generated during the machining process. The tool must have a specific geometry (known as tool geometry) for effective cutting and smooth surface finish. The aluminum oxide coated carbide insert tools will be used in this study's single-point cutting tool selection process. Due to their resilience against crater and flank wear, low thermal conductivity, and high temperature tolerance.

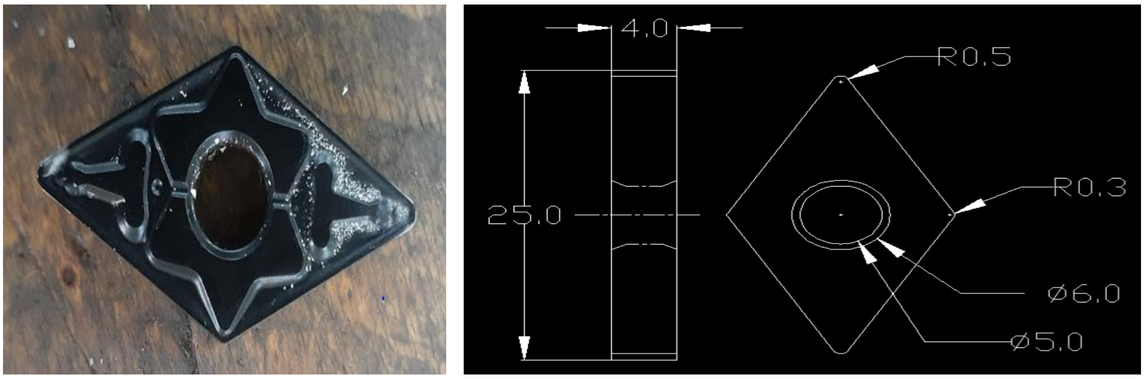

Figure 3.4 Aluminum oxide coated carbide insert and its geometry

3.2 METHODOLOGY

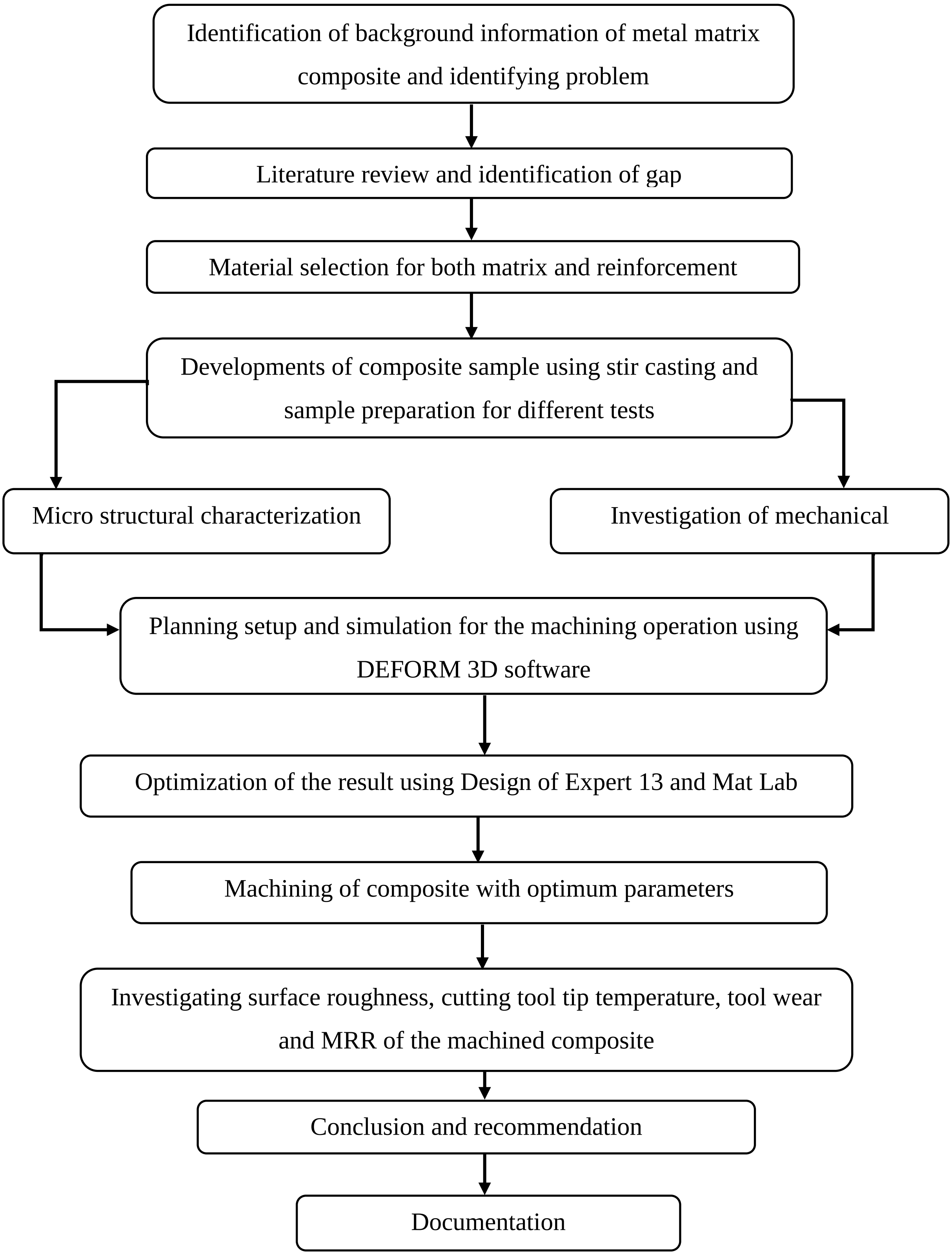

Figure 3.5 Research methodology flow chart

3.2.1 Identification of Parameters and Its Level

For industries that involve manufacturing, hybrid composites' machinability becomes essential. Thus, it is basically necessary to investigate how process variables affect the cutting forces while turning such hybrid composites in a dry environment. The parameters of a hybrid MMC material influencing the machining performance are the particle size, wt. %, temperature, hardness, the tool, its type and grade. In this research, the effect of fabrication process parameter (pouring temperature, stirring speed, stirring time) at constant level, weight percentage of reinforcement at 3 different level, and cutting process parameter (depth of cut, feed rate, and cutting speed) at three different level and surface roughness, MRR and tool wear at the optimum values of input machining parameters will be analyzed and identified.

From previously done literatures the optimum parameters (stirring speed, stirring time and pouring temperature) are selected to fabricate the three samples through stir casting process and these 3 samples are prepared for different tribological and mechanical testes in order to select the one material with best properties. The samples are developed at 800 rpm, 10 min and 720^{0}C Stirring speed, stirring time and pouring temperature respectively.

3.2.2 Weight % composition specifications for composites

The weight percentage (wt%) of the reinforcement has a significant impact on the generated composites' mechanical, corrosion, and wear properties. Thus, a literature review was performed to ascertain the weight percent composition of SiC and CeO_2 used in this research effort, and the researchers' subsequent work was used to estimate the weight percent composition of the reinforcement for each sample to be evaluated. By using semisolid stirring, two volume fractions (3 and 5 vol.%) of 1 mm-SiCp were used to reinforce the AZ31B magnesium matrix composites. A mass of one kilogram of AZ31B matrix alloy was used in each experiment. The matrix alloy was melted at 720 ^{0}C and cooled to 625 ^{0}C, resulting in a semi-solid state. Prior to stirring the semisolid melt for 20 minutes, 1 mm-SiCp that had been preheated to 650 ^{0}C was swiftly added. The liquid containing the melt and 1 mm-SiCp was quickly heated to 720 ^{0}C after 20 minutes of semisolid stirring. (Shen et al., 2015).

Mousavi et al. (2022) examined the microstructure and behavior of the heat cycle in the stir-cast AZ31/SiC composite. The AZ31/SiC composites were made by the stir casting method. Following alloying, the melt was mixed for ten minutes using a titanium stirrer containing five and ten weight percent of warmed SiC. In steel molds, composite ingots were cast.

Table 3.3 Experimental Design

S. No	Operating Conditions for Stir Casting Process	Reinforcement and their weight percentages			AZ31B
		CeO_2	SiC	Graphene	
1	Stirring Speed = 800 rpm	10%	5%		
2	Stirring Time = 10 min	7.5%	7.5%		
3	Pouring Temperature = 720^0C	5%	10%	4%	81%

3.2.3 Mass and Volume Estimation of Matrix and Reinforcements in Composites

The entire number of specimens needed for the machining process, microstructural, corrosion, wear, hardness, and compression tests was used to calculate the mass of reinforcement and matrix needed to construct AZ31B/SiC/CeO_2/Gr composite samples. A 20 mm diameter and a 100 mm length were used to prepare each sample. In the end, the reinforcing weight percentage (wt.%) has a significant impact on the mechanical and tribological properties of the composite materials. As a consequence, a review of the literature was used to identify the weight percent composition of SiC, CeO_2, and Gr used in this study. In this study, the weight proportion of reinforcements is 19% since most of the time; nanosized reinforcements have a major impact on the matrix when the weight percentage is greater than 3. The overall weight percentage of additional reinforcements should not exceed 30%.

The required volume of material for a cylindrical sample is calculated using eqn.

$$V = \frac{\pi}{4} D^2 * L \qquad (3.1)$$

Where,

V = volume of sample in mm^3,

L = sample length in mm, and

D = sample diameter in mm

Specimen sizes for different tests according to ASTM standard.

For hardness and microstructural test the specimen has a length of 8 mm and diameter of 18 mm.

For wear test the specimen has a length of 12 mm and a diameter of 6mm.

For compression test the specimen has a length of 8 mm and a diameter of 10 mm.

For the machining process the specimen has a length of 60 mm and a diameter of 20 mm.

For the removal of material by file, grinding and machining allowance 12 mm was considered.

L = hardness and microstructure (8 mm) + compression (8 mm) + Wear (12 mm) + machining (60 mm) + allowance (12 mm) = 100 mm.

D = 20 mm.

V = $\frac{\pi}{4}(20^2) * 100$ = 31,415.93 mm^3 = 31.4 cm^3

For three samples V_T = 31.415 cm^3 * 3 = 94.245 cm^3. The total volume of material required for three samples fabrication including both matrix and reinforcement materials is V_T = 94.245 cm^3

$$m_x = V_T * \rho_x * y \quad (3.2)$$

Where m_x is mass of reinforcement or matrix,

ρ_x is density of matrix and reinforcement and

"y" is weight percentage of reinforcement and matrix.

Table 3.4 Mass and Volume Fraction of Matrix and Reinforcements in Composite

Sample	AZ31B		SiC		CeO_2		Gr	
	V (cm^3)	Mass (g)	V (cm^3)	Mass (g)	V (cm^3)	Mass (g)	V (cm^3)	Mass (g)
Sample 1	25.45	45.0397	1.62	5.042	3.142	22.682	1.257	2.848
Sample 2	25.45	45.0397	2.42	7.563	2.356	17.011	1.257	2.848
Sample 3	25.45	45.0397	3.14	10.084	1.571	11.341	1.257	2.848
Total volume required	76.35 cm^3	135.119g	7.18 cm^3	22.689 g	7.069 cm^3	51.034 g	3.771 cm^3	8.544 g

Density of AZ31B =1.77 g/cm^3, Density of silicon carbide (SiC) = 3.21 g/cm^3, Density of cerium oxide (CeO_2) = 7.22 g/cm^3, Density of Gr = 2.267 g/cm^3

The composite's total weight = overall mass of AZ31B + overall mass of SiC + overall mass of CeO_2 + overall mass of Gr

Total weight of composite = 135.119 g + 22.689 g + 51.034 g + 8.544 g = 217.386 g

Total weight (mass) required for the work is 217.386 g.

3.2.4 Stir casting fabrication techniques

The composites were made by the stir casting process. To overcome the chemical processes occurring during the matrix material's liquid condition, the ingot material (AZ31D) was broken up and put into a graphite crucible. To minimize casting flaws and eliminate various gasses, the crucible and raw materials are warmed. In order to prevent oxidation during casting, high purity argon gas (99.9%) was utilized as an inert medium. Due to slag removal and oxidation losses, 10% of the extra alloy material was withdrawn. A pool was formed after reaching the necessary temperature of 770 °C. A traditional stirrer with an electronic variance and a graphite impeller spinning at 700 rpm creates the vortex. For uniform distribution in the molten metal, the SiC reinforcements that had been warmed to 200 °C were added to the vortex. The cylindrical mold made of gray cast iron that had been warmed was filled with the flowing molten metal. To increase their hardness and strength, the composite samples were quenched at room temperature. For a full day, a furnace was used to homogenize the cast specimens in order to remove internal tensions. (Kumar et al., 2022).

In composites, the volume percentage of micron SiCp varied in increments of 5 vol% from 5 to 15 vol%. The composites were made by stir casting in an argon-shielded resistance furnace. During the fabrication process, the alloy AZ31B was heated to a liquid and then cooled to a semisolid state at 620 ^{0}C. The warmed (650 ^{0}C) micron SiCp was then added to the semisolid melt. The composite melt was stirred for 10 minutes at 800 rpm using a 450 pitch stainless steel impeller. In composites, the volume percentage of micron SiCp changed in steps of 5 vol%, ranging from 5 to 15 vol%. The composites were fabricated in an argon-insulated resistance furnace by stir casting. During the fabrication process, the AZ31B alloy was heated to a liquid and then cooled to 620 ^{0}C, where it solidified into a semi-liquid state. Then, the semisolid melt was mixed with the warmed (650 ^{0}C) micron SiCp. The composite melt was agitated for ten minutes using a 450 pitch, 800 rpm stainless steel impeller (Shen et al., 2017).

For fabrication stir casting is used since it is simple and economical process. The matrix material is AZ31B and the reinforcements are SiC, CeO_2 and Graphene. First the reinforcements are mixed using ball milling then it is pre heated at 620 ^{0}C after that AZ31B is melted at 720^{0}C inside the furnace at the same time argon gas is constantly supplied to avoid burning or reaction with the atmospheric air then it is stirred before adding the pre heated reinforcements to reduce agglomeration of the reinforcement particles then the melted matrix is supplemented with the reinforcements. While stirring and the mixture was stirred for 10 min then pour it in to the mold cavity to produce the samples using this process three samples with different reinforcement ratio are produced as per experimental design.

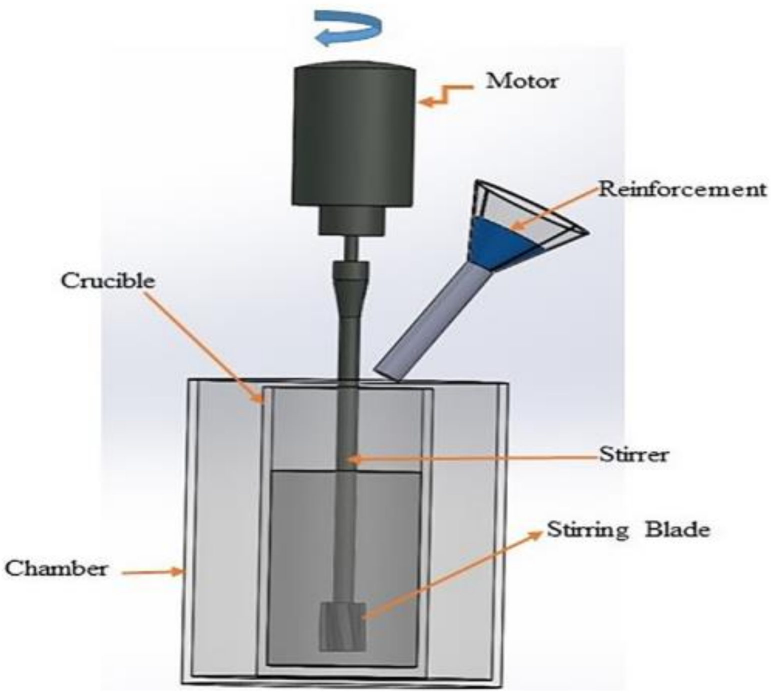

Figure 3.6 Schematic of Stir-Casting Machine (Islam et al., 2021).

3.2.5 Stir casting process parameters

The three primary process parameters for stir casting are temperature of pouring, speed of stirring, and stirring duration.

3.2.5.1 Stirring time

The right amount of stirring time is crucial because too little stirring time leads to uneven particle dispersion and the aggregation of reinforcement in some areas of the matrix. When stirring is not done for an appropriate amount of time, Particles of reinforcement are observed to detach from the matrix. Conversely, a too lengthy stirring period could result in the stirrer blade deforming.

3.2.5.2 Stirring speed

For the reinforcement to be distributed evenly throughout the matrix, a vortex must be created, and Stirring speed is directly in charge of for this. It also affects the flow pattern of the molten metal and the wettability of the combination of matrix reinforcement. It takes a high-speed mechanical or ultrasonic stirrer to properly distribute reinforcement throughout the matrix.

3.2.5.3 Pouring temperature

Maintaining a consistent velocity of pouring and elevated temperature of pouring will help to enhance casting quality and prevent gas entrapment. An increased pouring temperature would result in a reduction of porosity in the composite and better dispersion of reinforcement particles assimilated into the matrix.

3.2.6 Process flow of stir casting

The molten material is kept in a melting furnace as part of the casting apparatus. A feeder adds reinforcement from the top. The purpose of the furnace is to melt and heat the matrix substance. Additionally, it is equipped with a motor-driven mechanical stirrer with variable speed settings. To guarantee that the reinforcing material is properly mixed into the molten matrix material, the stirrer creates a vortex. As soon as the reinforcement and molten material are joined, poring becomes necessary to prevent the reinforced particles from sinking to the furnace's bottom. After stirring, reinforcement is combined with the matrix. Furthermore, heating the reinforcing material is necessary to stop the composite material from thermally deforming.

3.2.7 Specimen Preparation for Tests

Fabricated samples are prepared (machined) using lathe machine for mechanical, physical and tribological tests according to the ASTM standard.

3.2.7.1 Machining

The fabricated samples have cylindrical shape and rough surface finish. M460 GH Lathe machine is used for preparation of samples having ASTM standard size for different tests. Turning, facing and cutoff operations are done on the samples. The machined samples have good surface finish and accurate size.

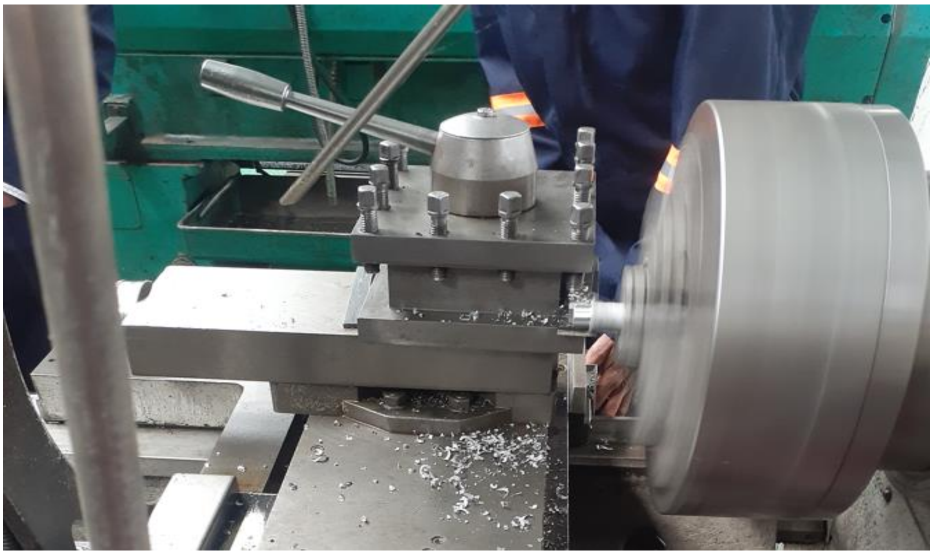

Figure 3.7 M460 GH Lathe machine during sample preparation

3.2.8 Microstructural characterization of composite

Microstructural characterization identifies the distribution of reinforcement inside the matrix, grain size and gain boundary and it also study the defects present in the fabricated samples like porosity, agglomeration, crack, fractography etc. Under microstructural characterization the samples are tested utilizing an X-ray diffractometer (XRD), an optical microscope, and a scanning electron microscope (SEM). As it is mentioned above the samples for each test are machined (prepared) using lathe machine according to ASTM standard but for the microstructural characterization further preparation is needed to see the surface of the sample through microscope. The main steps to prepare the samples for microstructural characterization are: grinding, polishing, etching and inspecting using microscope.

3.2.8.1 Grinding

Grinding is a process of rubbing the surface of the machined composite using different graded emery sheets of grid 240, 800, 1200, and 2000. Then rub it again after rotating the sample 90^0 to the previous direction to remove scratch from the surface & make it smooth.

3.2.8.2 Polishing

The AZ31B/SiC/CeO_2/Gr hybrid composite is then polished on RB 204 Metpol II model polishing apparatus. The polisher uses SiC abrasive for the grinding purpose and diamond suspension is used for the lubrication purpose. The speed is adjustable. The polisher makes the surface more smother than the grinding operation.

3.2.8.3 Etching

Etching is a process that uses chemical to see the grain boundary of the sample more clearly. The suitable etchant for AZ31B composite are mixture of 6g picric acid, 10ml acetic acid, 100ml ethanol and 10ml distilled water but picric acid was replaced with 5.52g sodium citrate and 0.48g citric acid since picric acid was not available. First sodium citrate and citric acid was dissolved in distilled water then acetic acid and ethanol was add and stir the mixture after that the sample was immersed using sample holder for 10 sec then to clean the chemicals from the sample surface it was inserted in distilled water then it was left in the air to dry. Finally it was inspected under optical microscope.

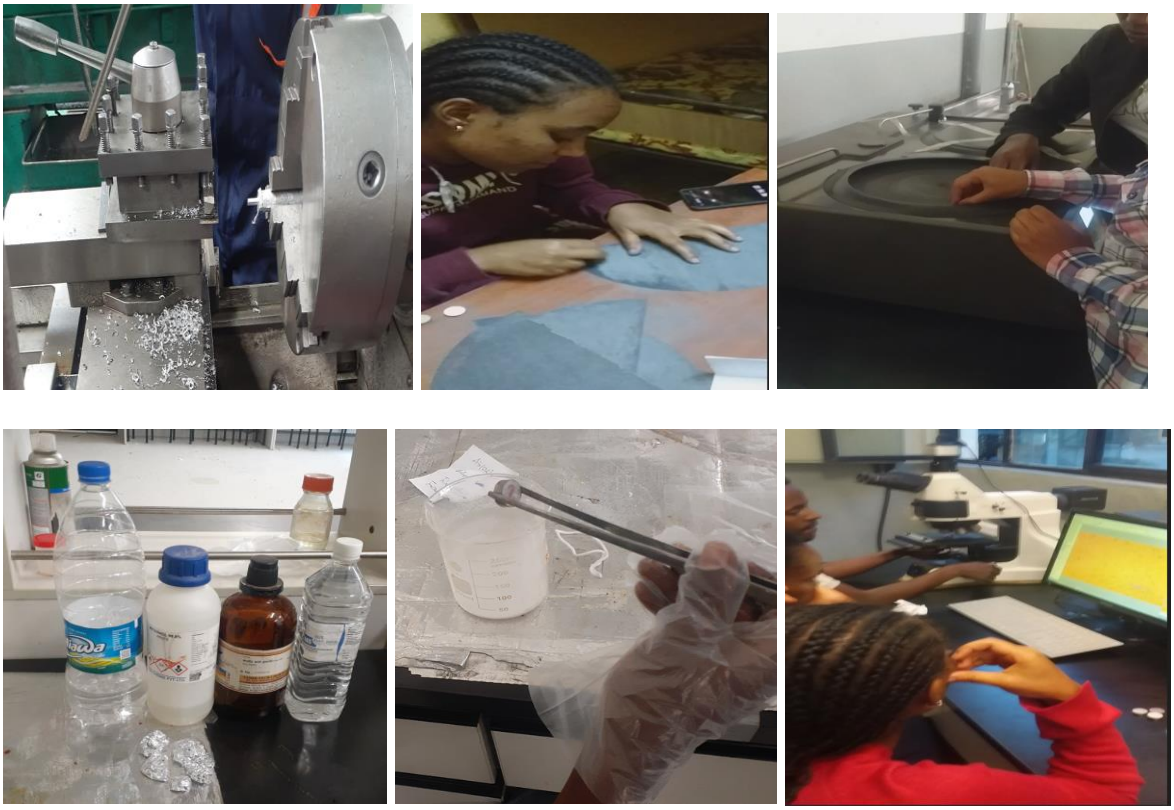

Figure 3.8 sample preparation

3.2.9 Optical Microscope (OM) and Scanning Electron Microscope (SEM)

The optical microscope Huvitz HR-300 (at ASTU, material lab) is used to view the distribution of reinforcement materials, grain boundaries, grain size, and other surface features. Solid item surfaces can be examined and described with a scanning electron microscope. SEM was used to analyze the fractography and morphology of the samples.

3.2.10 X-Ray Diffraction (XRD)

A Shimadzu Corporation (Japan) XRD-7000 X-ray diffractometer Maxima model was used to identify the crystalline phases and elements of Mg MMC samples. Appropriate sample preparation and sample retention methods were also used. Utilizing Cu-Kα radiation at 40 kV and 30 (mA) at 2θ value in between (10^o-80^o) at a scan rate of 3°/min, X-ray diffraction (XRD) was employed to examine the phase of the sintered samples at ASTU observation. For phase identification and quantitative phase analysis, Origin Pro-2022 was utilized. The matrix and reinforcement included in the sintered composite were analyzed in its crystalline phase.

The parameters of micro structure have estimated using the XRD peak analysis Gauss method of the Scherrer formula. Peak variance analysis for the XRD Gauss method allows for a more precise determination of the microstructural characteristics of materials, such as lattice strain and dislocation density (Venkateswarl et al., 2014); (Altuntaş et al., 2022); (Zhu et al., 2023)

The XRD data of AZ31B/SiC/CeO_2/Gr is used to compute the microstructural parameters, including crystalline diameters, mean squared lattice strain, root mean squared strain, and dislocation density, using the Gauss technique for X-RD peak profile analysis. We can quantitatively determine the link between the crystal grain size and the entire width at half maximum of the diffraction peak using the Scherrer equation.

The Scherrer equation for crystalline size;

$$D = \frac{k\lambda}{\beta cos\theta} \qquad (3.3)$$

Where, D crystallite size

λ XRD radiation of wavelength (μm)

K is Shape factor can be 0.62 - 2.08.

θ is Braggs angle in degree

β is line of broadening at FWHM in radians or measurement of the full width at half maximum of the radian peak located at any 2θ.

The number of dislocations per unit volume of the crystal is known as the dislocation density. XRD data related to crystalline size was used to make the determination.

$$\delta = \frac{1}{D^2} \tag{3.4}$$

Lattice strain is the local deviation of atoms in the crystal structure from their equilibrium positions. Mathematically calculated using the below equation.

$$\varepsilon = \frac{\beta}{4tan\theta} \tag{3.5}$$

3.2.11 Density and Porosity calculation

Density is the mass of matter per unit volume. The simple mass density of composite materials that is, materials made up of two or more distinct materials with known component densities can be computed using the Archimedes principle. Using the law of mixture, the theoretical density of the composite samples was determined to determine the densities of the reinforcement and matrix that are occupied in the composite.

A straightforward procedure was used:

1. Determine the densities of each member (or element) in the composite.

2. Divide the percentile contribution of each component in the composite by 100 after converting it to a decimal value (a number between 0 and 1).

3. Take the density of each related constituent and multiply it by the decimal.

4. Combine the items from step 3.

As a result, it was calculated using the following equation.

$$\rho_{th} = (\rho_{BM} * V_{BM}) + (\rho_{rein1} * V_{rein1})^n \tag{3.6}$$

Where;

V_{BM} and V_{rein1} represent percentile contribution in the composite,

ρ_{rein1} and ρ_{BM} represent matrix density the reinforcement density, respectively and,

n represents No. of reinforcement.

The actual densities for magnesium MMCs were also calculated using the Archimedes method. According to Archimedes, when something is submerged in water or another fluid, the buoyant force that results is equal to the product of gravity and the mass of the displaced water (i.e., the weight of the displaced water).

First, the composite samples were weighed in air and then suspended in distilled water. Therefore, the actual density was calculated according to the equation below.

$$\rho_{ac} = \frac{W_{air}}{W_{air} - W_{Water}} * \rho w \qquad (3.7)$$

In order to examine the actual sample density in relation to the theoretical density of the composites, the relative density of the samples was computed using the following formula.

$$\rho_r = \frac{\rho_{Ac}}{\rho_{Th}} * 100\% \qquad (3.8)$$

Where ρ_r, ρ_{Ac} and ρ_{Th} represents the relative density in %, actual and theoretical density in, g/cm^3 respectively.

Due to the fact that density and porosity affect the mechanical characteristics of composite materials, like hardness and compression strength, it is essential to analyze these parameters. Therefore, for material density and porosity, the smaller the better criterion was applied, and for material hardness and compressive strength, the greater the better criterion was applied (Bayu et al., 2021).

3.2.12 The composites' porosity

By measuring all of the void spaces in a composite, Porosity, also known as the void fraction, was calculated from the actual and theoretical densities. The following equation was used to calculate the porosity (ϕ), which is given as a range of 0 to 1 (or as a percentile 0% to 100%).

$$\phi = 1 - \frac{\rho_{Ac}}{\rho_{Th}} \qquad (3.9)$$

3.2.13 Hardness test

In order to determine whether or not the sample is appropriate for the required use, its hardness was tested using the Vickers hardness tester HVS-50 apparatus. The experiment was conducted using a Vickers indenter, which is a 136° pyramidal diamond indenter that leaves a square indent. Initially, the sample's surface was polished to a mirror-like finish using sandpaper grades 220, 800, 1200, and 2000. The cylindrical sample preparation method required by ASTM E3-95 was also used in accordance with ASTM E384-17 in order to conduct the hardness test on the magnesium MMC samples. The average result values in this investigation were obtained by applying 10 kgf forces progressively for 10 seconds at three distinct places. The hardness value was then ascertained by optical analysis of the resultant indent mark at a 10X magnification in order to measure the diagonal lengths. Using the following equation, the VHT machine subsequently performed an automatic analysis and pulled up the HV number.

$$HV = \frac{(Constant\ x\ test\ force)}{Surface\ area\ of\ indentation} = \frac{0.102 * 2F(sin360°/2\ )}{(d^2)} \qquad (3.10)$$

Where F is the applied force for indentation (kgf), d is the average length of the diagonals (d1 & d2) recorded by the indenter in millimeters, and HV is the Vickers hardness value (kgf/mm2).

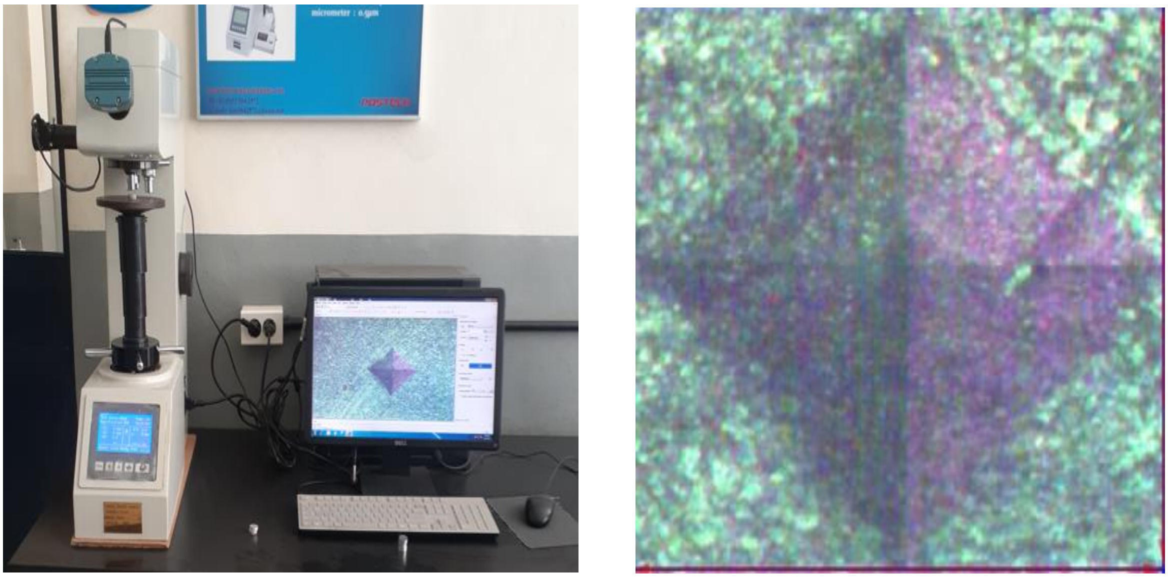

Figure 3.9 Vickers Hardness Measurements and test

3.2.14 Test for compression strength

A compression test is used to determine the compressive strength of a material and how elastic and compressive fracture materials (fractography) behave when crushing loads are applied. Using a universal testing machine (UTM), the samples in this inquiry underwent a 50 kN capacity uniaxial compressive load test at room temperature. The magnesium MMC specimens were prepared in accordance with ASTM E9-09 standard. They measured 10 mm in diameter and 8 mm in height, with an approximate length to diameter ratio of 0.8. The compressive strength was determined by gradually applying loads to the metal matrix composite samples made of magnesium alloy. For analysis and computation, the forces per cross sectional area of the samples, or applied compressive load, as provided by the following equation, was used.

$$UCS = \frac{F}{A} \qquad (3.11)$$

Where,

UCS stands for Ultimate compressive strength,

F is Ultimate compressive load and

A is Cross-sectional area.

A

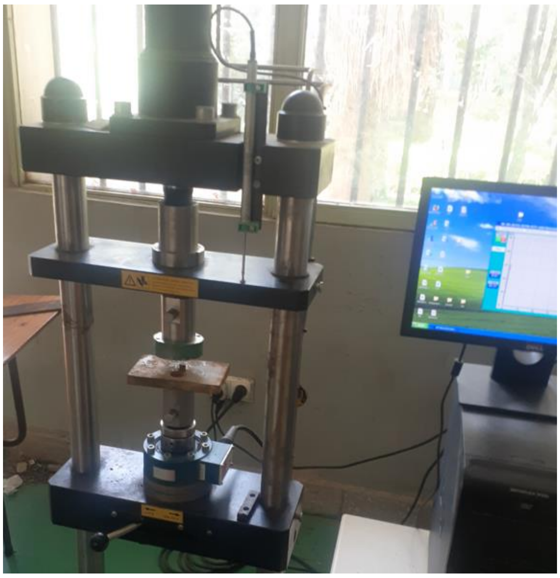

B

Figure 3.10 (A) UTM for the compression test (B) The compressed composite sample

3.2.15 Wear test

Wear is the phenomena that occur when a surface and materials that come into contact with it move in relation to one another, as happens when rubbing or striking. In this work, the magnesium MMC samples were subjected to a dry sliding wear test using a TR-20 Micro model Micro Pin on disk micrometer instrument. It has been used to evaluate sample wear rates and look at wear mechanisms. In this investigation, a wear test measuring 6 mm in diameter and 12 mm in height was conducted in accordance with ASTM G99-05 Standard. To evaluate the samples' wear characteristics, 30 N applied loads were applied to a 50 mm dia. wear truck. Furthermore, it was operated at a sliding speed of 400 rpm for fifteen minutes at room temperature. The wear rate of the Mg MMCs samples was calculated using the equation below.

$$W.R = \frac{W_b - W_a}{\pi * d * n * t} \quad (3.12)$$

Where;

W_b is weight of the samples before wear,

W_a is weight of the samples after wear,

WL is weight or mass loss ($W_b - W_a$),

d is wear truck diameter of disc,

n is revolution per minute and

t is time.

A B

Figure 3.11 (A) Micro Pin on disk micrometer apparatus (B) wear rate analyzing software

3.2.16 Corrosion test

To conduct corrosion testing, the specimens were submerged for one hour in a 3% NaCl solution. The length of the testing specimens was 7 mm, and their diameter was 4 mm. Three electrode cells were used for the electrochemical measurements, and an electrochemical analyzer (SP300 EC-LAB, Biologic Science Instruments, ASTU, Material science laboratory) was utilized. The standard calomel electrode (SCE) or mercury served as the reference electrode, while composite specimens including one centimeter of exposed magnesium served as the working electrodes. Graphite served as the auxiliary (counter) electrode. Tafel curves were produced by automatically varying the electrode potential at a scan rate of 1 mVS-1 from -250 to +250 mV versus corrosion potential (Ecorr). Stir casting-manufactured composites were subjected to experiments to examine the impact of reinforcing content on corrosion behavior. Numerous electrochemical properties are shown by the Tafel polarization curves, such as corrosion protection efficiency (μp%), corrosion rate (CR), corrosion potential (Ecorr), and corrosion current density (Icorr). Using the anodic and cathodic areas of Tafel plots, corruption potential (Ecorr) and corrosion current density (Icorr) were calculated. The corrosion rate was measured using the following formula:

$$Corrosion\ rate\ (in\ mpy) = \frac{CEwIcorr}{d} \tag{3.13}$$

Where;

C is the conversion constant (0.129),

Ew is the equivalent weight of the specimen (g) and,

d is the density of the specimen (g/cm3)

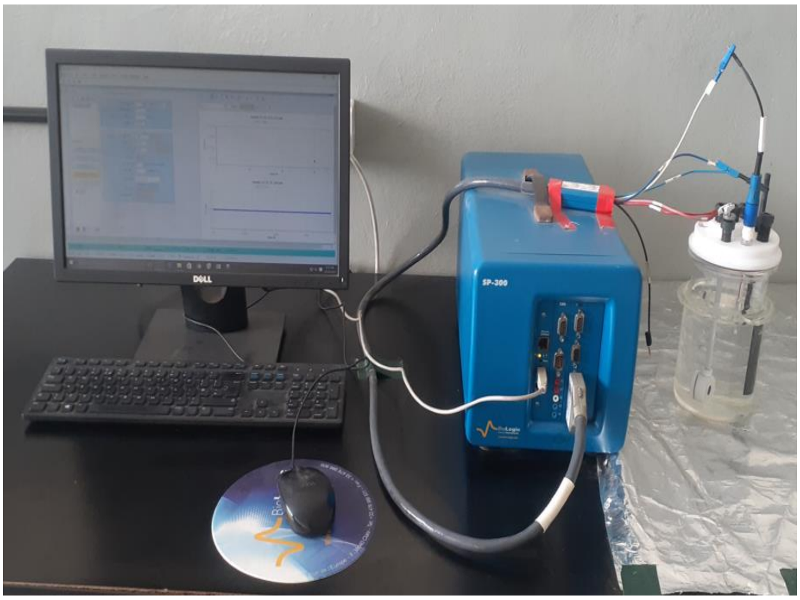

Figure 3.12 Electrochemical Analyzer

3.2.17 Finite element analysis of dry machining process

The current simulation experiment was conducted using DEFORM-3D v11 software. Simulations were carried out using FEM. Usually; the purpose of it was not only for heat treatment but also for forming process analysis. The turning process for the AZ31B/SiC/CeO_2/Gr hybrid composite was the current focus of this simulation. DEFORM was created for modeling machining and has an intuitive graphical user interface that makes data preparation and collecting easy, in contrast to the general-purpose algorithms used for FEM. A pre-processor, a simulation engine, and a post-processor are the three main components of DEFORM-3D.

After reading the database file and computing the real solution, the simulation engine appends the solution data to the database file; the postprocessor is used to view the simulation data after the simulation is completed. Pre-processors are used to generate, compile, or alter the data required for simulation analysis and to construct the required database file.

3.2.17.1 Input data

One needs to understand the material qualities required to specify a material in DEFORM in order to achieve a high degree of simulation accuracy. The material parameters that the user needs to supply are determined by the material types used in the simulation. It was assumed for this simulation that the holder was rigid and the material was a stiff-plastic work piece. In an isothermal turning problem involving rigid holder and plastic work piece, flow stress should only be computed for the work piece, per the instructions provided with the DEFORM 3D program. The flow stress data for the selected composite is obtained from the compression test. Most metals have strain-dependent flow stresses at room temperature. Most metals have strain-dependent flow stresses at room temperature. Empirical investigation revealed that Hollomon's equation can be used to depict the strain dependency of the flow stress.

$$\bar{\sigma} = K\dot{\varepsilon}^{n} \qquad (3.14)$$

Where $\bar{\sigma}$ is flow stress, $\dot{\varepsilon}$ is true strain, K is material constant and n is strain hardening constant.

The flow stress is mostly driven by the strain rate at higher temperatures, above the recrystallization temperature, and it can be approximated as equation below.

$$\bar{\sigma} = C\dot{\varepsilon}^{n} \qquad (3.15)$$

DEFORM 3D provides several ways for defining flow stress. For simulation of magnesium matrix hybrid composite power law is employed as constitutive equation to determine flow stress developed during machining.

$$\bar{\sigma} = C\bar{\varepsilon}^{n}\dot{\bar{\varepsilon}}^{m} + y \qquad (3.16)$$

Where, $\bar{\sigma}$ is flow stress, $\bar{\varepsilon}$ is effective plastic strain, $\dot{\varepsilon}$ effective strain rate, n is strain exponent, m is strain rate exponent, C is material constant and y represented initial yield value.

Initial yield stress is obtained from stress-strain curve during compression test. Yield stress is a point of limit for elastic behavior and beginning of plastic behavior. True strain and true strain were calculated using the equations below based on data obtained from compression test.

$$\varepsilon = log\ (1 + e) \tag{3.17}$$

$$\sigma = S\ (1+ e) \tag{3.18}$$

Where, ε and σ are represented true strain and true stress, respectively, while e and S are represented engineering strain and engineering stress respectively.

After the yield point, more plastic deformation requires an increasing load, although at a slower pace. Work hardening reduces the material's cross-sectional area while strengthening it. A typical load progression curve is the result of these two events together. The metal's forming process behavior is determined by the strain hardening exponent (n). It is easier to create higher value materials than lower value ones. As metals harden, their ability to work hardens decreases. These equations compute the strain rate exponent and the stain hardening exponent.

$$n = \frac{d\ log(\sigma)}{d\ log(\varepsilon)} \tag{3.19}$$

$$m = \frac{d\ log(\sigma)}{d\ log(\bar{\varepsilon})} \tag{3.20}$$

Strength coefficient K is calculated using following equation

$$log(\sigma) = log(k) + n\ log(\varepsilon) \tag{3.21}$$

3.2.17.2 Pre-processor by Simulation Control

In this experiment, an aluminum oxide coated tungsten-carbide tool was utilized to simulate turning AZ31B-10SiC-5CeO2-4Gr using FEM. The FEA was conducted using DEFORM 3D software. The simulation's settings included a start temperature of 20 °C, a shear friction factor of 0.6, a conviction coefficient of 0.02 N sec−1 mm−1 C−1, a heat transfer coefficient of 45 N sec−1 mm−1 C−1, and the absence of a coolant. Time or displacement reference can be used to control the cutting tool's movement. Up until the entire number of steps allocated is completed, the cutting tool will move the stroke length per step as stated. The entire step multiplied by the cutting tool velocity (displacement/step) equals the cutting tool's complete trip. Important factors are time and total step selection. In this example, the size ratio of the tool insert is 4. The tooltip's element edge length is 25% of the mesh size outside the tip, indicating that finer mesh was utilized there. In keeping with that, the work piece's size ratio was 7. Since the chip shape can only be characterized by finer mesh and the strain, stress, and temperature gradients are stronger at the work piece, this suggests that a finer mesh was used for the work piece than the tool.

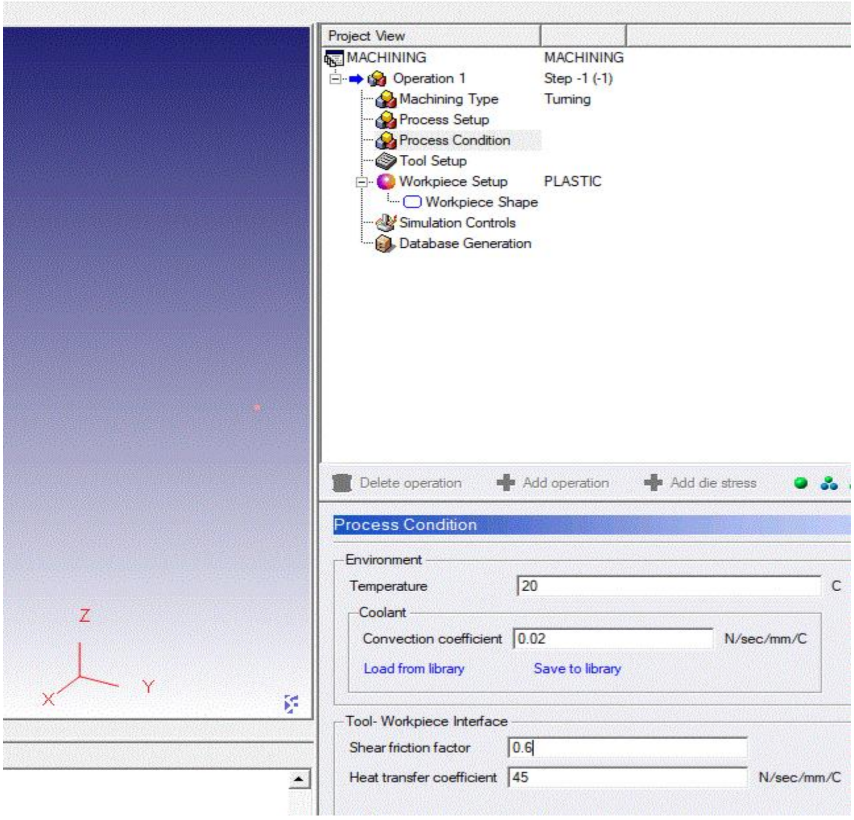

Figure 3.13 Process condition for turning operation on DEFORM 3D software

Materials

An object needs to have a material assigned to it if it is defined using mesh. The software database list contains information on the characteristics of the majority of standard materials. Moreover, the software makes it easier to create a new material model. The parameters of the composite AZ31B-10SiC-5CeO2-4Gr were computed and entered into the software using the power law equation and the findings of the compression test.

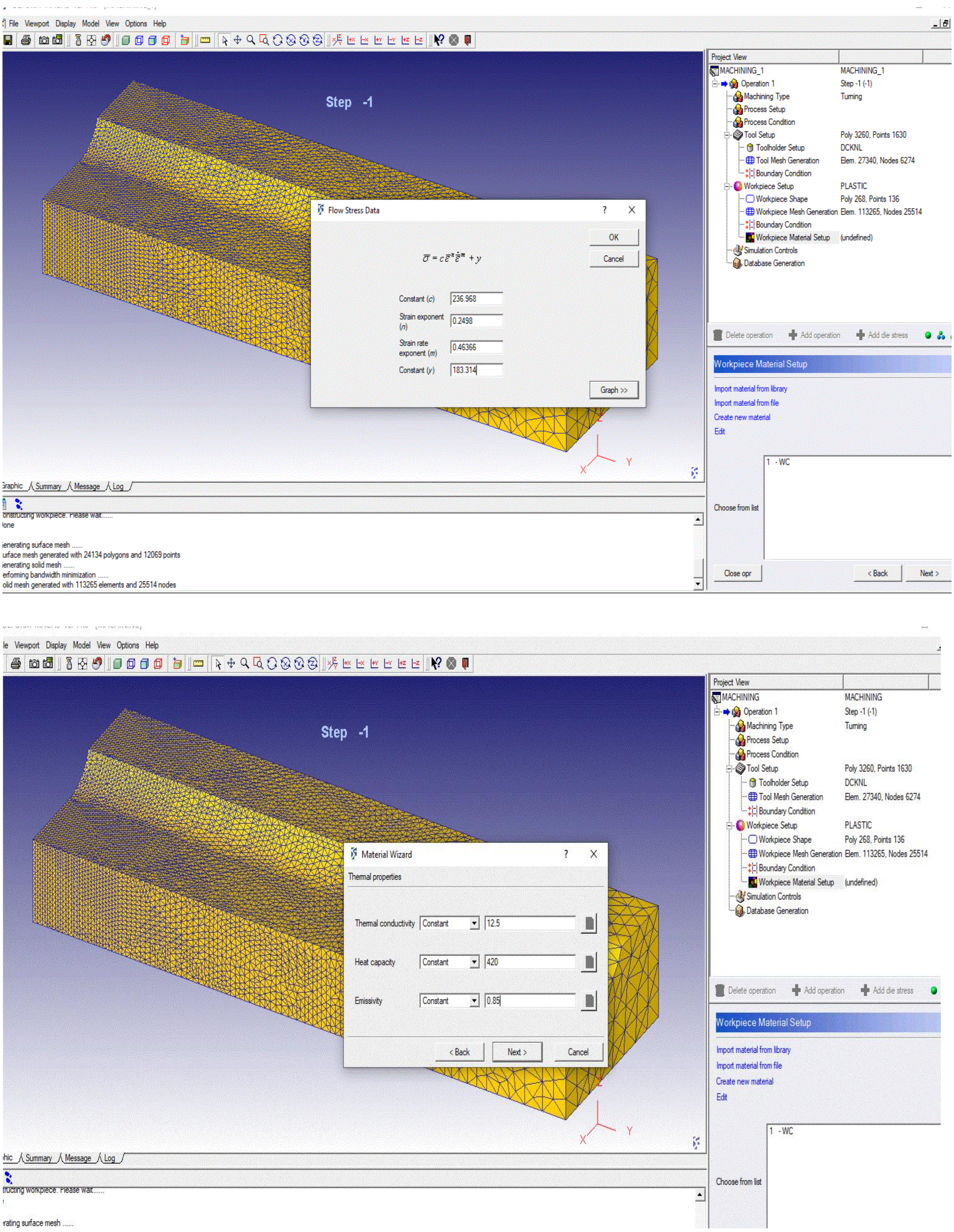

Figure 3.14 New material definition on the software database

Boundary condition

The boundary condition governs how an object's boundary interacts with its surroundings and with other objects. The object boundary exchanges heat with the surrounding environment most of the time. The turning operation is satisfied by the definition of the objects' movement boundary condition. The cutter can move in three dimensions: the cutting direction is on the +y axis, the feed direction is on the -x axis, and the depth of the cut direction is on the +z axis. The holder and work piece have their velocities set to zero in all directions.

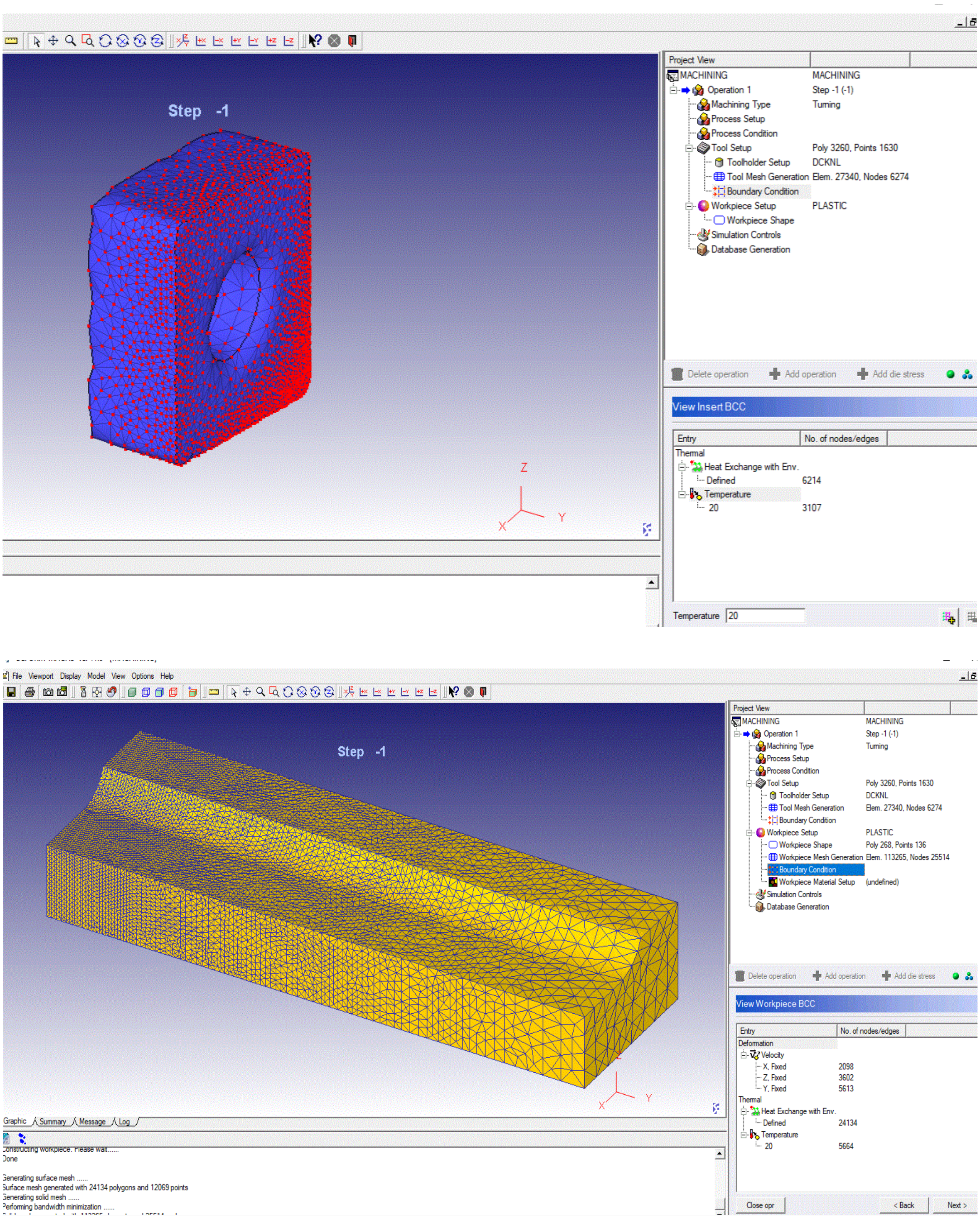

Figure 3.15 Boundary conditions for cutting tool and work piece

3.2.17.3 Simulation Engine

By selecting the run icon, the assigned simulation or numerical task that was defined in the pre-processor stage is processed further. The convergence information is displayed along with the execution information in the message window. While the problem is running, the simulation graphics option allows you to see the most recent step. For that step alone, various consequences can be seen, including MRR, tool wear rate, and cutting tool tip temperature. In the event of a constraint, the user has the option to terminate the problem or proceed until they receive a completion notification.

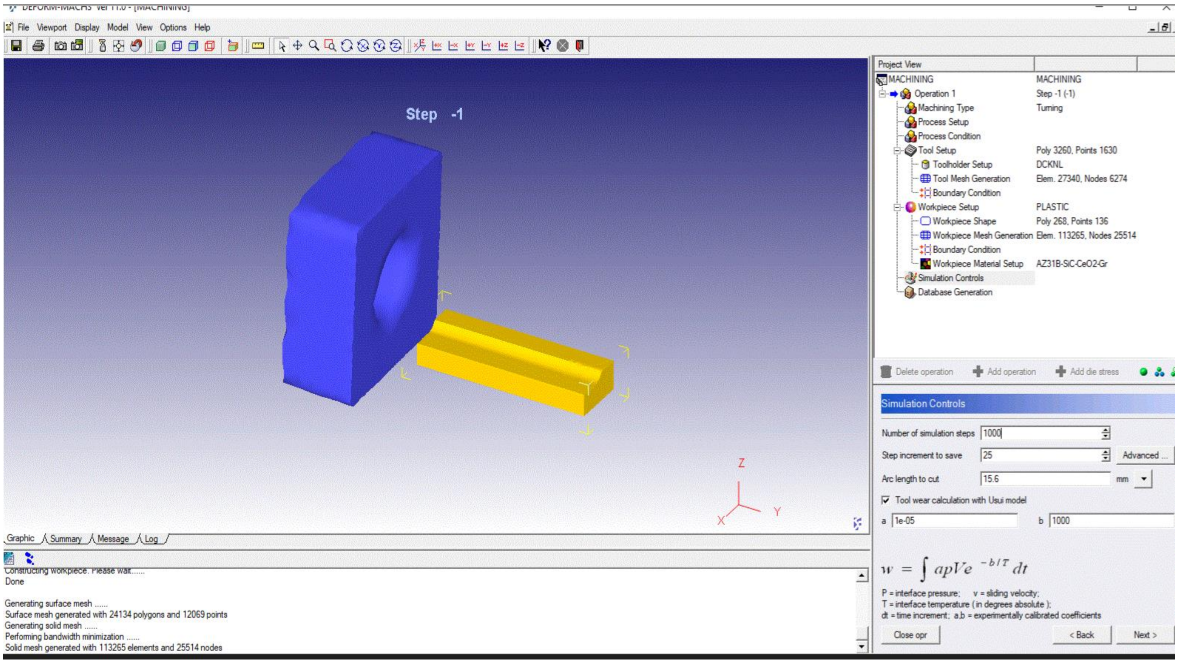

Figure 3.16 Simulation process at step 1

3.2.17.4 Post Processor

The results of this step were displayed, and they are also retrievable from the database. It is possible to gather the geometry following machining (turning) with tool movement at each stage from several angles. It is possible to analyze the contour plots that represent the state variable distribution on the objects. Plotting and extraction are possible for the graphs connecting any two state variables about various abscissas. The ability to adjust vision and range in accordance with analysis is offered by the graphic utility window.

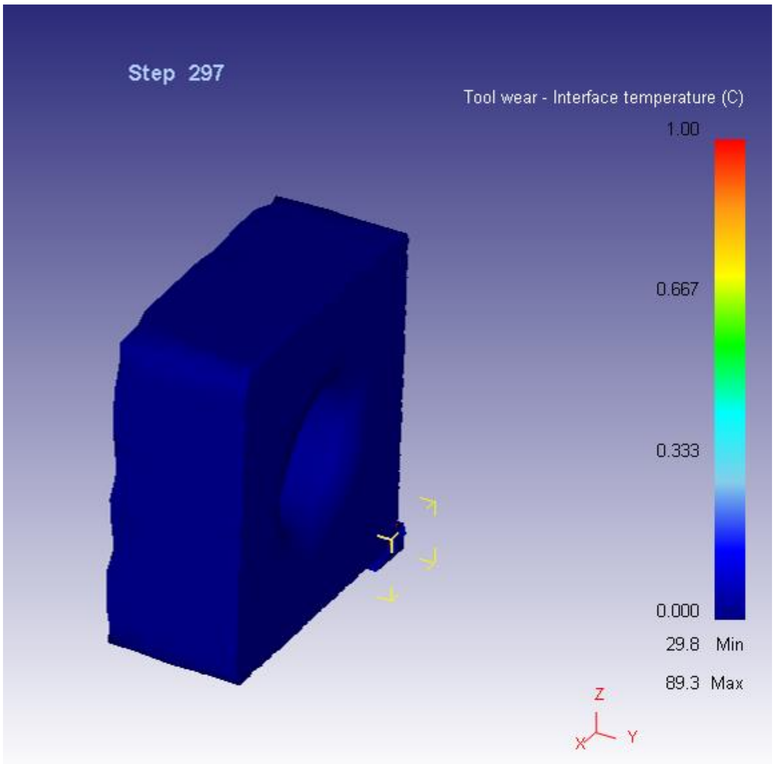

Figure 3.17 Post processor extracted data

3.2.17.5 Experimental design for simulation

Each machining technique's process parameters were chosen taking into account the required end products' attributes as well as different manufacturing considerations including cost effectiveness. Three machining process parameters cutting speed, feed rate and depth of cut were chosen in accordance with prior literature reviews and machine specifications. The cutting tool insert and work piece mesh sizes were both set at 25,000. Therefore, using multi-objective optimization with Design Expert 13 software to carry out the GRA, the impact of these parameters on the tool wear, MRR, and cutting tool temperature was examined.

Table 3.5 Levels and parameters of machining

Parameters	Unit	Levels		
		1	2	3
Cutting speed	m/min	40	80	120
Feed rate	mm/rev	0.08	0.24	0.4
Depth of cut	Mm	0.2	0.5	0.8

Figure 3.18 shows that when the machining specifically turning operation was started or when the simulation was run the cutter becomes in contact with the work piece and starts to remove the specified amount of material from the work piece the second image shows end of single turning operation or end process of removing unwanted material from the work piece.

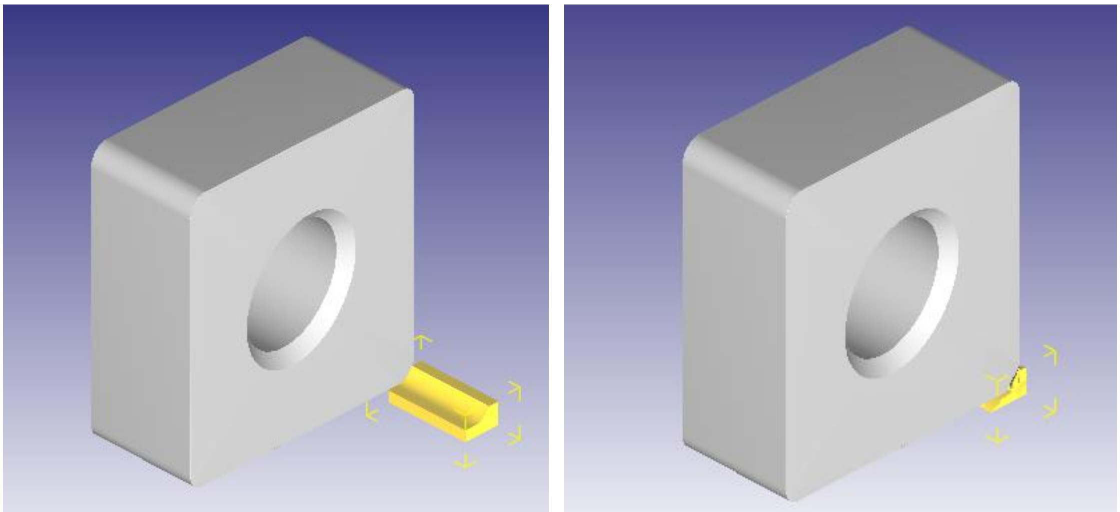

Figure 3.18 simulation set up of work piece and cutting tool at the starting and ending points of machining operation

3.2.18 Design of Experiment

One highly useful tool that allows us to model and analyze the impact of process variables on response variables is the design of experiments (DoE) technique. The response variable can be defined as an unknown function of the process variables, sometimes referred to as independent variables or design factors. There are numerous elements that can be taken into account when determining the machining parameters for a turning process. However, the literature review reveals that the most often used machining parameters by the researchers are feed rate (f, mm/rev), spindle speed (N, rpm), and depth of cut (d, mm). These were chosen as design elements for this investigation, with the assumption that other parameters would remain constant across the experimental domain. For this study project, Box-Behnken Design was utilized. For the response surface methodology (RSM), Box-Behnken Design (BBD) is specifically created to suit a second-order model, which is the main focus of the majority of RSM investigations. Unlike CCD, which requires five levels for each factor, the BBD only needs three levels. In addition to requiring fewer experimental runs, the BBD established a mid-level between the initial low and high levels of the components. The Box-Behnken design-based experimental plan has been followed in carrying out the experiments. The experimental design matrix is displayed in the table below, along with the experiment run order and coded values for the process parameters.

Table 3.6 Matrix of trial layout

Run	Cutting speed (m/min)	Feed rate (mm/rev)	Depth of cut (mm)
1	80	0.24	0.5
2	120	0.24	0.2
3	80	0.4	0.2
4	120	0.08	0.5
5	80	0.4	0.8
6	80	0.24	0.5
7	40	0.4	0.5
8	80	0.24	0.5
9	80	0.08	0.2
10	80	0.08	0.8
11	40	0.24	0.8
12	120	0.4	0.5
13	120	0.24	0.8
14	40	0.24	0.2
15	40	0.08	0.5

3.2.18.1 Analysis of Variance (ANOVA)

Finding the parameters that significantly affect the quality characteristic was the goal of the analysis of variance (ANOVA). The statistical method called ANOVA is employed to determine the impact of each control parameter. Using the percentage contributions of each control component, the corresponding effects on the performance parameters were quantified by analysis of variance. A significance threshold of 5%, or a 95% level of confidence, was considered in this research. Whether or not there is a statistically significant difference in the output characteristics is demonstrated by the results of an ANOVA. In an ANOVA analysis, values above 0.05 are not deemed significant; those below 0.05 are. The percent contribution represents the percentage contribution of each model term to the total sum of squares often; the % contribution provides a rough but accurate indication of the relative importance of each model item. Using analysis of variance, the percentage contribution of every significant parameter was found.

Each term that was used in ANOVA table were explained here

Block: The response's block variance is shown by the block row. Block variation is eliminated from the examination. Since blocks are thought to be a hard-to-change, non-replicated factor, they are not evaluated (no F or p-value).

Model: The model row displays the overall model test for significance along with the amount of variation in the response that the model can account for.

Words: The model is tested separately after being divided into distinct words.

Residual: The residual row displays the amount of response variation that is still unaccounted for.

C, or Total, is the variation around the mean of the observations.

df, or degrees of freedom, is the number of estimated parameters used to calculate the sum of squares from the source.

Mean Square, or variance, is the sum of squares divided by the degrees of freedom.

F Value is a test used to compare the mean square from the source to the mean square from the residual.

Probability > F: (p-value) Chance of observing the observed F-value in the event that the null hypothesis that is, no factor effects is correct. Low probability values need the null hypothesis to be rejected. The probability is equal to the integral under the F-distribution's curve, which is located outside of the observed F-value. To put it another way, the source has tested significant if, by default, the Prob >F value is much smaller than 0.05. It is likely that significant model terms actually affect the answer. When there is a considerable lack of fit, the model is unable to account for the observed replicate variance in the data.

Mean: The total squares for the mean's influence. The degrees of freedom for each source are listed in the column with the name "df." The number of successively applied model coefficients in the response surface methodology represents the total degrees of freedom, line by line.

For the sake of this mixture model, let q be the number of components in a mixture. In a mixed model the degrees of freedom for the linear terms are (q-1), not q, because the sums of squares are corrected for the mean.

3.2.19 Multi objective optimization by using Genetic Algorithm and Desirability

When trying to improve one objective at the expense of another, when dealing with complex optimization situations where the distinct goal functions of the problem conflict, multi-objective optimization is a helpful tactic. In this work, the optimization method is a hybrid of a desirability function and a genetic algorithm. This optimization's main objective was to determine the cutting depths, feed rates, and speeds that would maximize MRR while simultaneously reducing tool wear and surface roughness (Ra). Regression analysis was performed on these output responses using the expert 13 software design's regression model. In order to perform multi-objective optimization using a genetic algorithm, regression models of each output response were written into a MATLAB workspace. Important variables were also written, such as the number of variables, upper and lower bounds on the input process parameters (feed rate, cutting speed, and depth of cut), as well as any other necessary inputs. The optimization process then began by choosing the population type, which is used to specify the type of input to the fitness function. The starting random population composed of a viable population satisfying all linear constraints and limitations.

3.2.20 Turning operation on CNC lathe machine

Lathes are another name for turning machines. They come in a range of sizes and designs and are used to perform a variety of machining operations such as drilling, turning, and facing while maintaining a stationary cutting tool. Based on the available control types, turning machines can be categorized. The motion of the cutting tool must be managed by the operator of a conversional lathe while the machine is turning. As an alternative, computers are capable of controlling turning machinery. They are called as in this case computer numerical control, or CNC, lathes, and they operate by utilizing a preprogrammed code to turn items. Because they offer extremely high precision, these lathes are the recommended choice.

Figure 3.19 CNC lathe machine

3.2.21 Measurement of Surface Roughness

The VOGEL Surface Roughness Tester, a surface contact profilometer roughness tester with 65711 models, was used to measure the surface roughness. Its model is shown in the photo below. The roughness value in micrometers (µm) is displayed by this surface roughness tester. The VOGEL Surface Roughness Tester 65711 has a measurement range of 0.02 to 10 micrometers. The tester's detecting device has a stylus that is used to map out even the smallest surface imperfections. The instrument's liquid crystal display processes and displays digitally the vertical stylus motion that occurred throughout the tracing.

Figure 3.20 profilometer roughness tester

3.2.22 Tooltip Temperature measurement

The temperature at the tool's tip was measured using an infrared thermometer, and the relationship between temperature, tool wear, and cutting parameters was examined. During the machining phase of each run, the cutting zone's temperature was monitored. The unit optics detects the energy that is transmitted, reflected, and released. It then collects and concentrates this energy onto a detector. The electronics of the unit process the data and display the temperature reading on the screen. If a device has a laser, it is only used for aim. By grabbing hold of the meter's handle and pointing it in the direction of the surface that needs to be measured. To activate the meter and begin testing it, pull and hold the trigger. Continue pushing the trigger to keep the laser pointer focused on the cutting zone. The LCD screen will show that the reading is being retained when the trigger and hold are released. We can use two different temperature units: ^{0}C and ^{0}F. The temperature was measured using an infrared thermometer, as seen in the image below;

Figure 3.21 Infrared thermometer

3.2.23 Measurement of Tool Wear

An optical microscope (Model: Huvitz HR – 300 series, with magnification power of X50, X100, X200, 500, X1000) is utilized to assess the tooltip wear and tool wear pattern following each experimental run of turning AZ31B-10SiC-5CeO_2-4Gr.

3.2.24 Measurement of Rate of Material Removal (MRR)

The quantity of material extracted in a specific amount of time, or a machine's material removal rate, is what ultimately determines how productive it is. With large-batch production and roughing processes, maximizing the rate of material removal is crucial. However, it impacts surface roughness, tool life, cutting temperature, and the overall efficiency of the machining process during finishing operations. Because finishing usually has a low MRR, In the turning process, low cutting parameters are often used to achieve minimal tool wear, low tool tip temperature, and low surface roughness. The following formula has been used to determine the material removal rate in the current experiment.

$$MRR = V * f * d \qquad (3.22)$$

Where: The feed rate, expressed in mm/rev, is represented by f; the spindle speed, expressed in m/min; and the depth of cut, expressed in mm, for each turn is represented by d.

Table 3.7 Equipment and Tools Used in the Research Work

S. No.	Tools	Function
1.	Stir casting machine	To fabricate the composites
2.	Lathe machine	To prepare the samples for each test according to ASTM standard
3.	Polisher	To file or grind the surface of the sample to make it smooth and to be able to see the surface using optical microscope easily.
4.	Optical microscope	To see the distribution of the reinforcements and grain boundary at the surface level
5.	XRD tester	To know the phase of the fabricated sample
6.	Scanning electron microscope (SEM)	To see the surface, fractography and wear type of the samples
7.	Universal testing machine	To test compression strength
8.	Pin on disk apparatus	To test the wear rate
9.	Vickers hardness tester	To determine hardness of the samples
10.	Analytical precision balance	To measure the weight of matrix, reinforcement and fabricated sample

11.	CNC lathe machine	Machining of the sample to know the surface roughness at optimum parameters
12.	Design expert software	Optimization of machining parameter using BBD model
13.	Deform 3d	To identify the output responses for the optimization purpose
14.	Mat lab software	To determine the global optimum parameters for machining
15.	Potentiator	To determine corrosion rate

CHAPTER-FOUR

RESULTS AND DISCUSSIONS

4.1 Introduction

In this chapter the results of all tests and the secondary operation are discussed. Microstructural characterization, density measurement, compression test, wear test, hardness test and corrosion tests for the fabricated samples were analyzed and discussed. The sample with best property was selected and the simulation on DEFORM 3D software, the optimization process on design expert 13 using BBD response surface methodology, Mat lab for the multi response optimization and machining (turning) operation using the optimum parameters were analyzed and discussed. Lastly, an analysis was conducted on the chosen composite's surface roughness, tool wear, cutting tool tip temperature, and MRR.

4.2 Analysis of fabricated sample properties

Three different AZ31B/SiC/CeO_2/Gr composite materials are fabricated through stir casting process using constant pouring temperature, stirring speed and stirring time by varying the weight percentage of SiC and CeO_2 to analyze the effects of the reinforcements on the base material.

Table 4.1the composite's composition and sample designation

Sample code	Composition in wt. %
S1	AZ31B-10%CeO_2-5%SiC-4%Gr
S2	AZ31B-7.5%CeO_2-7.5%SiC-4%Gr
S3	AZ31B-5%CeO_2-10%SiC-4%Gr

4.2.1 Diffraction of X-rays (XRD)

The diffraction pattern of X-rays of AZ31B-5SiC-10CeO_2-4Gr (S1), AZ31B-7.5SiC-7.5CeO_2-4Gr (S2), and AZ31B-10SiC-5CeO_2-4Gr (S3) was found at a scan speed of 3°/min, in an angle ranging between (10°-2θ-80°). As illustrated in Figure 4.1 for ceramic materials, the diffraction peaks of the samples were compared to XRD-JCPDS files of different materials. Since modest percentages have been added, the SiC, CeO_2, and Gr reinforcement in the AZ31B matrix can be seen as distinct little peaks in XRD plotted graphs. The composite matrix contains additions (SiC, CeO_2, and Gr) and AZ31B (high intensity peak), as indicated by several indicators and XRD-JCPDS.

The strength of the reinforcement peaks rose as the percentage of reinforcements increased. Because of the elevated concentration of AZ31B, it was noted on the tallest peak at (2θ= 37°) and in other peak at (2θ=74^0). A graphene peak point was recoded at an angle of (2θ = 33° and 70^0), and silicon carbide was generated at (2θ = 35° and 63^0). The rest peaks at (2θ=47° and 56°) cerium oxide has been detected. Due to the low weight percentage, the reinforcements' peak intensity is smaller than that of the matrix and may even be below the limit for detection of the XRD technique.

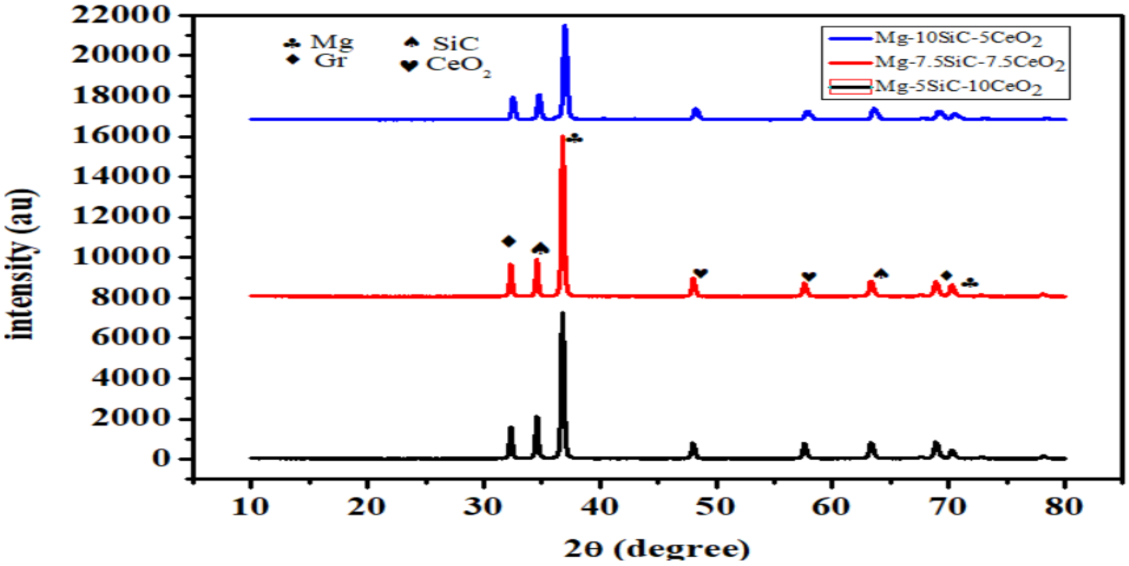

Figure 4.1 XRD spectrum of AZ31B-CeO_2-SiC-Gr composite

4.2.1.1 Dislocation Density and Lattice Strain of Composited Material

Since melting, pouring and stirring had processed during the fabrication of magnesium based composite materials, the particles can interact and get circulated in the matrix. Although these particles should flow uniformly, there was a possibility that defects like dislocations and lattice strain may emerge due to stirring speed, stirring time, and pouring temperature.

Both dislocation density and lattice strain had been calculated in the table below. According to Table 4.2, When the proportion of silicon carbide reinforcement decreased from (10-5) wt% and the percentage of cerium oxide increase from (5-10), there was a decrease in crystalline size, an increase in lattice strain, and a rise in dislocation.

Table 4.2 Crystalline Sizes, Dislocation Density and Lattice Strain Experimental Calculation

Sample	Peak 2θ (^{0})	FHWM β (^{0})	D (μm) $D = \frac{k\lambda}{\beta \cos \theta}$	Dislocation density $\delta * 10^{-3}$ μm^{-2} $\delta = \frac{1}{D^2}$	Lattice strain $\varepsilon * 10^{-3}$ $\varepsilon = \frac{\beta}{4 \tan \theta}$
Sample 1	32.53781	0.34104	25.34446	1.556804	5.099066
	34.77161	0.33823	25.70613	1.513305	4.713397
	37.00438	0.3751	23.32611	1.837872	4.890907
	48.27974	0.45034	20.19032	2.453091	4.384577
	57.90362	0.59009	16.06943	3.872568	4.654206
	63.63412	0.57803	16.89297	3.504193	4.065079
	69.24802	0.67018	15.04537	4.41768	4.235088
	70.61983	0.73768	13.78359	5.263508	4.544317
Average			**19.5448**	**3.052377625**	**4.573329625**
Sample 2	32.33428	0.281	30.74381	1.057997	4.229295
	34.57569	0.27195	31.95421	0.979363	3.812601
	36.78977	0.28944	30.21061	1.095673	3.79761
	48.04193	0.35322	25.71791	1.511919	3.458215
	57.62802	0.39145	24.1917	1.708706	3.105083
	63.36592	0.43691	22.31698	2.00784	3.088746
	68.95316	0.45744	22.00344	2.06547	2.906682
	70.31397	0.51067	19.87335	2.531966	3.163741
Average			**25.8765**	**1.61986675**	**3.445246625**
Sample 3	32.34144	0.25984	33.24803	0.904624	3.909905
	34.58457	0.26124	33.26503	0.9037	3.661452
	36.79916	0.2797	31.26348	1.023117	3.668812
	48.04706	0.32854	27.6504	1.307968	3.216197
	57.62252	0.3965	23.88295	1.75317	3.145499
	63.36025	0.42516	22.93305	1.901413	3.006012
	68.93998	0.4805	20.9458	2.279324	3.053964
	70.3051	0.48608	20.87758	2.294244	3.011894
Average			**26.75829**	**0.0001820388**	**3.334216875**

From sample one to sample three, the crystalline size increases (from 19.5448m to 26.75829m). However, the dislocation density decreases from 3.052377625μm^{-2} to 0.0001820388μm^{-2} and the lattice strain decreases from 4.573329625 to 3.334216875. In this study, SiC up to 10% addition to AZ31B metal matrix composites demonstrated a reduction in lattice strain and dislocation density. The results in Table 4.2 lead to the conclusion that the dislocation densities and lattice strain of composite materials rise when the crystalline size falls and vice versa.

4.2.2 Optical Microscope

Optical microscopy (OM) was used to measure the scattering of the reinforcing fragments within the matrix of AZ31B, as indicated in Figure 4.2. The image below also shows before and after etching. After being etched for ten seconds in a solution containing 5.52g sodium citrate, 0.48g citric acid, 10ml acetic acid, 100ml ethanol, and 10ml distilled water, the grain boundary is depicted in the third column. This means that etchant has a big effect on the grain boundary and facilitates better cleaning.

(S_1)  100µm (before etched)	(S_1) 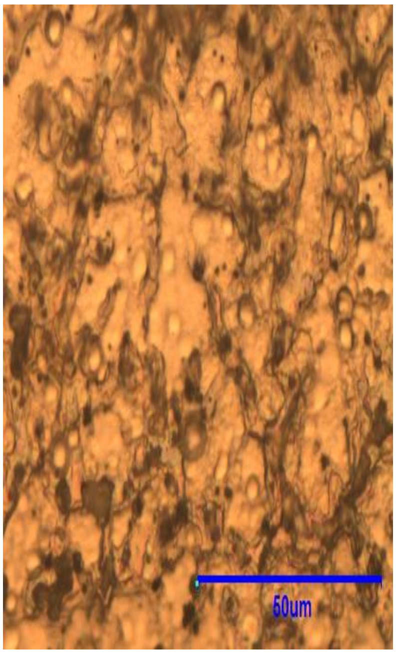 50µm (after etched)	(S_1) 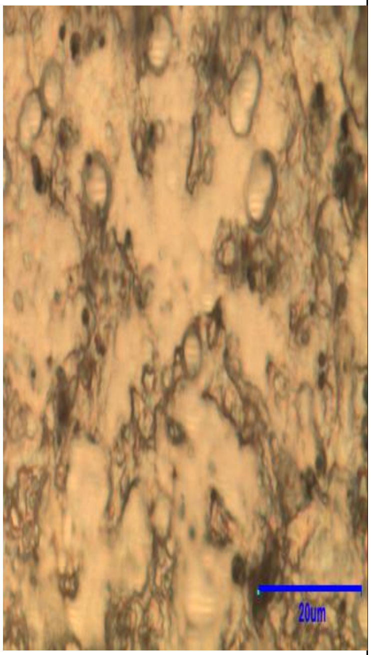 20µm (after etched)
(S_2)	(S_2)	(S_2)

 100µm (before etched)	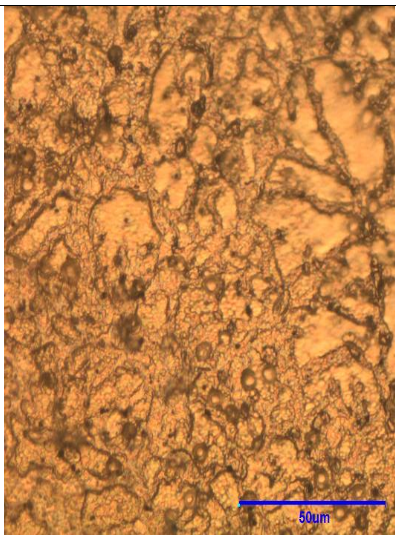 50µm (after etched)	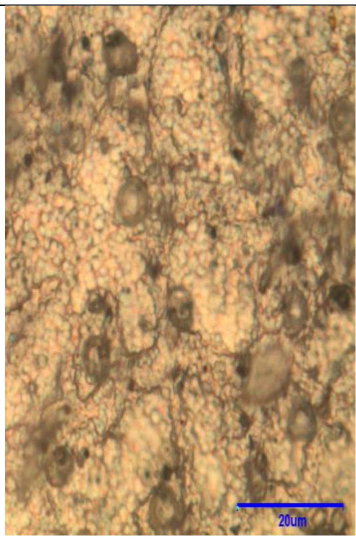 20µm (after etched)
(S_3)  100µm (before etched)	(S_3) 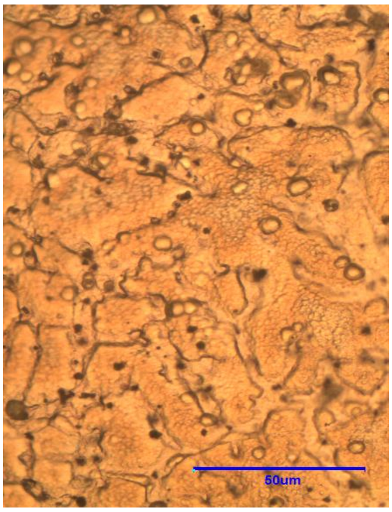 50µm (after etched)	(S_3) 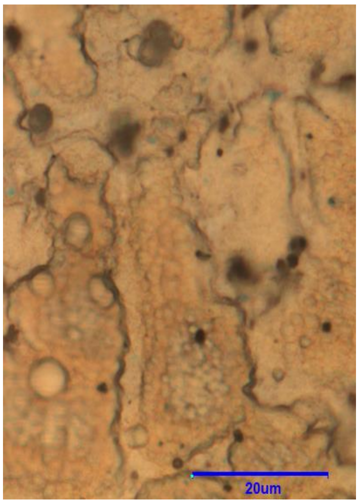 20µm (after etched)

Figure 4.2 optical micrographs of AZ31B-SiC-CeO_2-Gr composite samples before and after being etched at different magnification

4.2.3 Scanning electron microscope (SEM)

4.2.3.1 Surface morphology analysis

Research on reinforcing distribution in composites is essential because it affects the final properties of stir-casted composites in a big way. The SEM analysis showed that, with the exception of sample two (S2), the particles were evenly dispersed.

The hybrid AZ31B composite, with some pore spaces created by the evenly dispersed SiC and CeO_2 reinforcement on the AZ31B matrix, is depicted in Figure 4.3. The reinforcements (SiC and CeO_2) for S1 and S3 are demonstrated to be uniformly distributed throughout the AZ31B matrix and to show little to no agglomeration. But compared to S3 S1 has little agglomeration. There is also notable porosity and particle agglomeration in sample S2, which could be the outcome of an interaction between equivalent concentrations of reinforcements (SiC and CeO_2). When hard particles are added to a magnesium matrix, the poor mixing may generate some strained lines, broken lines, particle displacement that causes the composite to agglomerate, and some porosity holes formed by the hard particles.

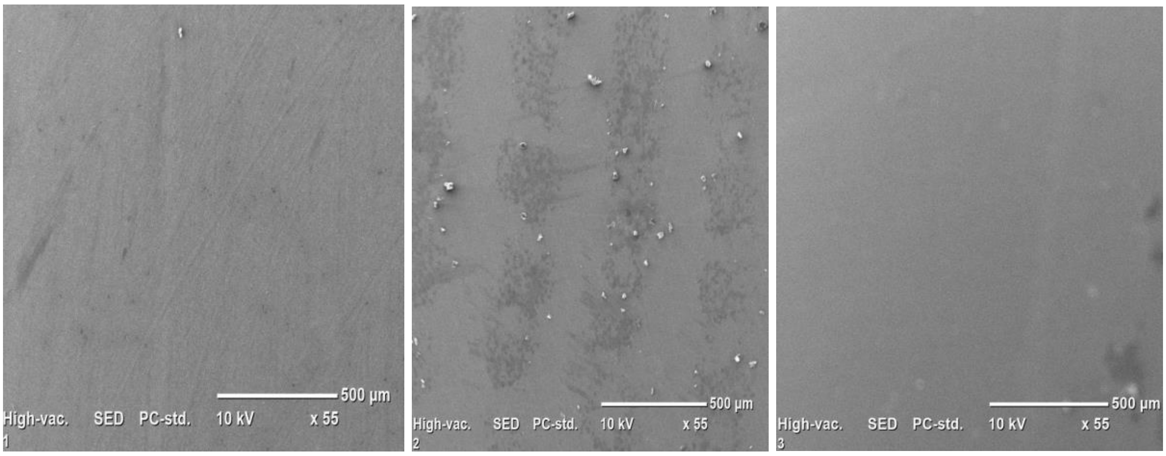

Figure 4.3 SEM micrographs of AZ31B-SiC-CeO_2-Gr composite samples at 500µm

4.2.4 Density and Porosity Measurement

The density of the matrix AZ31B is less than the reinforcing ceramics (SiC, CeO_2 and Gr) these increased the density of the base metal. The density of AZ31B, SiC, CeO_2 and Gr are 1.77, 3.21, 7.22 and 2.267 g/cm^3 respectively. SiC has lower density than CeO_2 so S3 (sample three) has lower density than the other samples since it contained 10% of SiC. CeO_2 has higher density so S1 has the highest actual density which is 1.7874 than the rest fabricated samples. So addition of SiC, CeO_2 and Gr increased the actual, theoretical and relative density of AZ31B.

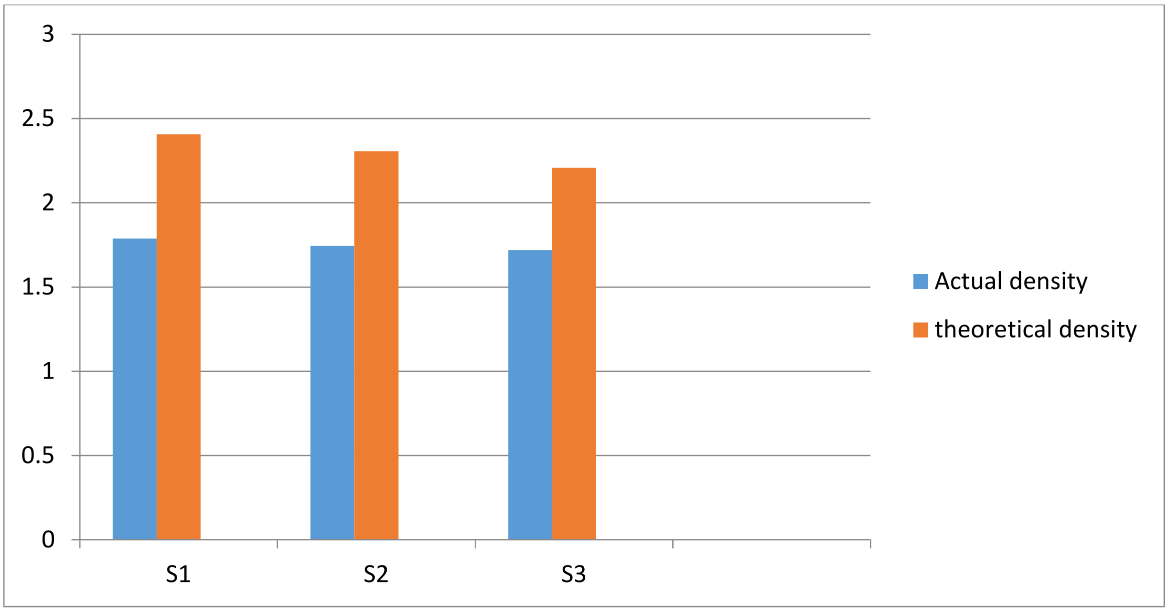

Figure 4.4 Actual and Theoretical densities of AZ31B-SiC-CeO_2-Gr composite

4.2.5 Porosity of Composite

Porosity was calculated from the actual and theoretical densities by measuring the total void space within the composite. Particles addition in the base matrix, trapping air between them, and interconnected in nature the main reason for generation of voids, therefore the percentage of porosity increases with the number of particles added and the porosity increases as the reinforcement content increases. Porosity decreases when relative density increases and vice versa.

Table 4.3 Density and Porosity measurement

Sample	Actual Density (g/cm^3)	Theoretical Density (g/cm^3)	Relative Density (%)	Porosity
S_1	1.7874	2.40688	74.26	0.25738
S_2	1.7436	2.30663	75.59	0.2441
S_3	1.7188	2.20638	77.9	0.2209

From Table 4.3 it was understood that when the variance between the experimental density and theoretical density increase (percentages of relative density decreased) there is high probability of the composite to have porosity. So minimum porosity was obtained in sample three (S3), due to high relative density and less content of CeO_2 which have large variance within base metal AZ31B density.

4.2.6 Hardness

The test was done using Vickers hardness tester HVS-50. The Vickers hardness value of stir casted AZ31B/SiC/CeO_2/Gr hybrid composites with varying reinforcement contents is shown in the appendix. The average hardness values for S1, S2 and S3 are (88.467, 95.367 and 111.2) respectively. Sample 3 (S3) has the highest hardness value, possibly 111.2 HV greater than the matrix material AZ31B hardness of 83 HV. The inclusion of ceramic particles, notably SiC and CeO_2, causes the volume percent of the reinforcement to vary, which in turn affects the samples' hardness ratings. Every manufactured sample has a harder value than the matrix material (AZ31B). Sample 3 is the hardest sample in which hardness of the matrix increases by 34% when 10 weight percent of silicon carbide particles and 5 weight percent of cerium oxide are added to matrix metal (AZ31B). Sample two equal amount of (7.5 wt% SiC and CeO_2) 15% increment in hardness and in sample three (10 wt% SiC and 5 wt% CeO_2) 6% increment were recorded. The additions of SiC and CeO_2 have increased the hardness, however with increment of CeO_2 more porosity is existed which affects the hardness of composite. As weight percentage of SiC increases up to 10 wt% the hardness of the composite also increases, and it has major significant effect on hardness than CeO_2 in this work.

Table 4.4 Hardness values of fabricated composites

Sample	Chemical Composition	HV_1	HV_2	HV_3	HV Average
S_1	AZ31B/5SiC/ 10CeO_2/4Gr	89.2	89	87.2	88.467
S_2	AZ31B/7.5SiC/ 7.5CeO_2/4Gr	99	94.4	92.7	95.367
S_3	AZ31B/10SiC/ 5CeO_2/4Gr	106.5	111.9	115.2	111.2

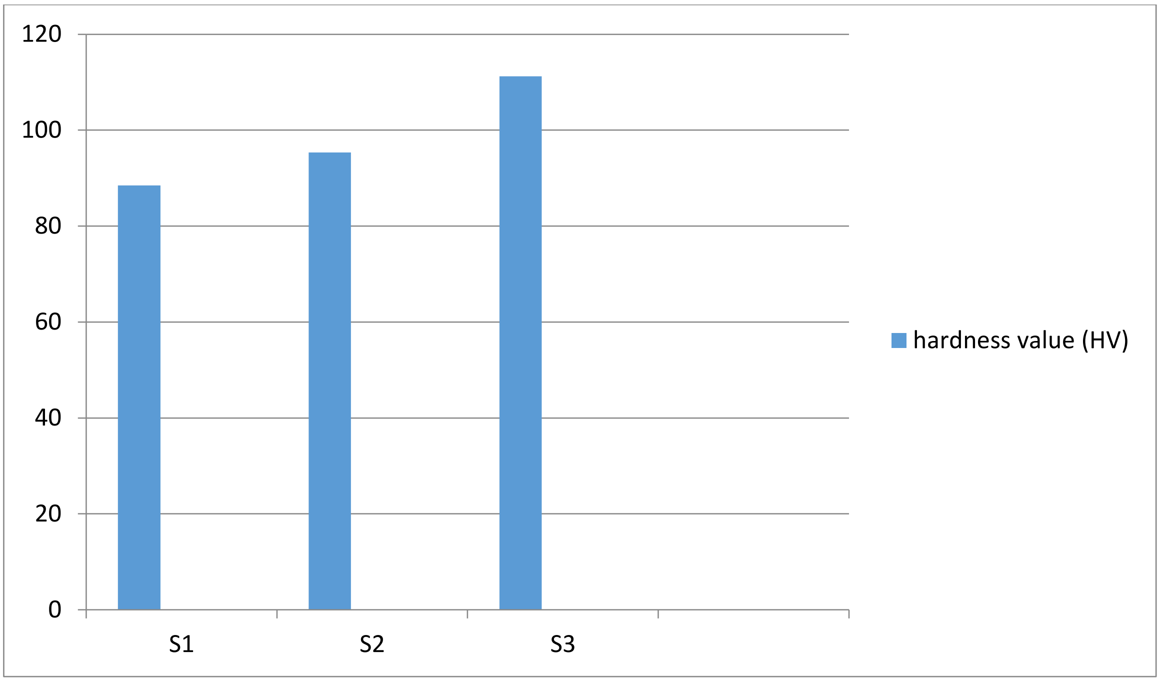

Figure 4.5 Hardness values of AZ31B-SiC-CeO_2-Gr composite

4.2.7 Analysis of compressive test

The universal testing device was used to compress three samples. As shown in Figure 4.6 the ultimate compressive strength (UCS) values of the samples S1, S2 and S3 are 293.6084, 307.4866 and 339.6084 MPa respectively. Sample three have the highest ultimate compressive strength value of 339.6084 MPa which have an increment of 208.7% than the matrix material (AZ31B) having 110MPa ultimate compressive strength. The ultimate compressive strength of the AZ31 matrix material can be increased by adding up to 19% of reinforcement particles. However, sample three, which contains 10% SiC and 5% CeO_2, has the highest ultimate compressive strength. This indicates that increasing the weight percentage of SiC in the sample increases the UCS because the sample has less porosity due to the presence of less CeO_2. Compressive strength increases as the porosity, or void space inside the sample, decreases, allowing the sample to resist fracture.

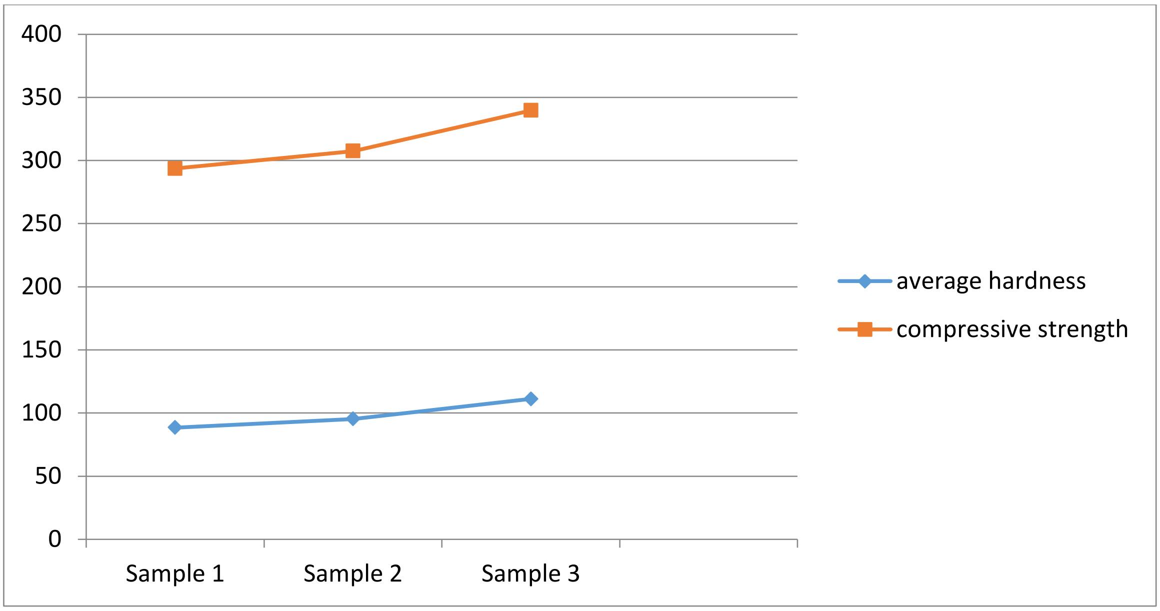

Figure 4.6 Average Vickers Hardness and Compressive Strength

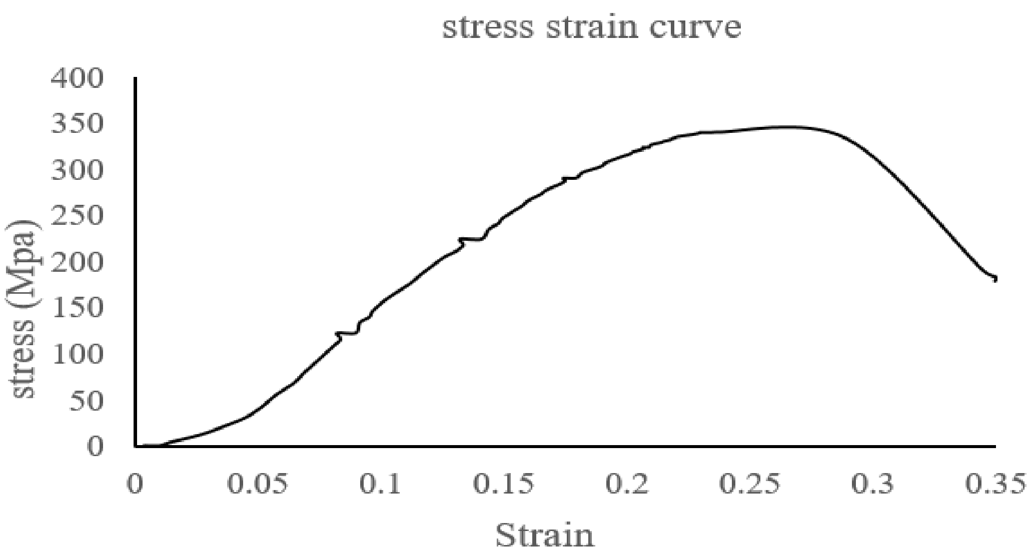

Figure 4.7 stress strain diagram for sample three (AZ31B-5%CeO_2-10%SiC-4%Gr)

4.2.7.1 Compression fractography

SEM is utilized to investigate the fracture mechanisms of the composites at different magnifications. The surface morphology, or fractography, of the samples at 100 µm magnifications is shown in Figure 4.8. It's employed to investigate the fracture mechanism of the composite once a load is applied till failure.

Figure 4.8 clearly illustrate cleavage cracks, implying the presence of brittle fracture in the Mg MMCs. The force applied immediately perpendicular to the sample caused small cracks to begin to spread in multiple places, and the brittleness of the material led to cleavage cracking in some locations, increasing the fracture of composite samples. Simultaneously, micro pores occurred, resulting in a reduction in mechanical properties.

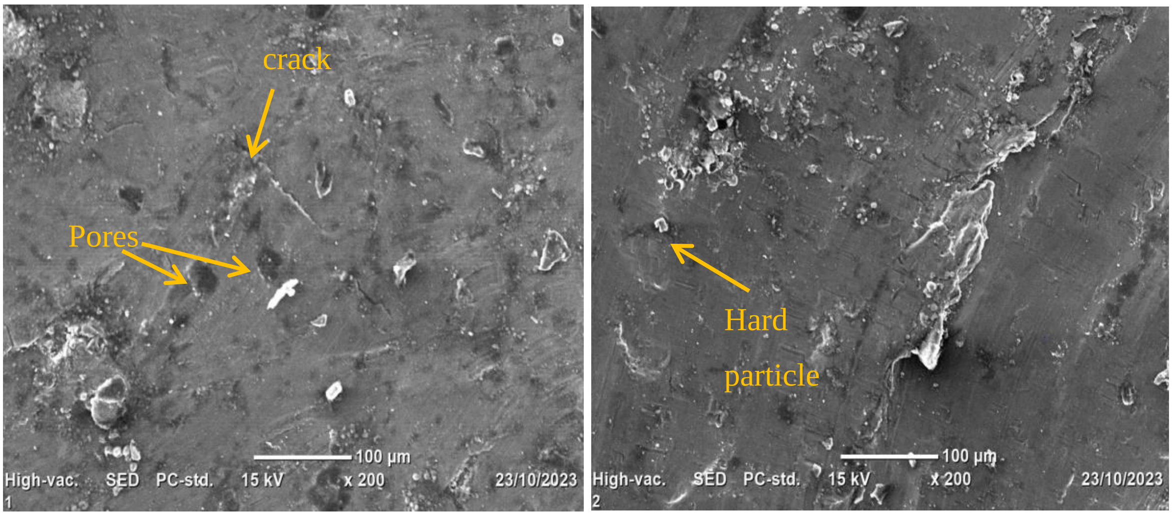

Figure 4.8 Fractography Analysis Using SEM for (S1) and (S2) at 100 μm

4.2.8 Wear test analysis

The samples were tested with 30 N applied loads on a 50 mm dia. at a sliding speed of 400 rpm wear truck for fifteen minutes at room temperature. Using equation (3.12) the following wear rate results are obtained.

Table 4.5 wear rate results of the samples

Sample No.	Weight before wear test (W_b)	Weight after wear test (W_a)	Wear rate (W.R) mg/m
S1	0.53841g	0.4839g	0.0578
S2	0.5281g	0.4707g	0.0609
S3	0.5049g	0.4493g	0.0589

According to the Table 4.5 the wear rate of S1 is the lowest since it have 10 wt% of CeO_2. Addition of CeO_2 has high effect on wear resistance of the base metal (AZ31B) but SiC also have effect on the wear resistance of AZ31B, S3 have a good wear resistance next to S1. Small amount of difference was observed between the wear rate of S1 and S3 which is 0.0011. Graphene also increases the wear resistance of AZ31B because of the solid lubrication effect.

4.2.8.1 Worn surface analysis using SEM

In this work, the wear morphology of Mg MMCs was also investigated after the wear test in the pin-on-disc device. The samples' worn surfaces under a 30 N applied load were examined using a SEM characterization tool. Various wear mechanisms are clearly visible on the worn surface; consistent wear detritus, scratches, delamination, and grooves are visible in connection to sliding directions. Figure 4.9 illustrates the main wear mechanisms that were found in the samples: abrasive wear, fatigue, oxidation, and delamination. The inclusion of SiC and CeO_2 improves wear resistance, as demonstrated by SEM examinations of worn surfaces and wear debris. In addition, wear loss is reduced by the addition of graphene since it guides the uniform dispersion of particles throughout the matrix.

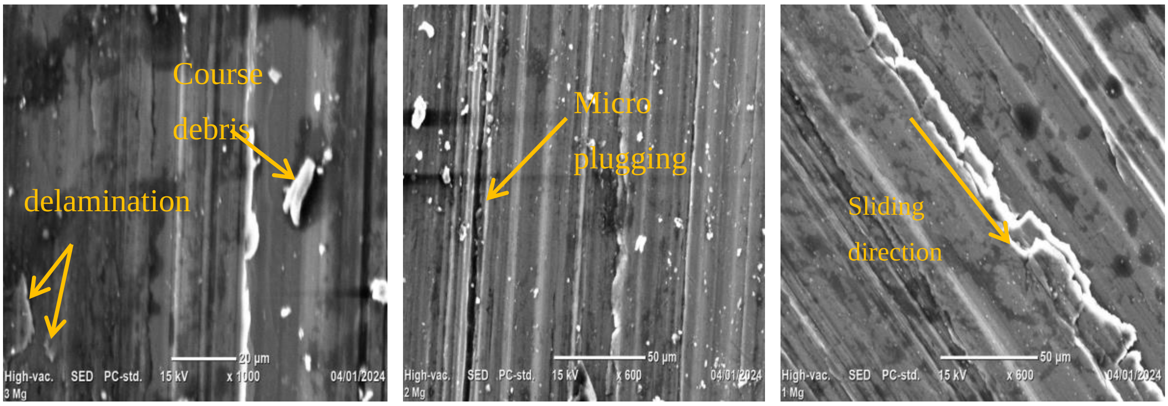

Figure 4.9 Worn surfaces of S1, S2 and S3 at 20 and 50µm using SEM

4.2.9 Corrosion test analysis

Corrosion tests on a range of AZ31B composite materials in a 3 weight percent NaCl solution were carried out in the ASTU material lab using a biological electrochemical cell that had three electrodes attached to a biological device called a potentiostat. 100 mL of distilled water electrolyte was removed for each experiment, and 3% (30g) of NaCl was dissolved to generate a NaCl electrolyte. The electrodes were left in the electrolyte solution for approximately an hour prior to testing, during which time the open circuit potential (OCP) was measured and recorded as indicated in the appendix. Potentiodynamic polarization curves in the -250 to +250 mV range were recorded for OCP at a scan rate of 1 mV/sec. After the sample was immersed in NaCl solution for an hour, the Tafel Plot, also known as the polarization curve (corrosion potential in Y-axis, versus corrosion current in X-axis), and electrochemical impedance spectroscopy (EIS) Nyquist plots (resistance in X-axis versus impedance in Y-axis) were processed and plotted in EC-LAB software. The test was then halted, and the data from each completed test was extracted and plotted using Origin Pro.

4.2.9.1 Measurements of Potentiodynamic Polarization

Potentiodynamic polarization was identified utilizing the Tafel estimation method in order to examine the corrosion behavior of the synthetic materials. The polarization curve's form can be used to calculate the pace at which corrosion reactions occur. An alternative electrochemical method with the advantages of speed and relative simplicity is provided by Tafel plots. The Tafel plot for three samples from the potentiodynamic polarization test was displayed in Figure 4.10 using test data.

The appendix shows how the corrosion potential (Ecorr) and corrosion current density (Icorr) were calculated by projecting the Tafel plot's cathodic and anodic linear segments to the intersection points using the Origin Graphs Analysis Method. The anodic and cathodic slopes of polarization were assessed after Icorr and Ecorr were calculated using the linear fitting dialog box, as shown in the appendix.

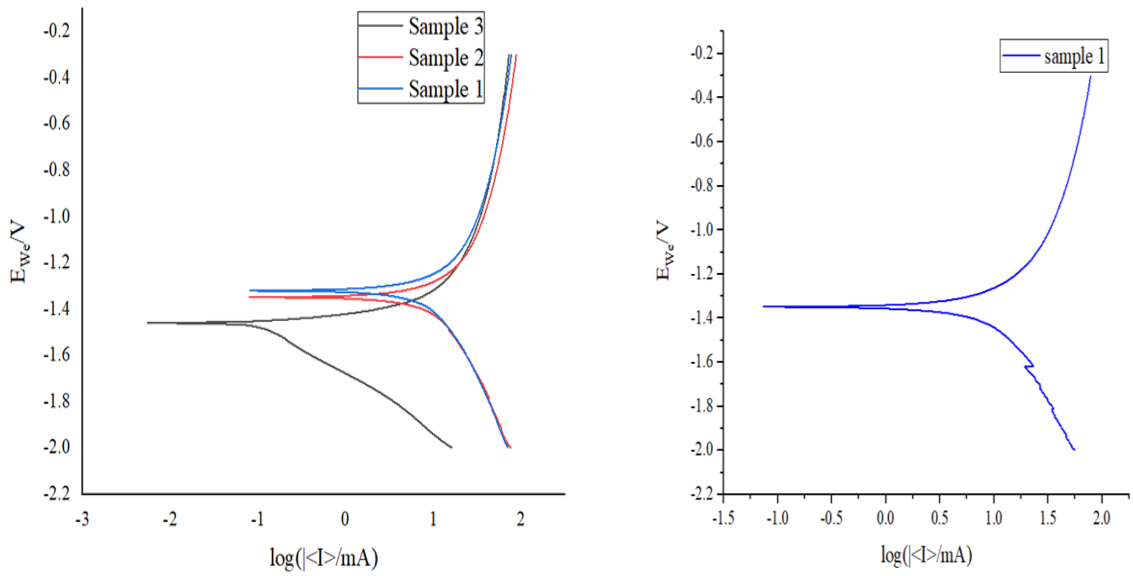

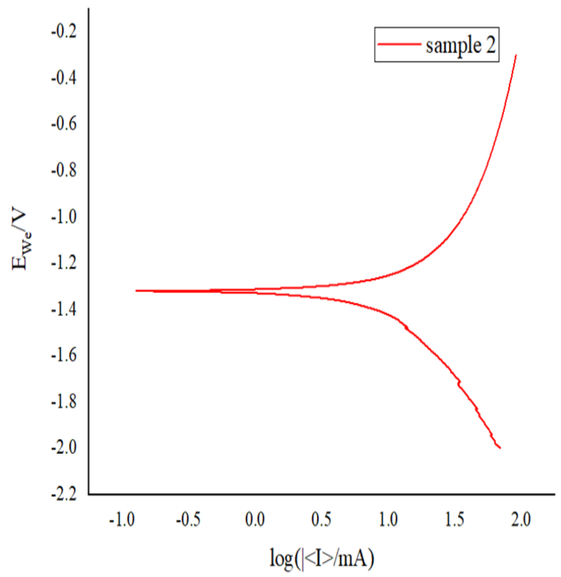

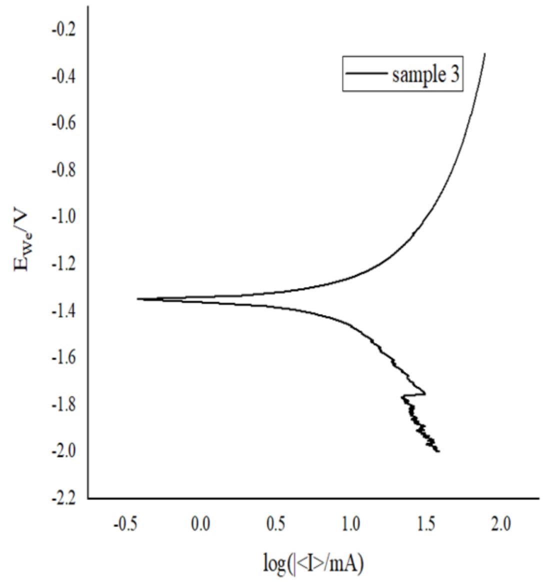

Figure 4.10 Tafel plot of magnesium matrix hybrid composite specimens in 3%NaCl solution

Equation (3.13) listed under corrosion test was utilized to calculate the rate of corrosion and protection effectiveness of manufactured samples. Table 4.6 provides an overview of the Icorr, Ecorr, corrosion rate, anodic and cathodic slopes.

Table 4.6 Tafel Polarization Experimental Parameters Values

Sample No.	E_{corr}(V)	$\boldsymbol{\beta a}$(V)	$\boldsymbol{\beta c}$(V)	I_{corr} ($\boldsymbol{\mu A}_{/mm^2}$)	CR (mm/yr)
S1	1.34728	0.25884	-0.31353	0.691	0.521
S2	1.3169	0.16903	-0.27849	0.6077	0.446
S3	-1.3472	0.20886	-0.2619	0.5872	0.428

According to Figure 4.10 and Table 4.6 by dissolving into the solution, the AZ31B ions in the lattice thin the passive barrier on the metal surface, accelerating corrosion in the base material and the formation of rust on their surfaces. The effect of adding hybrid reinforcement particles to the base metal led the Ecorr to move in a favorable direction and the Icorr to decrease, as shown in Figure 4.10, which was proven by a potentiodynamic polarization test in a 3% NaCl solution. Since CeO_2 and SiC are resistant to severe corrosion attack, their addition may have an impact on the rate of corrosion and the polarization resistance. The corrosion rate of S3 (0.428mm/yr) was lowest than the other two samples. Since the weight percentage of SiC is largely present in sample 3 the CeO_2 also gives the base material to have better wear resistance than the base material and the other samples.

Using the above test results sample three (AZ31B-10SiC-5CeO_2-4Gr) was selected because of having best properties than the other samples for the secondary operation which is machining.

4.3 Simulation result for machining

The cutting tool tip temperature, tool wear rate, and MRR for the experimental process are predicted using a simulation of AZ31B-10SiC-5CeO_2-4Gr. Based on prior research, the DCKNL tool holder was chosen for this investigation, and the parameters of cutting speed, feed rate, and depth of cut were found to have a substantial impact on the machining responses. For the purpose of simulating cutting tool tip temperature, tool wear rate, and MRR during machining, DEFORM 3D was utilized.

Table 4.7 Data required for defining material and assumption made for simulation

No.	Defined parameters	Data/formula	Source of data
1	Compression strength	339.6084MPa	Compression test.
2	Density	1.7188g/cm^3	Archimedes principle and experimental result.
3	Flow stress constitutive equation (power law)	$\bar{\sigma}$ = C$\bar{\varepsilon}^n \dot{\bar{\varepsilon}}^m + y$	Selected to determine flow stress from DEFORM 3D software.
4	constants defined in power law C= constant of material n= exponent of strain m= exponent of strain rate y= value of initial yield k=thermal conductivity C_p=heat capacity e=emissivity	C = 236.968 MPa n = 0.2496 m = 0.46366 y = 183.314 MPa k = 12.5W/mk C_p = 420 J/kgk e = 0.85	Calculated data with Equations listed under input material data based on compression strength of AZ31B-10SiC-5CeO2-4Gr hybrid composite

4.3.1 Result Values Obtained from DEFORM 3D software

For simulation the combination of input parameters were used by using BBD method for response surface methodology. After simulation was done a different value of responses (cutting tool tip temperature, tool wear rate and MRR) have been obtained. The MRR was calculated using the initial and final volume data from DEFORM 3D software.

$$MRR = \frac{\Delta V}{t} = \frac{V_f - V_i}{t} \quad (4.1)$$

Where; V_i *and* V_f are initial and final volumes of the sample before and after the machining (turning) process and t is the time taken to finish one machining (turning) operation.

a

b

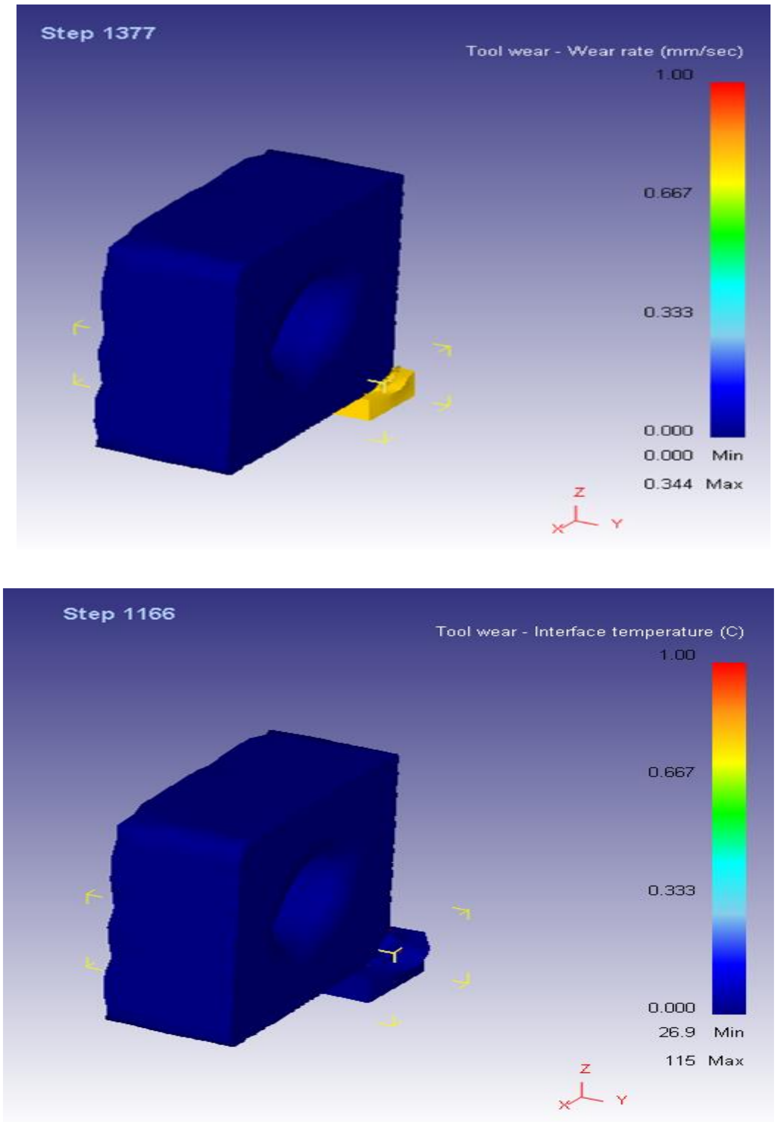

Figure 4.11 a) simulation result for wear rate b) simulation result for tool tip temperature

Table 4.8 MRR, Tool wear rate and Cutting tool tip temperature data obtained from DEFORM 3D software

Cutting Speed (m/min)	feed rate (mm/rev)	Depth of cut (mm)	MRR (cm^3/min)	Tool wear rate (mm/sec)	Cutting tool tip temperature (^{0}C)
80	0.24	0.5	10.25	0.47	85
40	0.24	0.2	2.02	0.16	61.6
40	0.08	0.5	1.7	0.12	52.8
40	0.24	0.8	8.16	0.19	63.89
80	0.4	0.2	6.88	0.57	90
40	0.4	0.5	8.48	0.25	64.2
80	0.24	0.5	10.25	0.47	85
80	0.08	0.2	1.38	0.34	74
120	0.4	0.5	24.48	1.1	123.98
120	0.24	0.2	5.6	0.81	114.2
120	0.08	0.5	4.82	0.74	102.6
80	0.24	0.5	10.25	0.47	85
120	0.24	0.8	23.52	0.89	121.4
80	0.4	0.8	26.08	0.66	97
80	0.08	0.8	5.14	0.38	80.2

4.4 Design Expert 13 software

Statistical work was performed using Design of Expert 13 software. Optimization process using the output data from DEFORM 3D software on Design Expert 13 software was done to identify the optimum paramaters for the actual experimentation on CNC lathe machine. The results from Design Expert 13 software furthermore, predictive and optimization models are discussed with supporting photographs and schematic diagrams.

4.4.1 Material Removal Rate analysis and discussion

4.4.1.1 Statistical Analysis

Fit Overview

Fit Summary is a computer program that provided statistics for comparing the models and evaluated the impacts for each model term. These data included p-values, lack of fit, and R-squared values. This program collected the essential data required to identify the suitable beginning point for both the recommended model and the final model fitting. Table 4.9 indicates that the cubic and quadratic models were aliased and that the 2FI model (sequence sum of squares for the two-factor interaction A, B, C, AB, BC, and AC terms) was advised. Accordingly, the model with the greatest rank is the one that has an insignificant lack of fit (p-value > 0.10), explains a large portion of the response variance (p-value small), and has a reasonably good agreement (within 0.2 of the expected and adjusted R-squared).

Table 4.9 Fit summary for MRR

Source	Sequential p-value	Adjusted R^2	Predicted R^2	
Linear	< 0.0001	0.8161	0.6909	
2FI	**< 0.0001**	**0.9990**	**0.9983**	**Suggested**
Quadratic	0.0822	0.9995	0.9974	
Cubic		1.0000		Aliased

Table 4.10 Sequential Model Sum of Squares

Source	Sum of squares	Df	Mean square	F- value	P- value	
Mean Vs total	1480.27	1	1480.27			
Linear Vs mean	806.97	3	268.99	21.71	< 0.0001	
2FI vs Linear	**135.76**	**3**	**45.25**	**676.50**	**< 0.0001**	**Suggested**
Quadratic vs 2FI	0.3799	3	0.1266	4.08	0.0822	
Cubic vs Quadratic	0.1553	3	0.0518			Aliased
Residual	0.0000	2	0.0000			
Total	2423.53	15	161.57			

Table 4.11 Model Summary Statistics

Source	Std. Dev.	R^2	Adjusted R^2	Predicted R^2	PRESS	
Linear	3.52	0.8555	0.8161	0.6909	291.60	
2FI	**0.2586**	**0.9994**	**0.9990**	**0.9983**	**1.60**	**Suggested**
Quadratic	0.1762	09998	0.9995	0.9974	2.48	
Cubic	0.0000	1.0000	1.0000		*	Aliased

4.4.2 Analysis of Variance for Material Removal Rate

This part contained descriptive statistics and statistical tests that identified key terms in the model determined by low p-values. Based on the analysis of variance for material removal rate Table 4.12, the model F-value of 2348.78 revealed that the model is significant, and there is only a 0.01% possibility that an F-value this large could arise due to noise. A P-value below 0.0500 indicates that the model terms are significant. In this case, A, B, C, AB, AC, and BC were significant model terms. In the event that there is a smaller than 0.2 discrepancy between the adjusted R-squared and anticipated R-squared values in the following table, the model is fitting the data and can be confidently utilized for interpolation. Additionally, the model's Adequate Precision (141.3531) in the table below shows that it has a value greater than 4, the signal is strong enough to be utilized for both optimization and design space navigation. By dividing the total of squares for each individual source by the sum of squares for the Cor Total, the proportion of contribution in this ANOVA was determined.

Table 4.12 Analysis of Material Removal Rate Variance

Source	Sum of squares	Df	Mean square	F-value	P-value		Contribution percentage (%)
Model	942.73	6	157.12	2348.78	< 0.0001	Significant	99.9
A-Cutting speed	181.07	1	181.07	2706.79	< 0.0001		19
B-feed rate	349.54	1	349.54	5225.16	< 0.0001		37
C-depth of cut	276.36	1	276.36	4131.25	< 0.0001		29
AB	41.47	1	41.47	619.98	< 0.0001		4
AC	34.69	1	34.69	518.61	< 0.0001		3
BC	59.60	1	59.60	890.92	< 0.0001		6
Residual	0.5352	8	0.0669				
Cor Total	943.27	14					100

Table 4.13 Fit Statistics

Std. Dev.	0.2586	R^2	0.9994
Mean	9.93	Adjusted R^2	0.9990
C.V. %	2.60	Predicted R^2	0.9983
		Adeq Precision	141.3531

4.4.3 Regression for Material Removal Rate

Regression technique was employed for figuring out the statistical relationship between cutting parameters and Material removal Rate and to make predictions about the response for given levels of each factor.

$MRR = 9.8 – 0.13X_1 – 39.15X_2 – 19.34X_3 + 0.50X_1X_2 + 0.25X_1X_3 + 80.42X_2X_3$ or

$$MRR = 9.8 – 0.13v – 39.15f – 19.34d + 0.50vf + 0.25vd + 80.42fd \quad (4.2)$$

Where; v, f and d are cutting speed, feed rate and depth of cut respectively.

4.4.4 Parametric Impact on the Rate of Material Removal

The residuals follow a normal distribution and, therefore, follow a straight line, according to the graph of the Normal Probability plot vs internally student zed residual on Figure 4.12 (A). In addition, the residuals versus anticipated graph in the following figure (B) illustrates the validity of the model for analyzing how various elements affect the rate of material removal. It plots residuals against ascending predicted response values to test the assumption of constant variance. The plot displays a random scatter or constant range of residuals across the graph.

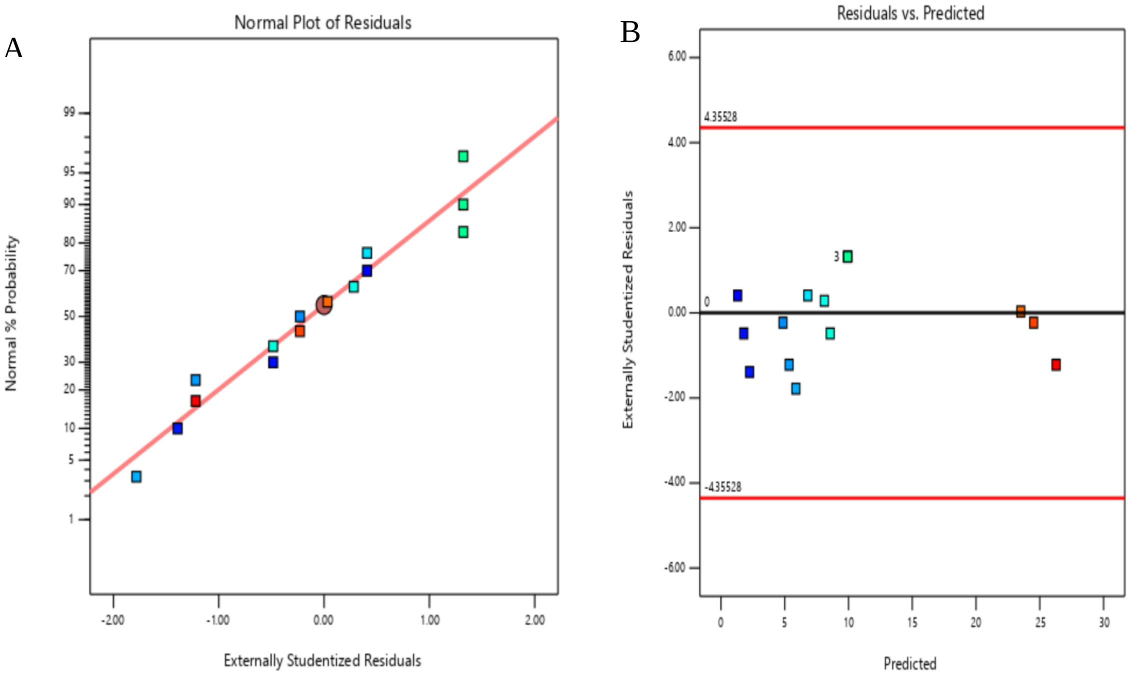

Figure 4.12 (A) normal plot of residuals (B) residuals Vs predicted

4.4.4.1 Effects of cutting speed on MRR

The material removal rate increased as cutting speed increased, as seen in the figure below, with a 19% percentage contribution to the material removal rate. The findings of the simulation showed that a cutting speed that is too slow would cause the machining operation to lose time, which would lead to a poor rate of material removal or production. Figure 4.13 shows the contour plot showing the relationship between feed rate and cutting speed on material removal rate.

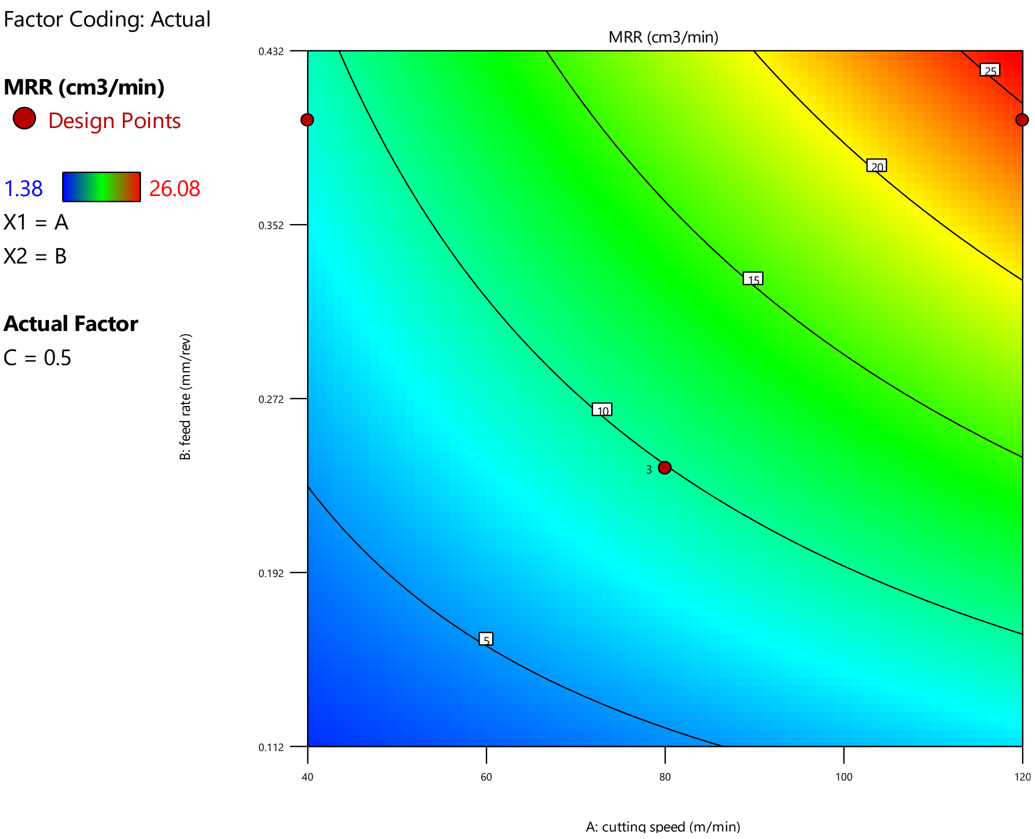

Figure 4.13 Interaction effects of feed rate and cutting speed on MRR

4.4.4.2 Effects of feed rate on MRR

It was found that when feed rate rose, cutting speed and depth of cut remained constant. According to the study and ANOVA, feed rate was a significant factor that contributed 37% of the greatest rate of material removal. Increased feed rates cause more material to come into contact with the cutting tool, increasing the cutting force and quickening the process of material removal. The cutting tool's axial movement is encouraged by higher feed rates, which speeds up its trip to a new location and raises MRR. The contour plot illustrating the interaction between cutting speed and feed rate and material removal rate is presented in Figure 4.14.

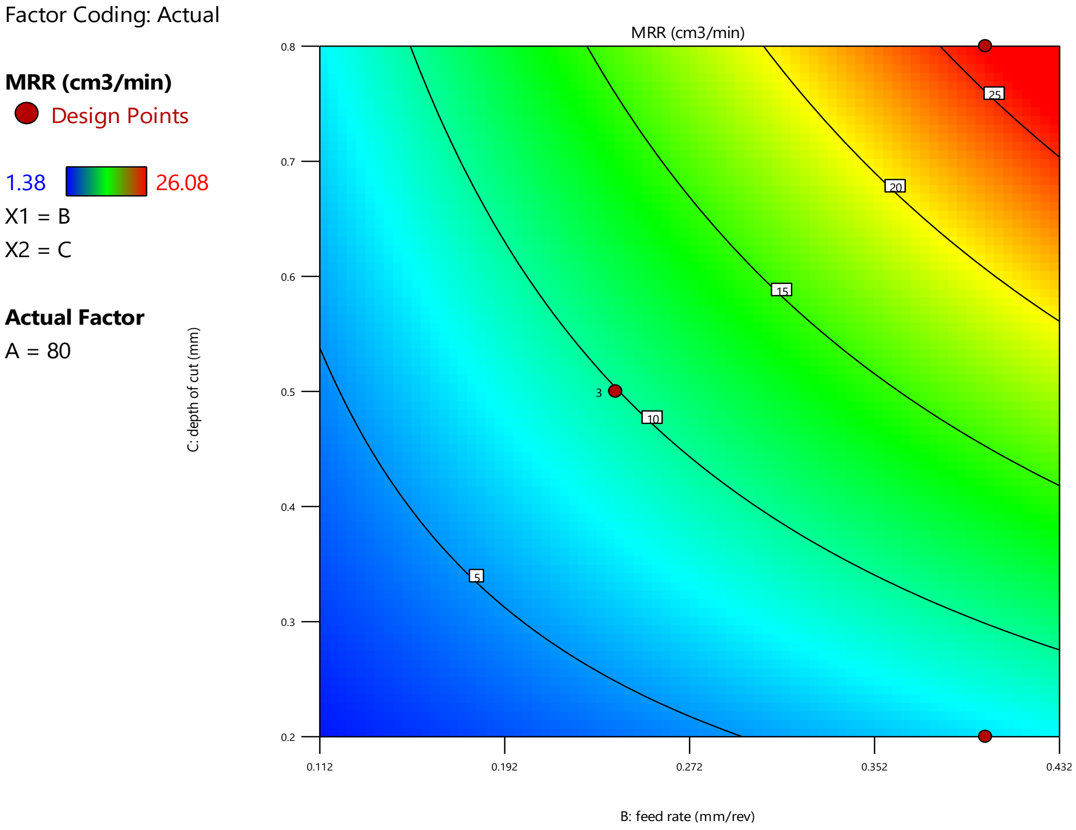

Figure 4.14 Interaction effects of depth of cut and feed rate on MRR

4.4.4.3 Effects of depth of cut on MRR

The rate at which material was removed rose in tandem with depth of cut and cutting speed at a steady feed rate. Furthermore, with a 29% contribution percentage, the ANOVA table indicates that depth of cut is the second important component on material removal rate, after feed rate. Greater volume of material to erode results from deeper cuts, which raises MRR. If the procedure is carried out at a high cutting speed, a greater Material Removal Rate can be attained in high cut turning operations. The contour plot for the interaction between cutting speed and depth of cut on rate of material removal is displayed in Figure 4.15.

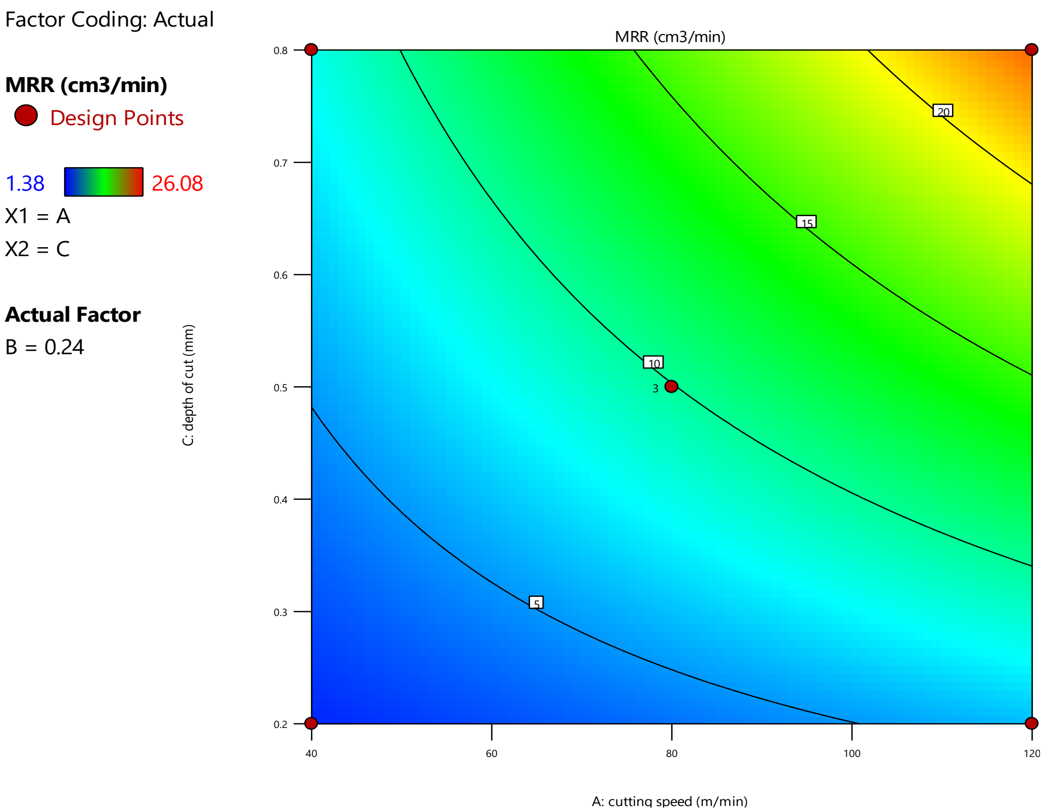

Figure 4.15 Interaction effects of depth of cut and cutting speed on MRR

4.4.5 Analysis of Tool tip Temperature

Interaction between the tool and the chip interfaces caused heat to be produced during machining. Depending on the material being machined and the cutting parameters being employed, different amounts of heat are created. Heat was produced at the tooltip interface as a result of friction forces, as observed and measured throughout the experimental procedure. Using an infrared thermometer, the table under the DEFORM 3D during the AZ31B-SiC-CeO_2-Gr turning process, the program showed the temperature measured at the tooltip for various cutting parameters.

4.4.5.1 Statistical Analysis

Suitable synopsis

Every model term and statistic that is used to compare the models is calculated by fit summary, including p-values, lack of fit and R-squared values. Furthermore, it obtained the essential statistical information needed to suggest a model and choose the proper starting point for the final model fitting. The tables below clearly showed that the cubic model was the aliased model and the quadratic model was the suggested model. Accordingly, the highest order model, the cubic model, explains a considerable portion of the variation in the answer (p-value tiny), has a negligible lack of fit (p-value > 0.10), and the Adjusted R-squared and Predicted R-squared agreed rather well (within 0.2 of each other).

Table 4.14 Fit summary

Source	Sequential p-value	Adjusted R^2	Predicted R^2	
Linear	< 0.0001	0.9805	0.9686	
2FI	0.3855	0.9813	0.9487	
Quadratic	**0.0002**	**0.9993**	**0.9958**	**Suggested**
Cubic		1.0000		Aliased

Table 4.15 Model Summary Statistics

Source	Std. Dev.	R^2	Adjusted R^2	Predicted R^2	PRESS	
Linear	3.06	0.9847	0.9805	0.9686	211.69	
2FI	3.00	0.9893	0.9813	0.9487	345.62	
Quadratic	**0.5926**	**0.9997**	**0.9993**	**0.9958**	**28.09**	**Suggested**
Cubic	0.0000	1.0000	1.0000		*	Aliased

4.4.5.2 Variance Analysis for Tool Tip Temperature

Descriptive statistics and statistical tests were presented in this section. Which substantial terms with low p-values were identified in the model. Model F-value of 2131.54 indicated that the model is significant, and there is only a 0.01% chance that an F-value this large could arise due to noise, according to the Analysis of Variance for Tool tip temperature Table4.16. Model terms are considered significant when P-values are less than 0.0500. Important model terms in this instance are A, B, C, AB, AC, A2, B2, and C2. Based on Table 4.17 if the difference between the predicted and adjusted R^2 values of 0.9958 and 0.9993, which is less than 0.2, then the model is fitting the data and may be used with confidence for interpolation. Furthermore, the model showed a sufficiently strong signal when the Adequate Precision in the following table was greater than 4, namely 147.402, to be utilized for optimization and design space navigation. The proportion of contribution in this ANOVA was calculated by dividing the sum of squares for each individual source by the sum of squares for the Cor Total.

Table 4.16 Variance Analysis for Tool Tip Temperature

Source	Sum of Squares	Df	Mean Square	F-value	p-value		Contribution Percentage (%)
Model	6736.14	9	748.46	2131.54	< 0.0001	Significant	99
A-cutting speed	6032.96	1	6032.96	17181.32	< 0.0001		89
B-feed rate	537.59	1	537.59	1531.01	< 0.0001		7
C-depth of cut	64.35	1	64.35	183.28	< 0.0001		
AB	24.90	1	24.90	70.91	0.0004		
AC	6.03	1	6.03	17.16	0.0090		
BC	0.1600	1	0.1600	0.4557	0.5296		
A^2	31.78	1	31.78	90.50	0.0002		
B^2	15.35	1	15.35	43.71	0.0012		
C^2	20.20	1	20.20	57.52	0.0006		
Residual	1.76	5	0.3511				
Cor Total	6737.90	14					100

Table 4.17 Fit Statistics

Std. Dev.	0.5926	R^2	0.9997
Mean	86.72	Adjusted R^2	0.9993
C.V. %	0.6833	Predicted R^2	0.9958
		Adeq Precision	147.4024

4.4.6 Regression model for Cutting Tool Tip Temperature

A regression model in this subtopic is a statistical model that estimated the relationship between cutting Parameters and cutting tool tip temperature.

CUTTING TOOL TIP TEMPERATURE = $38.78 + 0.25X_1 + 56.19X_2 - 25.72X_3 + 0.39X_1X_2 + 0.102X_1X_3 + 4.167X_2X_3 + 0.0018X_1^2 - 79.64X_2^2 + 25.99X_3^2$ or

$$CUTTING\ TOOL\ TIP\ TEMPERATURE = 38.78 + 0.25v + 56.19f - 25.72d + 0.39vf + 0.102vd + 4.167fd + 0.0018v^2 - 79.64f^2 + 25.99d^2 \quad (4.1)$$

4.4.7 Influence of cutting Parameter on tool tip temperature

Figure 4.16 A's graph of The residuals either fell on a straight line or very close to it, according to the Normal Probability plot vs. Externally Studentized Residual, indicating that the errors are distributed normally. As Figure 4.16 predict a random dispersion or continuous range of residuals across the graph shows that all cutting temperature settings were within a reasonable range. B, This tests the assumption of constant variance by plotting the residuals against the ascending expected response values. Consequently, the model may be applied to study how various parameters influence the temperature reached during rotation.

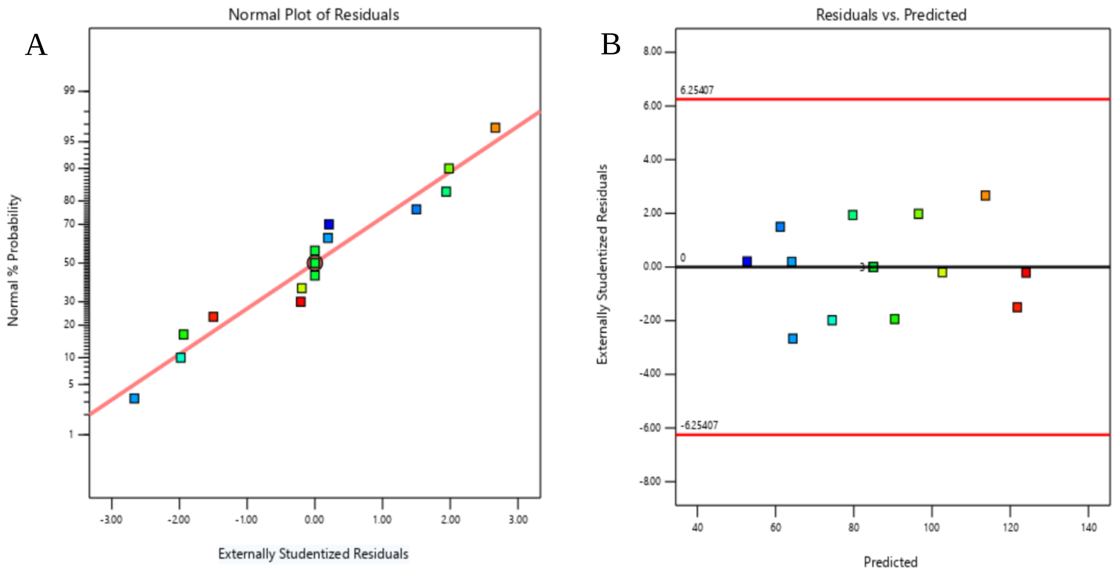

Figure 4.16 (A) Typical residual plot (B) residuals Vs predicted

Table 4.8 shows that the maximum cutting tool tip temperature (123.980) was established at a high feed rate of 0.4 mm/rev, a high cutting depth of 0.5 mm, and a high cutting speed of 120 m/min. With a low cutting speed of 40 m/min, a low feed rate of 0.08 mm/rev, and a cut depth of 0.5 mm, the minimum temperature of 52.80 ^{0}C were achieved. The friction between the materials of the tool and the work piece determines the cutting temperature in the tooltip, which can lead to unfavorable temperatures in the cutting tool and accelerate the wear of the cutting tool materials by softening the tooltip. Through plastic deformation, it hastened the cutting tool's crater and flank wear, which ultimately results in tool breakage. Figure 4.17, where A, B, and C stand for feed rate, depth of cut, and cutting speed, respectively, shows how cutting factors affect temperature.

4.4.7.1 Effect of cutting parameters on cutting tool tip temperature

Figure 4.17 presents the perturbation plot and shows the following: With a percentage of 89%, cutting speed is a significant parameter that affects tool tip temperature. This means that, for the same feed rate and depth of cut, a significant amount of temperature change is observed when cutting speed is changed. (i) The cutting temperature increases significantly with an increase in cutting speed (A). Temperature rises have produced comparable results. This occurred as a result of excessive friction at the tool-work interface and a lack of time for the heat created to be dispersed. (ii) According to the Table 4.16, the cutting temperature contributes 7% to the change in temperature when the feed rate (B) increases for the same reason that the cutting speed increases—that is, friction created at the tool-work interface. (iii) There is no reasonable increase in the cutting temperature when the depth of cut increases. Furthermore, raising the feed rate and cutting speed together often affects the cutting tool temperature more than raising the depth of cut.

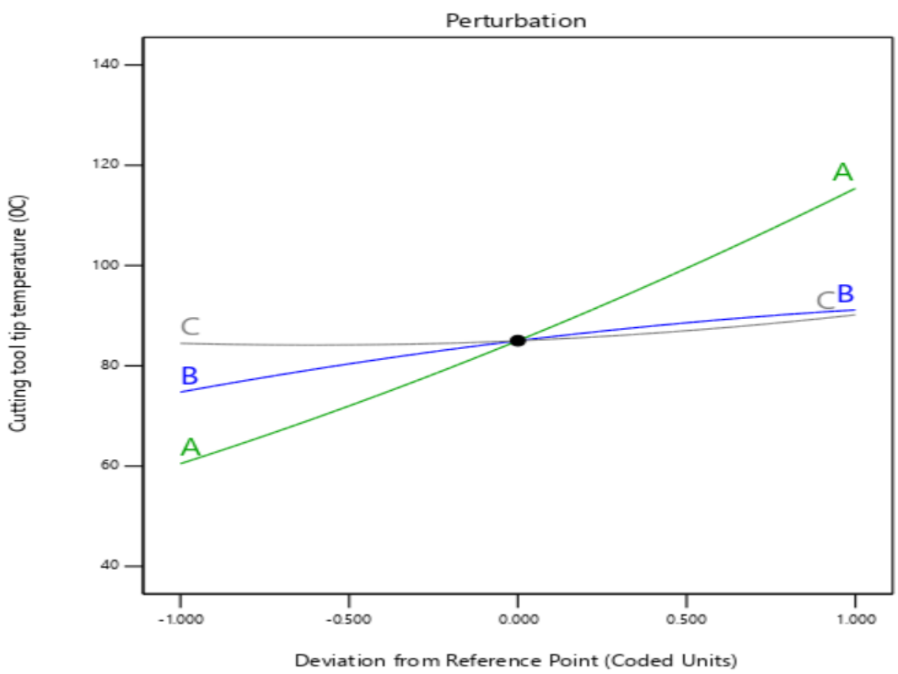

Figure 4.17 Effect of cutting parameters on temperature

The primary impacts of changing the two parameters, cutting speed (A) and feed rate (B), on cutting temperature are shown in the Figure 4.17, with a constant cut depth of 0.5 mm. Lower feed rates and cutting speeds result in lower cutting temperatures (T), as this chart illustrates. As well as Figure 4.17 (b) shows the effect of changing the two parameters, cutting speed (A) and depth of cut (C), on cutting temperature while maintaining a constant feed rate of 0.24 mm/rev. Figure 4.17 shows that, even if the depth of cut changes very little in terms of temperature change, reduced cutting depth and speed result in lower cutting temperatures. Figure 4.17 (c) illustrates the main effects of varying the two variables, feed rate (B) and cutting speed (C), on cutting temperature, where the cutting speed is held constant at 80 m/min. The contour plot of (a) feed rate and cutting speed interactions with tool tip temperature, (b) depth of cut and cutting speed interactions with tool tip temperature, and (c) depth of cut and feed rate interactions with tool tip temperature is displayed in Figure 4.18.

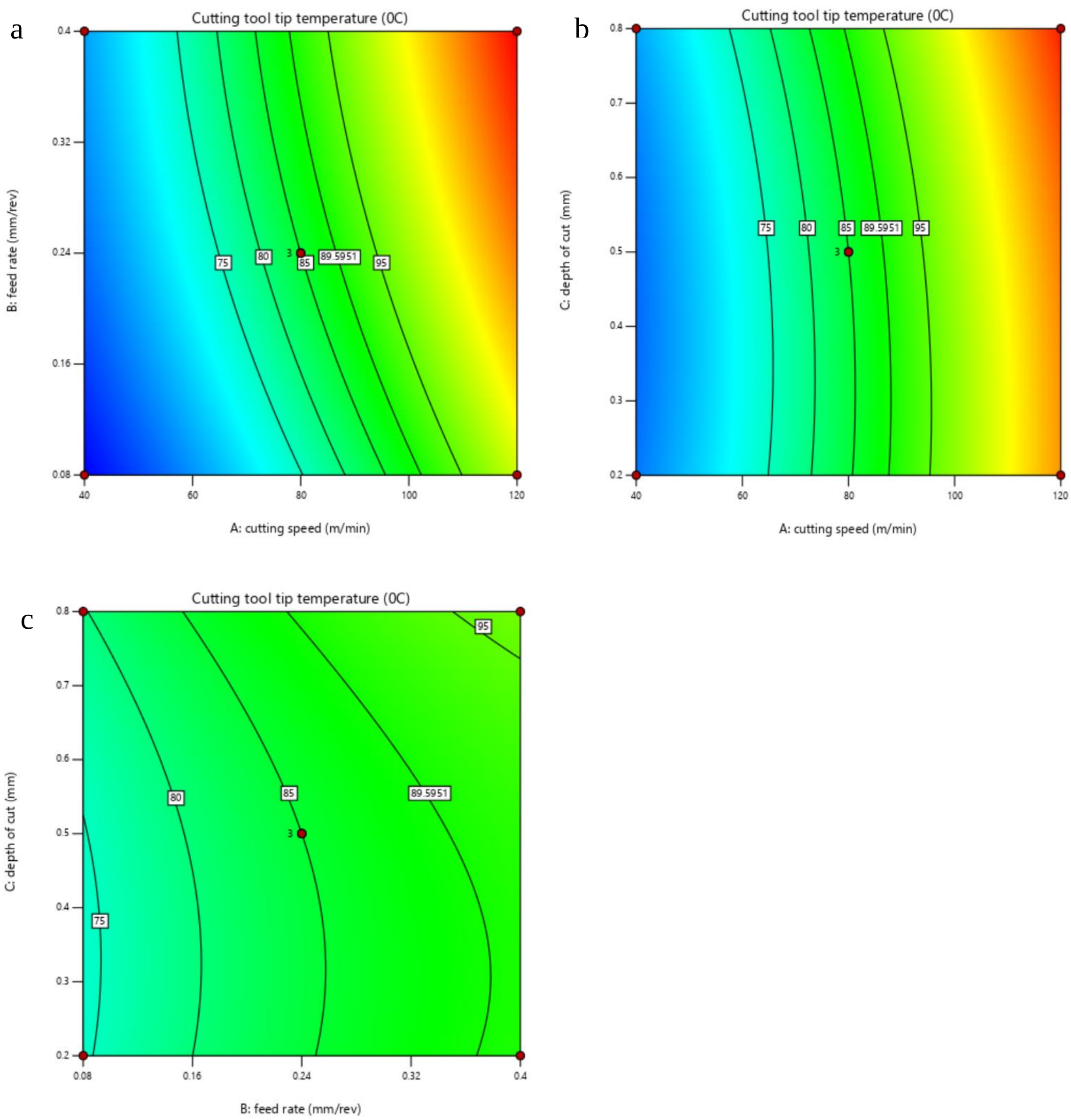

Figure 4.18 Interaction effects of cutting parameters on tool tip temperature

4.4.8 Statistical analysis of tool wear rate

According to tool wear data obtained from DEFORM 3D software, statistical data from design expert is reported here.

Fit Summary

Fit Summary assisted with the initial regression computation to fit all polynomial models for the chosen output answer. The application generated statistics for comparing the models, including R-squared values, p-values, and lack of fit, and it computed the impacts for each model term. Important data were obtained with this tool, which was then used to identify the best place to start when fitting the final model and making recommendations for the model. It was clear from the following tables the response's fluctuation is much more explained by the highest order model, the cubic model (p-value tiny). It also exhibits a negligible inability to fit (p-value > 0.10), as well as the predicted and adjusted R-squared match rather well (within 0.2 of one another). The model that is recommended is the quadratic model.

Table 4.18 Fit Summary

Source	Sequential p-value	Adjusted R^2	Predicted R^2	
Linear	< 0.0001	0.9666	0.9475	
2FI	0.1407	0.9759	0.9424	
Quadratic	**0.0096**	**0.9954**	**0.9737**	**Suggested**
Cubic		1.0000		Aliased

Table 4.19 Sequential Model Sum of Squares

Source	Sum of Squares	Df	Mean Square	F-value	p-value	
Mean vs Total	3.87	1	3.87			
Linear vs Mean	1.13	3	0.3754	135.89	< 0.0001	
2FI vs Linear	0.0145	3	0.0048	2.43	0.1407	
Quadratic vs 2FI	**0.0140**	**3**	**0.0047**	**12.29**	**0.0096**	**Suggested**
Cubic vs Quadratic	0.0019	3	0.0006			Aliased
Residual	0.0000	2	0.0000			
Total	5.03	15	0.3352			

4.4.8.1 Analysis of Variance for tool wear rate

Descriptive statistics and statistical tests were presented using ANOVA to ensure the model's appropriateness. P-values in the analysis of variance revealed significant terms in the model. The model's F-value of 337.64 indicated that it is significant, and there is only a 0.01% chance that an F-value this large could occur owing to noise, according to the analysis of variance for wear rate in Table 4.20. P-value for the model is smaller than 0.05, indicating the model terms' relevance. A, B, C, A^2, AB and B^2 are important model terms in this instance. The predicted R^2 of 0.9737 and the adjusted R^2 of 0.9954 are reasonably in agreement, as can be seen from Table 4.21; that is, the difference is less than 0.2. Furthermore, Adeq Precision measured the signal to noise ratio, or 60.001, and found that it was greater than 4, indicating that the model is desirable and was utilized to navigate the design space since its signal is strong enough for optimization. The proportion of contribution in the ANOVA was obtained by dividing the sum of squares for each individual source by the sum of squares for the Cor Total.

Table 4.20 Tool wear rate analysis of variance

Source	Sum of Squares	Df	Mean Square	F-value	p-value		Composition percentage
Model	1.15	9	0.1283	337.64	< 0.0001	Significant	99
A-cutting speed	0.9940	1	0.9940	2615.92	< 0.0001		85
B-feed rate	0.1250	1	0.1250	328.95	< 0.0001		10
C-depth of cut	0.0072	1	0.0072	18.95	0.0073		
AB	0.0132	1	0.0132	34.80	0.0020		1
AC	0.0006	1	0.0006	1.64	0.2559		
BC	0.0006	1	0.0006	1.64	0.2559		
A^2	0.0107	1	0.0107	28.07	0.0032		
B^2	0.0031	1	0.0031	8.03	0.0365		
C^2	0.0005	1	0.0005	1.23	0.3179		
Residual	0.0019	5	0.0004				
Cor Total	1.16	14					100

Table 4.21 Fit Statistics

Std. Dev.	0.0195	R^2	0.9984
Mean	0.5080	Adjusted R^2	0.9954
C.V. %	3.84	Predicted R^2	0.9737
		Adeq Precision	60.0008

4.4.9 Regression model for Tool Wear Rate

A regression model is a statistical model that estimated the relationship between cutting Parameters and tool wear rate.

TOOL WEAR RATE = $0.021 + 0.00076X_1 - 0.61X_2 + 0.079X_3 + 0.0089X_1X_2 + 0.001X_1X_3 + 0.26X_2X_3 + 0.000034X_1^2 + 1.12X_2^2 - 0.125X_3^2$ or

$$TOOL\ WEAR\ RATE = 0.021 + 0.00076v - 0.61f + 0.079d + 0.0089vf + 0.001vd + 0.26fd + 0.000034v^2 + 1.12f^2 - 0.125d^2 \quad (4.2)$$

4.4.10 Influence of cutting Parameter on tool wear rate

Figure 4.19 (a) shows the relationship between the externally studentized residual and the normal probability plot. It indicates that the errors are normally distributed because the residuals either fall on a straight line or extremely near to it. Further testing the assumption of constant variance was done on the Residuals vs. Predicted graph (see Figure 4.19, B). There is no need for transformation because the plot showed a random dispersion or continuous range of residuals across the graph, proving that all cutting parameter values fall within a reasonable range. In order to investigate the impact of certain elements on wear rate as determined by the DEFORM 3D program, the model is employed because it is valid.

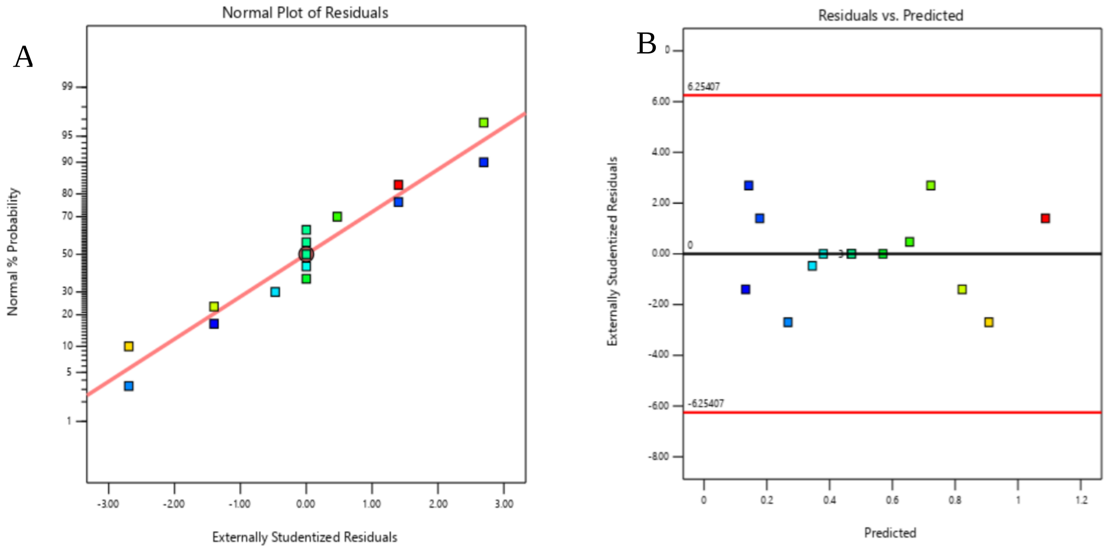

Figure 4.19 (A) Normal residuals plot and (B) Remaining versus Projected

Table 4.8 indicates that the maximum wear rate (1.1) was observed at 120 m/min high cutting speeds, 0.4 mm/rev high feed rates, and 0.5 mm high cut depths. A minimum speed of cutting of 40 meters per minute, a minimum rate of feed of 0.08 millimeters per rev, and cut depth of 0.5 millimeters were achieved to yield the minimal wear rate of (0.12). A study found that a high tool-work interface, high mechanical stress, high thermal stress, and ultimately a poor surface quality all contributed to an increased wear rate.

Figure 4.20 display and contrast the impact of every machining parameter on wear rate through the creation of a perturbation plot. Additionally, the Table 4.20 demonstrates that cutting speed is a key element that influences tool wear rate, accounting for 85% of the variation in wear rate observed for a given feed rate and depth of cut. According to the Table 4.20, the cutting temperature rises in tandem with an increase in feed rate (B). Its percentage contribution to wear rate is 10%, and an increase in cut depth does not rationally cause the wear rate to rise. Furthermore, compared to increasing the depth of cut, increasing the cutting speed and feed rate together often has a greater impact on the tool wear rate. The surface roughness analysis indicates that the primary determinant of surface roughness is feed rate. Specifically, an increase in feed rate causes a corresponding increase in surface roughness, resulting in a poorly machined surface. Additionally, an increase in feed indicates increased chip straining, which in turn promotes higher cutting forces and temperatures. The material becomes softer and easier to adhere to the machined surface because of the elevated temperature, which also raises the average surface roughness and tool wear. Research has also shown that a blunted cutting edge due to tool wear improves surface uniformity while also raising surface roughness. The effect of cutting parameters on wear rate is depicted in Figure 4.20, where A, B, and C stand for, respectively, cutting speed, feed rate, and cut depth.

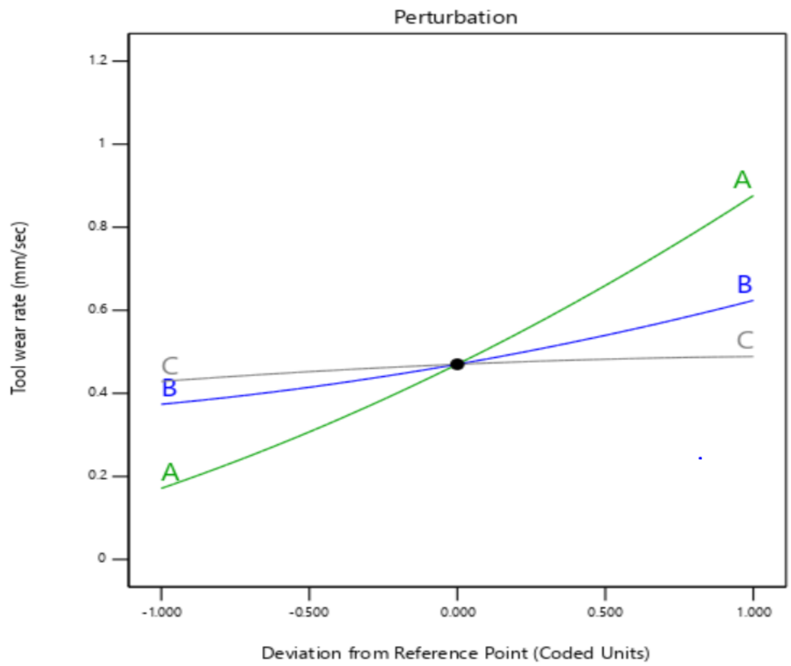

Figure 4.20 Effect of cutting parameters on wear rate

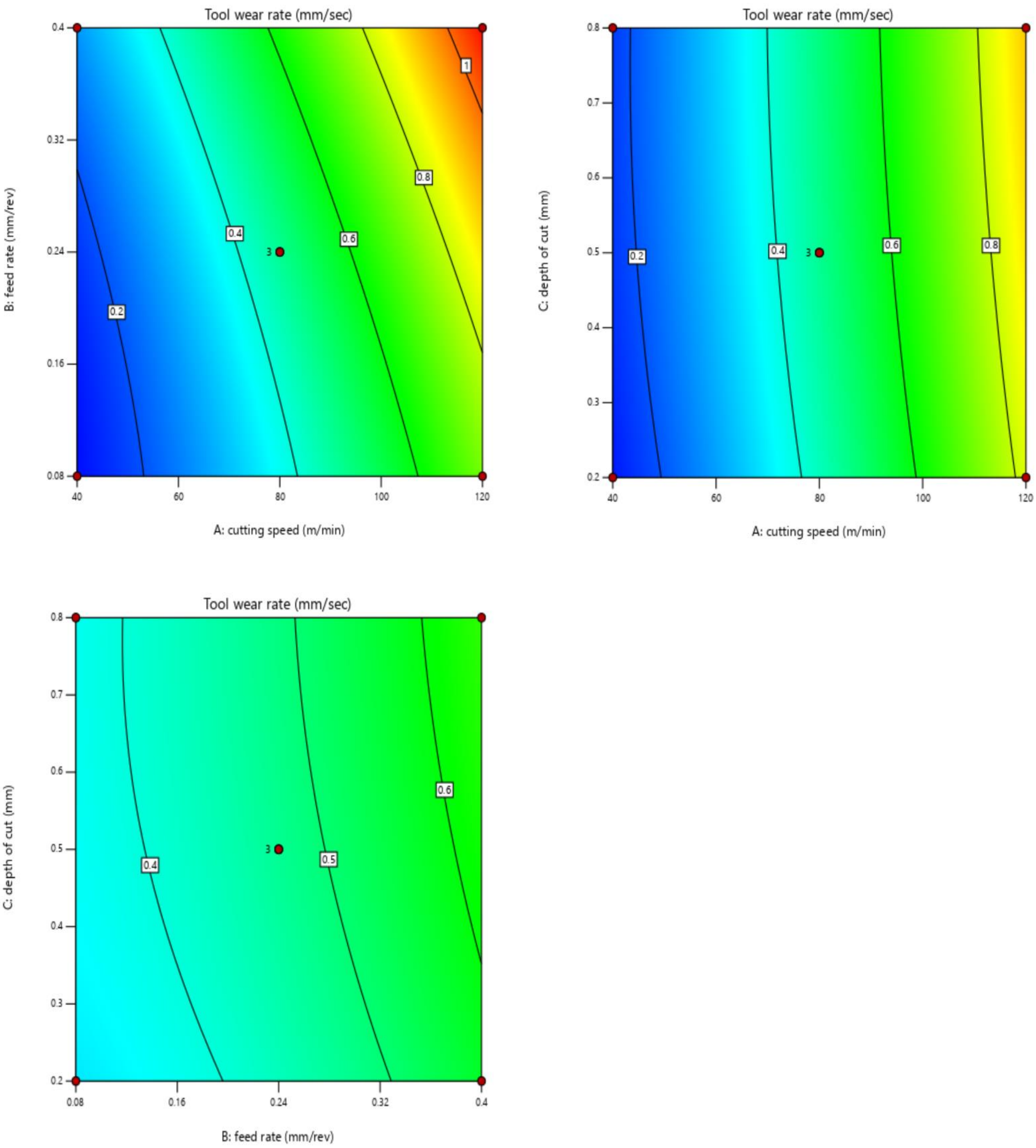

Figure 4.21 Effect of cutting parameters on wear rate

4.5 Multi objective optimization by using Genetic Algorithm

Fitness function must be solved using genetic algorithms in order to use the GA gamultiobj function tool, which stands for Multi-objective Genetic Algorithm Solver, to solve this optimization problem. To be optimized is the multi-objective (vector) function known as the fitness function. Regression and ANOVA models, created with Design Expert software, are the mathematical models used in this work to determine the relationship between input and outcome. The created mathematical model was transformed into a function for MATLAB R2018a. This function was entered as the objective function in the gamultiobj Toolbox of MATLAB R2018a. Three variables were used, and upper and lower boundaries were defined based on the machining parameter values. In the dry turning of AZ31B-10SiC-5CeO_2-4Gr, the objective function values are obtained for the following: maximizing of material removal rate, minimization of tool wear rate, and cutting tool tip temperature. The fitness function's input type was specified using a double vector population type, with 50 being the number of individuals in each generation. A random starting population that complies with boundaries was created using the feasible population. For this optimization tool, a cross-over fraction of 0.8 was used, implying the fraction of the next generation that crosses over produces and in migration, which determines the movement of individuals between subpopulations. A migration fraction of 0.2 and a Pareto fraction of 0.35 were also used. The solutions were ranked and sorted based on the algorithm. Table 4.22 report the Pareto-optimal solutions.

Table 4.22 Pareto Optimal Solution

S. No	MRR (cm^3/min)	Tool wear rate (mm/sec)	Tool tip temperature (^{0}C)	Speed of cut (m/min)	Rate of feed (mm/rev)	Cut depth (mm)
1	-2.685	2.704	88.736	40	0.4	0.2
2	9.499	-0.216	100.311	119.13	0.381	0.201
3	0.61	0.785	42.889	40.029	0.082	0.223
4	5.857	0.061	135.571	119.647	0.225	0.2
5	0.264	0.834	58.36	40.467	0.109	0.202
6	0.249	1.507	104.741	40.146	0.242	0.2
7	15.313	0.005	84.01	118.213	0.397	0.373
8	2.464	0.368	72..925	85.458	0.088	0.212
9	-0.578	2.955	87.73	40	0.4	0.265
10	-1.441	2.321	101.113	40.097	0.355	0.202
11	13.702	0.052	94.021	113.594	0.378	0.331
12	3.579	0.285	123.63	115.472	0.157	0.2
13	3.768	0.593	69.52	59.466	0.112	0.254
14	0.938	0.716	51.036	44.81	0.092	0.214
15	1.286	0.65	46.871	47.813	0.083	0.221
16	-2.468	2.644	90.791	40.122	0.394	0.2
17	17.523	0.13	81.784	118.399	0.39	0.535
18	17.711	0.189	75.313	117.984	0.4	0.573

The creation of the Front Pareto-optimal, which contains the final a group of solutions, is depicted in Figure 4.22. The continuous nature of the modeled optimization issue determines the shape of the Pareto optimum front. It is evident from the data in Table 4.22 that there are 18 pareto-optimal solutions. Surface quality declines as Material Removal Rate rises due to the contradictory nature of the performance criteria, and the resulting solutions exhibit the same tendency. Any one of the Pareto optimal set's options is a workable solution because none of them are superior to the others. The requirements of the process engineer determine which option is preferred above the others. It should be mentioned that every solution is equally good and that, depending on the needs of the manufacturer, any combination of input parameters can be used to obtain the correct response values. The average Pareto spread, which depicts the change in an individual's distance measure from the preceding generation, is shown in Figure 4.23.

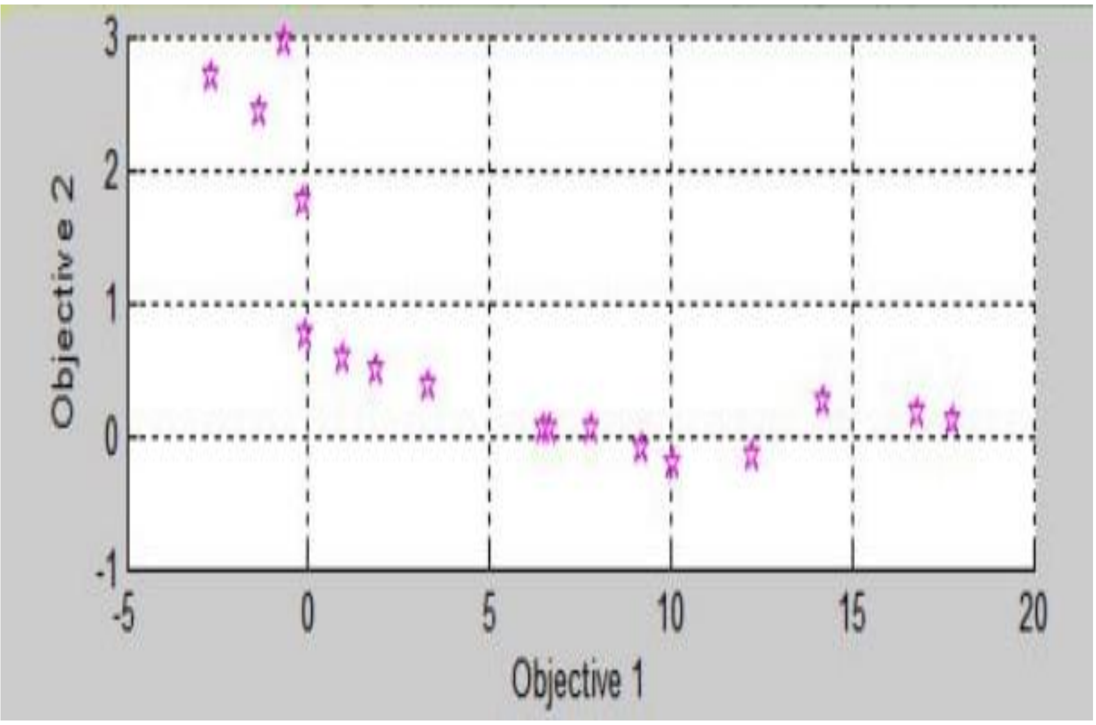

Figure 4.22 Pareto Optimal Front

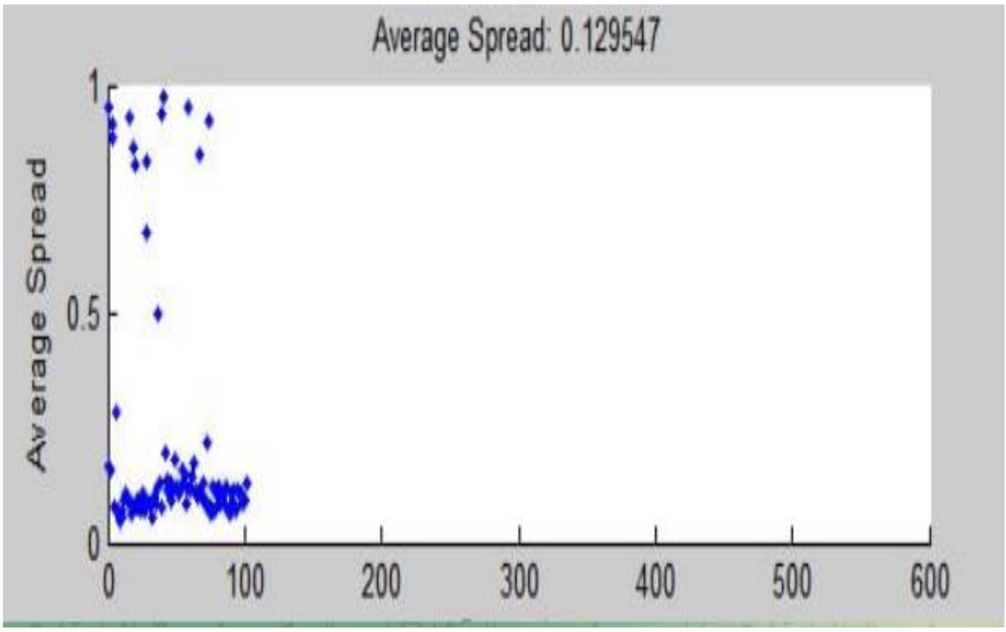

Figure 4.23 Average Pareto spread

4.6 Multi objective optimization by using desirability function

The desire function approach was applied to reduce the temperature of the cutting tool tip, enhance the rate of material removal, lower the rate of wear, and determine the ideal cutting settings for multiple responses. The multi-objective optimization report consisted of the table, the optimal solutions table, and the attractiveness bar graph for the process. The restrictions on multi-objective optimization are shown in Table 4.23. Furthermore, all of the factors used to determine the ideal settings are compiled in Table 4.23. In terms of input factors, range was the ideal configuration. Material removal rate value was analyzed using the larger-is-better desirability function; tool tip temperature and tool wear variables were analyzed using the smaller-is-better desire function. The attractiveness bar graph for every optimal option is displayed in Figure 4.24. The first three bars display the factor settings, while the final four bars display the ideal predicted response values. A graphical representation of the desired individual response for cutting tool tip temperature (78.2%), material removal rate (56.6%), and tool wear (83%), was given by the desirability bar graph. The total replies had a 71.6% desirability rating. The finest possibilities are those with attractiveness values close to 1, as there were 31 desirable results in all. Any of options 1, 2, or 3 may be chosen in this situation. Additionally, this choice was expected to yield the greatest material removal rate and the lowest feasible combined values of tool tip temperature and tool wear. The optimal combination of cutting parameters was 40 m/min for cutting speed, 0.4 mm/rev for feed rate, and 0.8 mm for cut depth.

Table 4.23 Constraints for optimization of cutting parameters and responses

Name	Goal	Lower Limit	Upper Limit	Lower Weight	Upper Weight	Importance
A:cutting speed	is in range	40	120	1	1	3
B:feed rate	is in range	0.08	0.4	1	1	3
C:depth of cut	is in range	0.2	0.8	1	1	3
MRR	Maximize	1.38	26.08	1	1	3
Tool wear rate	Minimize	0.12	1.1	1	1	3
Cutting tool tip temperature	Minimize	52.8	123.98	1	1	3

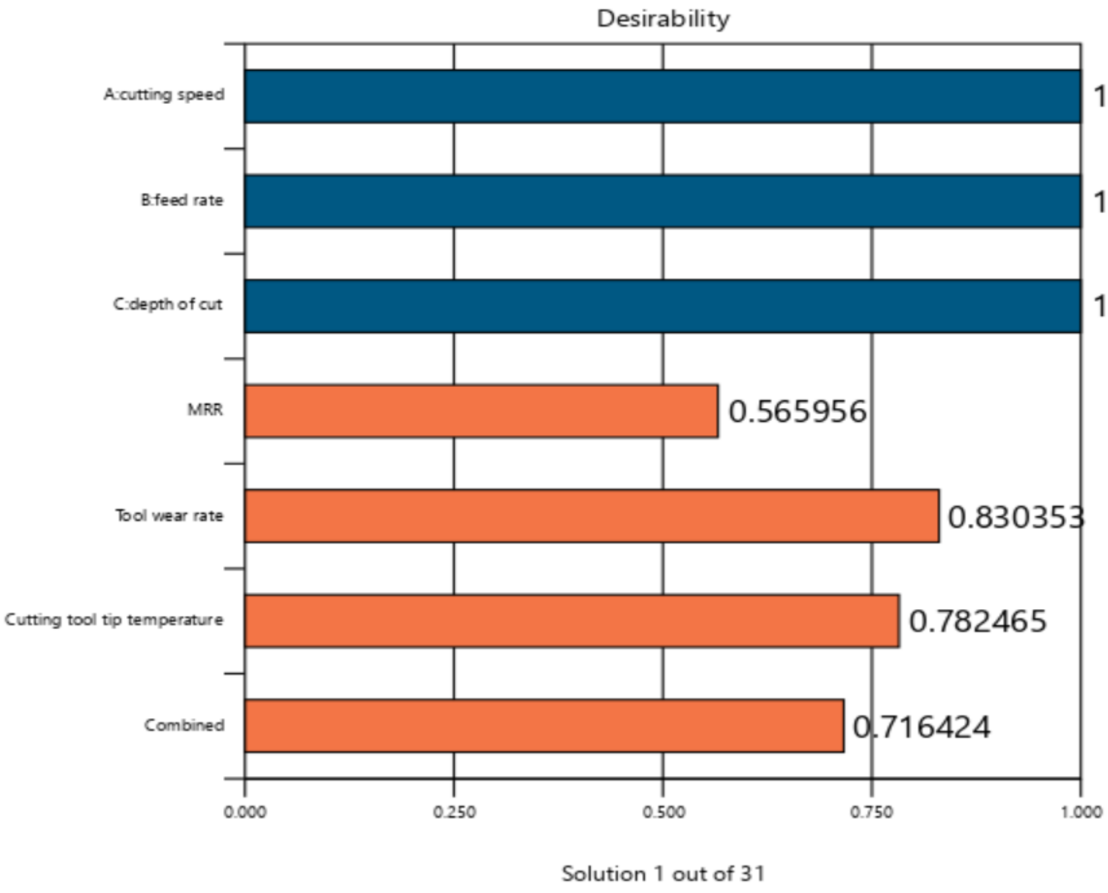

Figure 4.24 Desirability bar Graph

Table 4.24 Solution of optimized cutting parameters for work material

Number	cutting speed	feed rate	depth of cut	MRR	Tool wear rate	Cutting tool tip temperature	Desirability	
1	**40.001**	**0.400**	**0.800**	**15.359**	**0.286**	**68.284**	**0.716**	**Selected**
2	40.295	0.400	0.800	15.439	0.289	68.471	0.716	
3	41.312	0.400	0.800	15.717	0.297	69.117	0.716	
4	40.020	0.400	0.798	15.310	0.286	68.245	0.716	
5	40.393	0.399	0.800	15.408	0.288	68.518	0.716	
6	40.000	0.398	0.800	15.280	0.285	68.260	0.716	
7	42.054	0.400	0.800	15.919	0.303	69.591	0.715	
8	42.558	0.400	0.800	16.057	0.307	69.915	0.715	
9	40.001	0.400	0.795	15.240	0.286	68.171	0.715	
10	43.047	0.400	0.800	16.191	0.311	70.229	0.715	
11	40.000	0.396	0.800	15.169	0.283	68.235	0.714	
12	42.276	0.397	0.800	15.861	0.302	69.702	0.714	
13	40.000	0.400	0.790	15.130	0.286	68.068	0.713	
14	40.000	0.394	0.800	15.066	0.281	68.207	0.713	
15	42.444	0.396	0.800	15.844	0.302	69.792	0.713	
16	44.281	0.400	0.800	16.528	0.321	71.027	0.713	
17	40.002	0.400	0.783	14.966	0.286	67.917	0.711	
18	40.000	0.389	0.800	14.880	0.277	68.154	0.711	
19	42.072	0.400	0.784	15.563	0.302	69.268	0.711	
20	40.000	0.388	0.800	14.822	0.276	68.137	0.711	
21	46.565	0.400	0.800	17.152	0.339	72.518	0.710	
22	45.986	0.400	0.796	16.904	0.334	72.056	0.710	
23	40.011	0.387	0.800	14.769	0.275	68.128	0.710	
24	40.000	0.385	0.800	14.689	0.274	68.098	0.709	
25	47.765	0.400	0.800	17.479	0.349	73.309	0.708	
26	48.538	0.400	0.800	17.690	0.356	73.821	0.707	
27	40.001	0.379	0.800	14.424	0.269	68.015	0.706	
28	47.473	0.390	0.800	16.913	0.338	72.966	0.705	
29	40.000	0.386	0.768	14.025	0.273	67.442	0.700	

30	42.956	0.400	0.741	14.786	0.308	68.966	0.697
31	48.689	0.339	0.800	14.708	0.304	72.726	0.681

4.7 Dry Turning on CNC Lathe Machine

The initial diameter of the cylindrical bar is 20 mm and 50 mm in length before machining (turning). The turning process takes place in +y direction by 30 mm length. In order to validate the response prediction, three runs were selected at random from Multi-objective optimization, where the response parameters MRR was greatest, tool wear rate was minimal, and cutting tool tip temperature was likewise minimum. The desirability function with the maximum desirability was also chosen. Measurements were made for each of the final replies both during and after the machining process.

Figure 4.25 Workpiece after machining

From Table 4.25 the third row parameter combination gave the best surface roughness value which is 0.78 μm. Therefore, when cutting at a speed of 40.029 m/min, feed rate of 0.082 mm/rev, and depth of cut of 0.223 mm are employed, the surface roughness of the AZ31B-10SiC-5CeO_2-4Gr composite yields the best surface quality.

Table 4.25 Experimental values of output parameters with its parameter combination

Optimum Parameters				Experimental value	
Speed of cut (m/min)	Rate of feed (mm/rev)	Cut depth (mm)	MRR (cm^3/min)	Cutting tool tip temperature (^0C)	Surface roughness Ra (μm)
117.984	0.4	0.573	16.642	76.45	0.92
118.231	0.397	0.373	14.278	85.44	0.85
40.029	0.082	0.223	0.56	44.804	0.78
40.001	0.4	0.8	14.347	70.267	1.72

4.8 Analysis of tool wear

Cement carbide with an aluminum oxide coating was the cutting tool insert utilized in the experiments. Two types of wear were found during the dry turning of AZ31B-10SiC-5CeO_2-4Gr, as revealed by an experimental research and data obtained from an optical microscope. These types of wear are flank and crater wear. Because it occurs on the tool and chip interface rather than the tool work interface, crater wear is a defect caused by high temperature changes that are induced on the rake's face as an outcome of the intense interaction between chip and the cutting tool. It has been observed that crater wear does not directly affect the surface integrity of the work piece. However, flank wear happens at the interface between the tool and the work, which is observed to directly impact the machined surface's surface quality. Consequently, flank wear gradually modifies the cutting tool's geometry.

Because of the abrasive wear process, ear patterns primarily involve visible microgrooves, as seen in Figure 4.26. High pressures created at the tool-work piece interface during turning are the cause of this abrasive wear. The tool's plastic deformation caused ridges and microgrooves to emerge on the flank face. Furthermore, it is evident that the flank and crater face have narrow ridges and grooves caused by surface plastic deformation. The emergence of ridges and fine grooves on the machined surface, which signify the existence of abrasive wear, was caused by the plastic deformation of surface asperity and adherence of chip particles on the tool's flank and rake face. On the flank face of the cutting tool, chip adhesion and tooltip rattling are also visible.

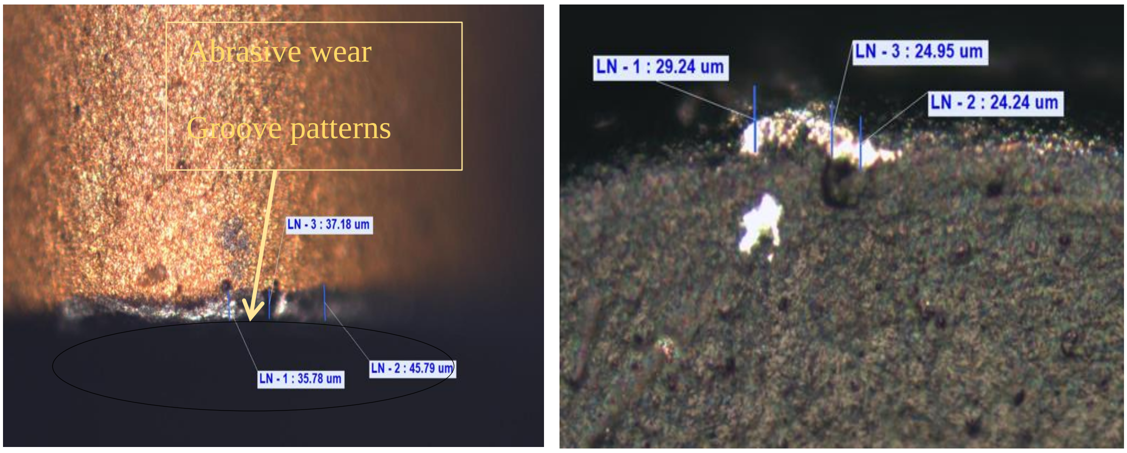

a) Cutting speed (v) = 117.984m/min, feed rate = 0.4mm/rev, depth of cut (d) = 0.573mm

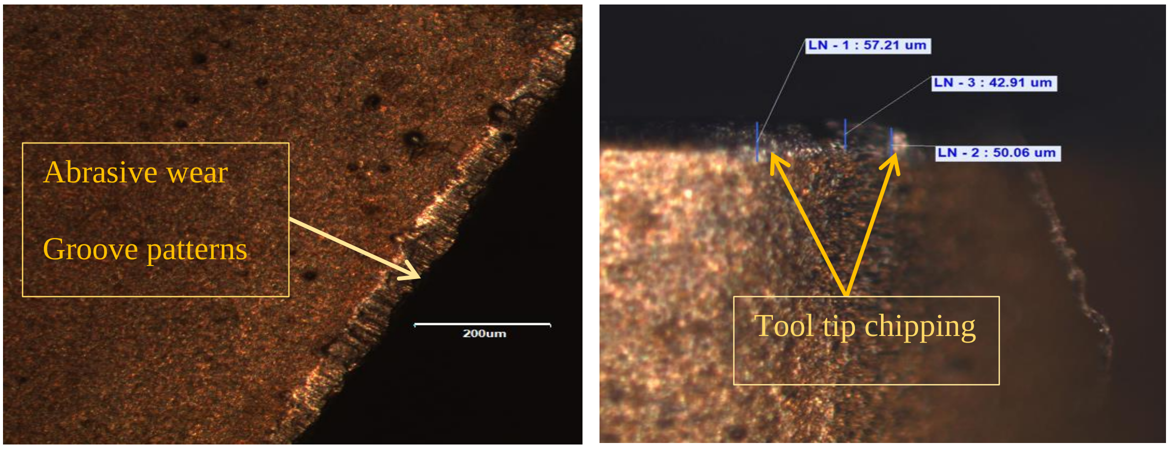

b) Cutting speed (v) = 118.231m/min, feed rate = 0.397mm/rev, depth of cut (d) = 0.373mm

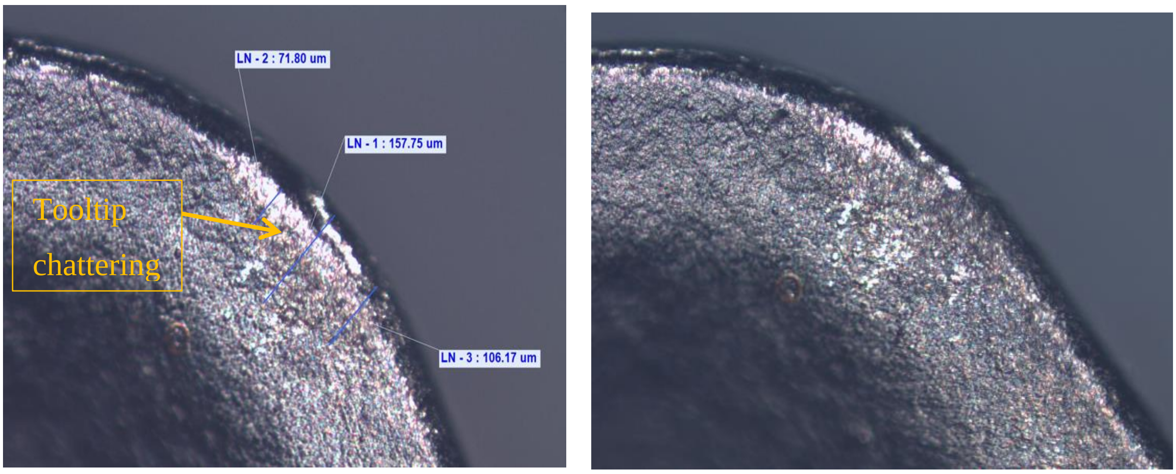

c) Cutting speed (v) = 40.029m/min, feed rate = 0.082mm/rev, depth of cut (d) = 0.223mm

Figure 4.26 Tool Tip Images with Type of Wear Observed

4.9 Confirmation experiments

In order to confirm the prediction of responses Material Removal Rate and cutting tool tip temperature, three runs were randomly selected from Multi-objective optimization using GA ideal values. The desirability function with the highest desirability is then chosen for the conformational run. Additionally, the results of the desirability function and genetic algorithm demonstrated a strong agreement with the predicted values of the replies, with an error of less than 10%, in Table 4.26.

Table 4.26 Confirmation location from GA and Desirability function

Optimum Parameters			Predicted value		Actual value		Error (%)	
Cutting speed	Feed rate	Depth of cut	MRR	Cutting tool tip temperature	MRR	Cutting tool tip temperature	MRR	Cutting tool tip temperature
117.984	0.4	0.573	17.711	75.313	16.642	76.45	6.4	1.5
118.231	0.397	0.373	15.313	84.01	14.278	85.44	7.2	1.7
40.029	0.082	0.223	0.61	42.889	0.56	44.804	4.3	4.4
40.001	0.4	0.8	15.359	69.284	14.347	70.267	7	1.4

CHAPTER- FIVE

CONCLUSION AND RECOMMENDATION

5.1 Introduction

This study used stir casting as an experimental method to generate a metal matrix composite based on magnesium and reinforced with ceramic particles such as SiC, CeO_2, and Gr. The effect of reinforcement weight percentage on the microstructure, corrosion behavior, and mechanical properties of MMCs was ascertained by creating and analyzing three samples with three distinct weight percentages of reinforcement. The material with the best properties was chosen for the secondary operation, which is machining. However, before the actual machining or experimentation was carried out, the machining properties were investigated using simulation software, DEFORM 3D, and data was collected for the optimization process using Design Expert and Mat Lab software. The optimal parameter combinations for the actual machining operation were then obtained from both optimization software, and the actual experimentation was carried out using a CNC lathe machine.

5.2 Conclusion

Based on the result and discussion the following conclusions have been drawn:

- A scanning electron microscope revealed uniform particle dispersion, and a computation yielded a maximum porosity of 0.2209 in the composite reinforced with $10CeO_2$-5SiC-4Gr.
- Adding silicon carbide, cerium oxide, and graphene to the magnesium matrix improved the mechanical properties of the metal, according to hardness and Compression tests. As a result, AZ31B-$5CeO_2$-10SiC-4Gr exhibits (111.2HV) and (339.6 MPa) compressive strength highest among all other fabricated samples.
- The corrosion and wear rate of AZ31B-$5CeO_2$-10SiC-4Gr were also 0.428 and 0.0589 respectively.
- AZ31B-$5CeO_2$-10SiC-4Gr hybrid composite was chosen for secondary processing (machining) since it have best properties than the other samples in order to use DEFORM 3D to forecast MRR, tool wear, and cutting tool tip temperature based on run findings.

- The optimum parameter combinations obtained from the design expert software were cutting speed of 40 m/min, feed rate of 0.4 mm/rev, and cut depth of 0.8 mm which results good MRR 14.347 cm^3/min and cutting tool tip temperature of 70.267 ^{0}C.
- Cutting speed is the most significant machining (turning) parameter on tool wear rate and cutting tool tip temperature, according to the ANOVA outcomes. As the cutting speed of aluminum oxide covered cemented carbide insert increased, so did the rate of tool wear and the cutting tool tip temperature.
- Rate of feed is the secondary factor that determines MRR after cut depth. The rate of feed contributed 37% to MRR, whereas the cut depth had a 27% impact.
- With an 89% influence from cutting speed, feed rate had a 7% influence on the temperature of the cutting tool tip. The difference in cutting tool temperature was mostly caused by these two parameters.
- Similar to the temperature of the cutting tool tip, wear rate was also significantly impacted by feed rate and cutting speed. The effects of feed rate were 10% and cutting speed was 85%.
- The outcomes following the rotation procedure and optimization software shown that, with an error of less than 10%, the results from simulation and experimental agree well.

5.3 Recommendation

Based on the results and conclusions found from this study, the following recommendations were made:

- For comparable investigations, other tests including impact and tensile testing may be used.
- Extrusion is an option for further improving the chosen hybrid's properties.
- Increasing the quantity of artificial samples to determine whether there is another ideal sample with superior characteristics.
- The sample's qualities being optimized in some areas.

SPECIAL ACKNOWLEDGEMENT

This research work is funded by Adama Science and Technology University under the grant number ASTU/SM-R/909/23, Adama, Ethiopia.

REFERENCES

Al-maamari, A. E. A., Iqbal, A. A., & Nuruzzaman, D. M. (2020). Mechanical and tribological characterization of self-lubricating Mg-SiC-Gr hybrid metal matrix composite (MMC) fabricated via mechanical alloying. *Journal of Science: Advanced Materials and Devices, 5*(4), 535-544.

Anand, N. (2020). Development and influence of tribomechanical properties on magnesium based hybrid metal matrix composites-a review. *Materials Research Express*, *7*(3), 036520.

Banerjee, S., Poria, S., Sutradhar, G., & Sahoo, P. (2021). Nano-indentation and corrosion characteristics of ultrasonic vibration assisted stir-cast AZ31–WC–graphite nano-composites. *International Journal of Metalcasting*, *15*, 1058-1072.

Banerjee, S., Sutradhar, G., & Sahoo, P. (2023). Effect of incorporation of graphite nanoparticles on wear characteristics of Mg-WC nano-composites in dry sliding condition. *Transactions of the IMF*, *101*(1), 29-39.

Dash, D., Samanta, S., & Rai, R. (2018). Study on fabrication of magnesium based metal matrix composites and its improvement in mechanical and tribological properties-a review. IOP Conference Series: Materials Science and Engineering,

Davis, B., Dabrow, D., Ju, L., Li, A., Xu, C., & Huang, Y. (2017). Study of chip morphology and chip formation mechanism during machining of magnesium-based metal matrix composites. *Journal of Manufacturing Science and Engineering*, *139*(9).

Dey, A., & Pandey, K. M. (2015). Magnesium Metal Matrix Composites-A Review. *Reviews on Advanced Materials Science*, *42*(1).

Gao, H., Ma, B., Singh, R. P., & Yang, H. (2020). Areal surface roughness of AZ31B magnesium alloy processed by dry face turning: An experimental framework combined with regression analysis. *Materials*, *13*(10), 2303.

Hira, J., Manna, A., Gera, P., Sharma, R., & Kumar, V. (2021). Effect of machining parameters on average surface roughness Ra while turning hybrid Mg-MMC-An experimental approach. Journal of Physics: Conference Series,

Islam, S. S. U., Khan, N. Z., & Khan, M. M. (2021). Effect of reinforcement on magnesium-based composites fabricated through stir casting: a review. *Materials Today: Proceedings*, *46*, 6513-6518.

Kandpal, B. C., Kumar, J., & Singh, H. (2018). Manufacturing and technological challenges in Stir casting of metal matrix composites–A Review. *Materials Today: Proceedings, 5*(1), 5-10.

Kavimani, V., Soorya Prakash, K., & Arun Pandian, M. (2017). Influence of r-GO addition on enhancement of corrosion and wear behavior of AZ31 MMC. *Applied Physics A*, *123*, 1-11.

Khatkar, S., Suri, N., Kant, S., & Pankaj. (2018). A review on mechanical and tribological properties of graphite reinforced self lubricating hybrid metal matrix composites. *Reviews on Advanced Materials Science*, *56*(1), 1-20.

Kumar, A., Kumar, S., & Mukhopadhyay, N. (2018). Introduction to magnesium alloy processing technology and development of low-cost stir casting process for magnesium alloy and its composites. *Journal of magnesium and Alloys*, *6*(3), 245-254.

Kumar, A., Vichare, O., Debnath, K., & Paswan, M. (2021). Fabrication methods of metal matrix composites (MMCs). *Materials Today: Proceedings*, *46*, 6840-6846.

Kumar, K. C. K., Kumar, B. R., & Rao, N. M. (2022). Microstructural, mechanical characterization, and fractography of AZ31/SiC reinforced composites by stir casting method. *Silicon*, *14*(9), 5017-5027.

Kumar, P. S., Gopal, P., & Senthilkumar, T. (2021). Machining and corrosion studies on HfC reinforced ZE41 magnesium matrix composites. *Materials Research Express, 8*(11), 116510.

Lakshmikanthan, A., Angadi, S., Malik, V., Saxena, K. K., Prakash, C., Dixit, S., & Mohammed, K. A. (2022). Mechanical and tribological properties of aluminum-based metal-matrix composites. *Materials*, *15*(17), 6111.

Liu, S., Paidar, M., Ojo, O. O., Poková, M. Š., Mehrez, S., Zain, A. M., Zhao, Q., & Wang, J. (2023). Friction stir processing of hybridized AZ31B magnesium alloy-based composites by adding CeO2 and ZrO2powders: mechanical, wear, and corrosion behaviors. *Journal of Materials Research and Technology*, *24*, 1949-1972.

Manroo, S. A., Khan, N. Z., & Ahmad, B. (2022a). Development of Nano-Composites on Rare-Earth Mg-ZE41 Alloy Via Friction Stir Processing (FSP): Microstructure, Mechanical, and Tribological Properties. *JOM*, *74*(5), 2047-2062.

Manroo, S. A., Khan, N. Z., & Ahmad, B. (2022b). Study on surface modification and fabrication of surface composites of magnesium alloys by friction stir processing: a review. *Journal of Engineering and Applied Science*, *69*(1), 1-23.

Mousavi, S. F., Sharifi, H., Tayebi, M., Hamawandi, B., & Behnamian, Y. (2022). Thermal cycles behavior and microstructure of AZ31/SiC composite prepared by stir casting. *Scientific Reports*, *12*(1), 15191.

Nagavally, R. R. (2017). Composite materials-history, types, fabrication techniques, advantages, and applications. *Int. J. Mech. Prod. Eng*, *5*(9), 82-87.

Olani, M., Kumar, D., & Asrat, G. (2023). Mechanical and corrosion properties of Fe–SiC–ZrO2 hybrid composite fabricated through powder metallurgy process. *Results in Engineering*, *17*, 100866.

Raj, K. P., Seshappa, A., & Prasad, B. A. (2020). Mechanical Characterization and Machining of MgAZ91D/SiC/Al2O3MMC by Squeeze Cast Method. IOP Conference Series: Materials Science and Engineering,

Raja, K. S., Kumar, U. M., Mathivanan, S., Ganesan, S., ArunKumar, T., Hemanandh, J., & Kumar, J. S. (2021). Mechanical and microstructural properties of graphene reinforced magnesium composite. *Materials Today: Proceedings*, *44*, 3571-3574.

Rajak, D. K., Pagar, D. D., Kumar, R., & Pruncu, C. I. (2019). Recent progress of reinforcement materials: a comprehensive overview of composite materials. *Journal of Materials Research and Technology*, *8*(6), 6354-6374.

Sajan, S., & Selvaraj, D. P. (2021). A review on polymer matrix composite materials and their applications. *Materials Today: Proceedings*, *47*, 5493-5498.

Saranu, R., Chanamala, R., & Putti, S. (2020). Review of Magnesium Metal Matrix Composites. IOP Conference Series: Materials Science and Engineering,

Sharma, A. K., Bhandari, R., Aherwar, A., & Rimašauskienė, R. (2020). Matrix materials used in composites: A comprehensive study. *Materials Today: Proceedings*, *21*, 1559-1562.

Shen, M.-J., Ying, T., Chen, F.-Y., & Hou, J.-M. (2017). Microstructural analysis and mechanical properties of the AZ31B matrix cast composites containing micron SiC particles. *International Journal of Metalcasting*, *11*, 287-293.

Shen, M., Wang, X., Li, H., Zhang, M., Ying, T., Nie, K., & Wu, K. (2018). Effects of (micron+ submicron+ nano) multisized SiC particles on microstructure and mechanical properties of magnesium matrix composites. *Journal of Composite Materials*, *52*(15), 2055-2064.

Shen, M., Wang, X., Zhang, M., Zhang, B., Zheng, M., & Wu, K. (2015). Microstructure and room temperature tensile properties of 1 μm-SiCp/AZ31B magnesium matrix composite. *Journal of Magnesium and Alloys*, *3*(2), 155-161.

Singh, N., & Belokar, R. (2021). Tribological behavior of aluminum and magnesium-based hybrid metal matrix composites: a state-of-art review. *Materials Today: Proceedings*, *44*, 460-466.

Sun, F., Fu, G., & Shen, J. (2019). Experimental investigation on micro-drilling properties of Mg-based MMCs reinforced with HAP nanoparticles. IOP Conference Series: Materials Science and Engineering,

Suneesh, E., & Sivapragash, M. (2018). Comprehensive studies on processing and characterization of hybrid magnesium composites. *Materials and Manufacturing Processes*, *33*(12), 1324-1345.

Treviso, A., Van Genechten, B., Mundo, D., & Tournour, M. (2015). Damping in composite materials: Properties and models. *Composites Part B: Engineering*, *78*, 144-152.

Veeranjaneyulu, I., Chittaranjan Das, V., & Karumuri, S. (2023). Investigation of Mechanical Properties and Microstructure of AZ31-SiC-Graphite Hybrid Nanocomposites Fabricated by Bottom Pouring-Type Stir Casting Machines. *Advances in Materials Science and Engineering*, *2023*.

Venkataiah, M., Anup Kumar, T., Venkata Rao, K., Anand Kumar, S., Siva, I., & Ratna Sunil, B. (2019). Effect of grain refinement on corrosion rate, mechanical and machining behavior of friction stir processed ZE41 Mg alloy. *Transactions of the Indian Institute of Metals*, *72*(1), 123-132.

Xiao, H., Ma, G., Ye, J., & He, Y. (2021). Preparation of graphene reinforced AZ31B magnesium-based composites by stirring casting. *Vacuum*, *191*, 110281.

Zhang, L., Luo, X., Liu, J., Leng, Y., & An, L. (2018). Dry sliding wear behavior of Mg-SiC nanocomposites with high volume fractions of reinforcement. *Materials Letters*, *228*, 112-115.

APPENDIX

Appendix 1

Hardness test results of the selected composite

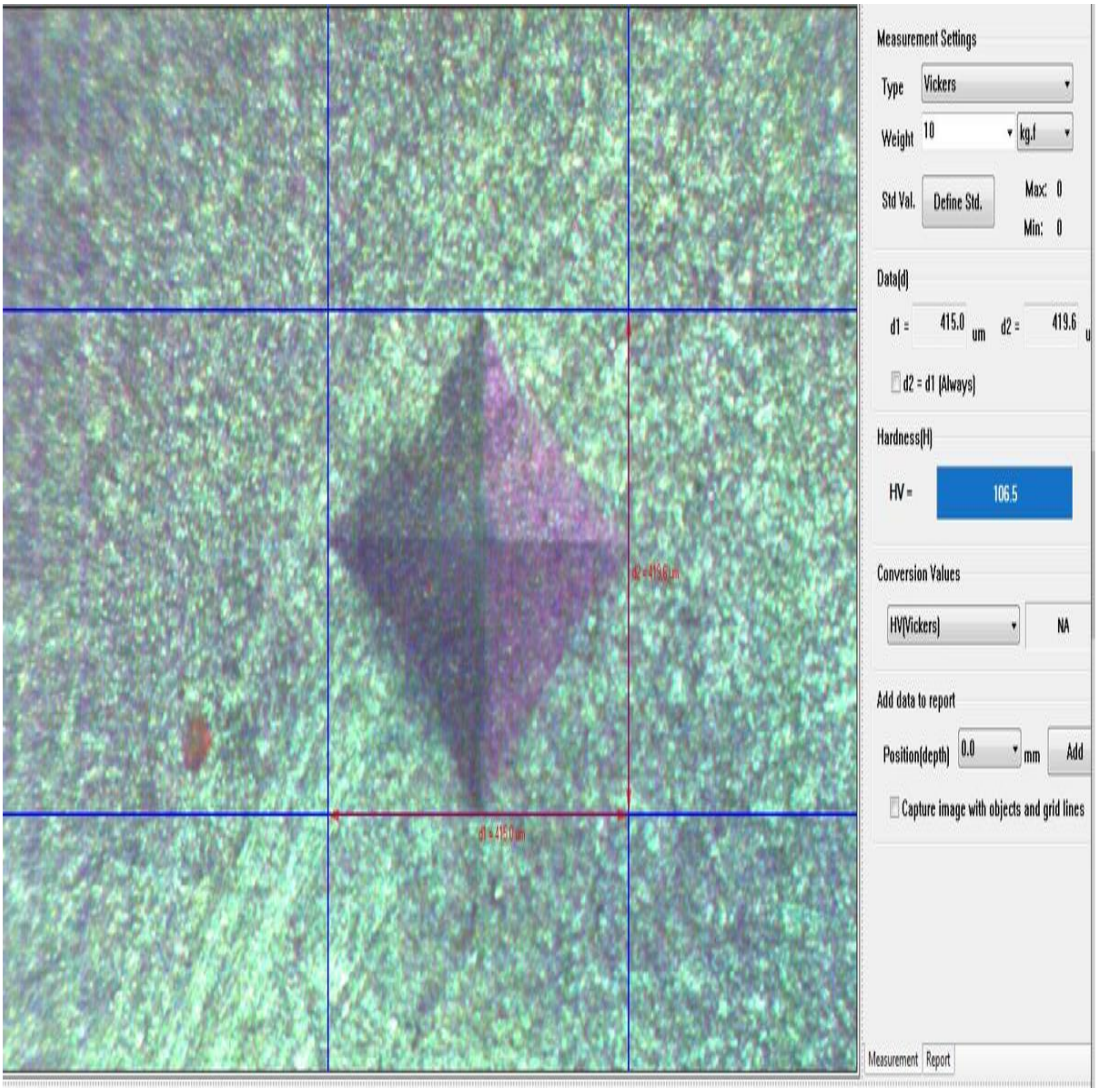

Wear rate of AZ31B-SiC-CeO$_2$-Gr samples

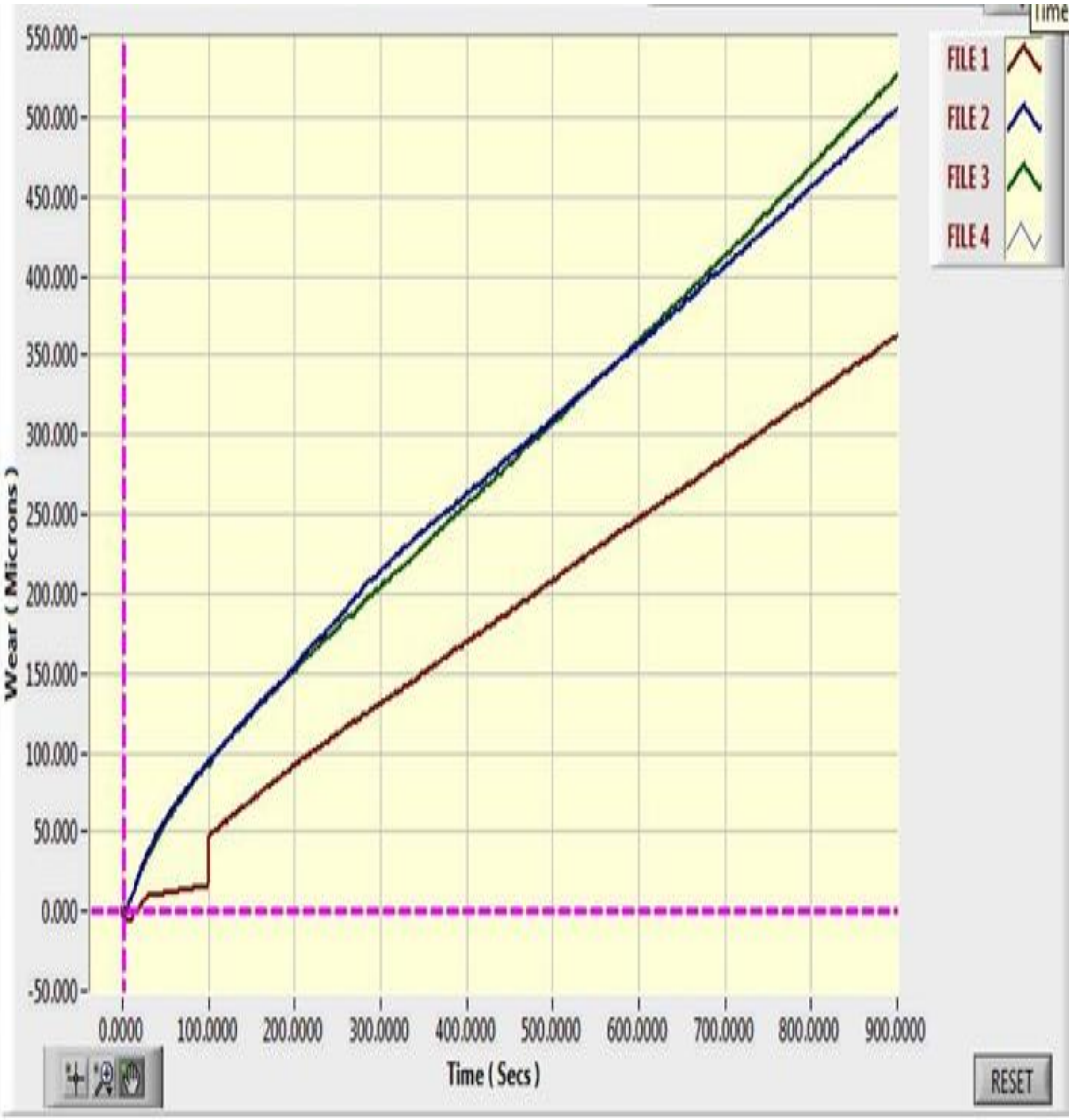

Polarization Resistance and Corrosion Rate Calculation from Tafel Plot

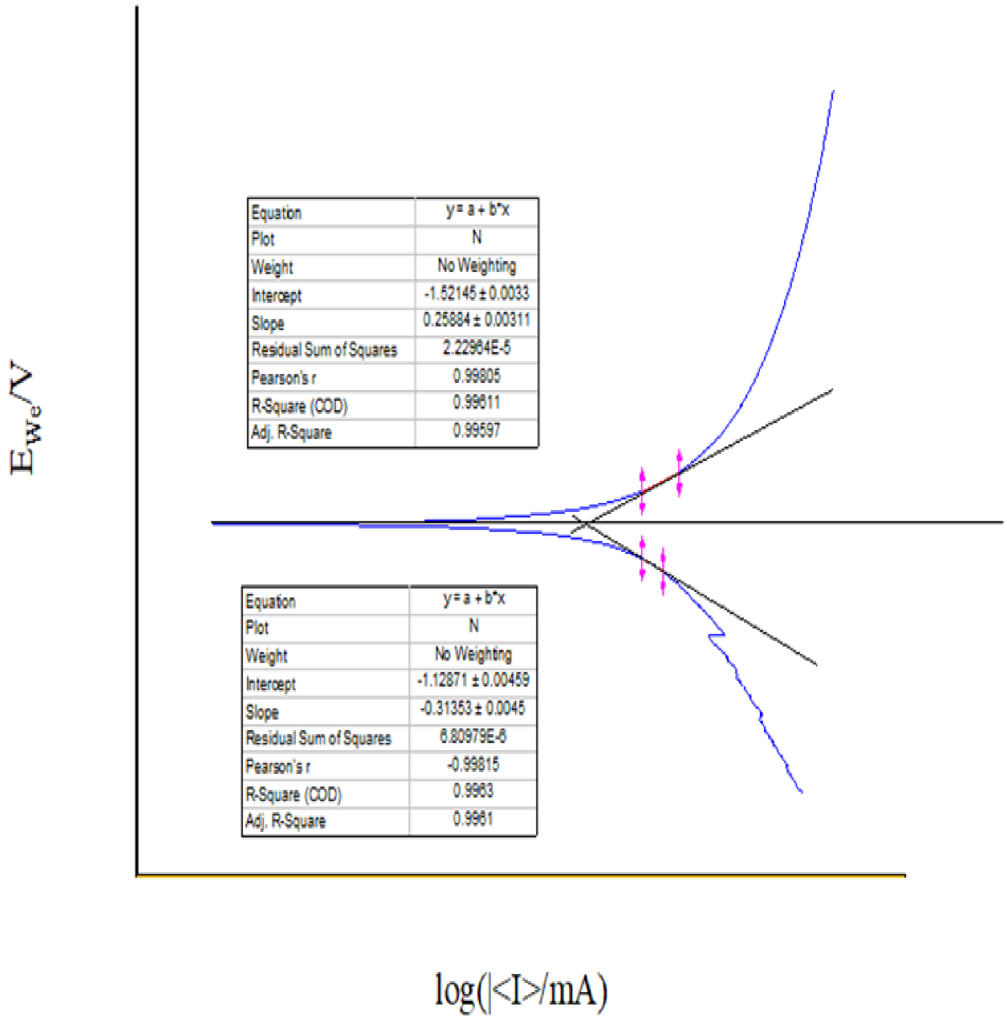

Appendix 2

Simulation results of volume before and after turning operation using DEFORM 3D software